

Growth and Remodeling of Human Abdominal Aorta Aneurysms

A dissertation submitted by
Wenjian Lin

In partial fulfillment of the requirements
for the degree of
Doctor of Philosophy
in
Civil and Environmental Engineering
Tufts University

May 2018

Advisor: Prof. Luis Dorfmann

Abstract

The human abdominal aorta aneurysm (AAA) has been increasingly modeled as a continuous deformation process in recent years. Changes in both structure and material of artery wall have been studied and analyzed. This thesis aims to address key issues related to the nonlinear modeling of AAA development, and a continuous growth and remodeling (G&R) model was proposed. The model incorporates artery wall material growth and degradation, microstructure remodeling and artery vessel stability to simulate and predict the aneurysm development. The kinematic model is described in which simultaneously occurring growth and deformation are considered as a sequence of two mappings, one representing stress-free growth and the other representing the deformations of the tissue due to stresses acting on the tissue. In the simulation, we combine the growth theory and remodeling theory, and apply it to the simulation of patient aneurysm development. Both microstructure geometry and component mass changes are accounted for. The fundamental concepts of the nonlinear theory of elasticity are addressed and suitable continuous material models are formulated. The model depicts the changes of the outer radius of a dilating abdominal aorta as a function of axial position over a twelve-year period with an applied pressure of 16 kPa (120 mmHg). Numerical results show that over this period, the maximum dilation increased from 12.94 mm to about 35 mm, and the elastin dropped from 60% to less than 20%. From years 8 to 12, as the bulge expanded, the

maximum von Mises stress increased almost four times, from 235 to 925 kPa.

Mixture theory of growth and remodeling predicted the development of inhomogeneous mechanical properties and dilatation of the diseased section of the arterial wall. The rate of expansion depended primarily on the rate of production and removal of elastin and collagen as well as on the change in fiber microstructure.

Acknowledgements

First and foremost, I'd like to express my gratitude to my advisor, Prof. Dorfmann. Thank you for your insight, guidance and extreme patience, I could not make this journey without your help. I would like to also thank Dr. Peattie for providing me the support, knowledge and enthusiasm on the AAA project. Thank you to my entire committee, Professors Helen Suh, Robert Viesca, James Adler and Robert Peattie for giving your valuable time and unique prospective you each bring.

To my office mates, past (Chris, Tony) and present (Nate, Jordan), thank you for providing me support on my research and life. I would like to thank Dr. Francesco Pancheri, it's been a pleasure working with you.

None of this would have been possible without my dearest family. You have given me all your support and patience throughout my life, thank you for supporting me when I quit my job and come to a place that is half a world from you, thank you for understanding the journey to a PhD is not short or easy. I know you have been through many difficult times, and now it's my turn to fulfill my duty and support the family.

In loving memory of grandpa

Contents

1	Introduction	3
1.1	Aneurysm rupture factors	5
1.1.1	Diameter	5
1.1.2	Expansion rates	6
1.1.3	Blood pressure	6
1.1.4	Biomechanical factors	6
1.1.5	Other factors	7
1.2	Basic background of soft tissue simulation	7
2	Nonlinear theory of elasticity	12
2.1	Hyperelastic material strain energy function	15
2.2	Isotropic materials loading responses	16
2.2.1	Responses under uniaxial loading	16
2.2.2	Responses under biaxial loading	17
3	Aneurysm material models review	19
3.1	Constitutive models	20
3.1.1	Fung-Type model	20
3.1.2	Humphrey and Yin model	21
3.1.3	Holzappel model	21
3.1.4	Baek and Humphrey model	22
3.1.5	Watton and Hill model	23
3.1.6	Volokh model	24

3.1.7	Other models	25
3.2	Finite element simulation	25
3.3	Mixture theory	28
3.4	Remodeling theory	30
4	Growth and remodeling with application to AAA	33
4.1	Hyperelasticity	33
4.2	Fiber deposition and remodeling	35
4.3	Mass balance	37
4.4	Energy function	38
4.5	Application to aneurysm development	39
4.5.1	Constitutive model	40
4.5.2	Isotropic matrix	40
4.5.3	Collagen fibers	42
4.5.4	Volumetric contribution	45
4.6	Computational model and results	45
4.6.1	Model parameters	45
4.6.2	Material parameters	46
4.6.3	Results	47
5	Concluding remarks	55
A	Appendix A	60
A.i	ABAQUS input file code	60
A.ii	UMAT code	64
A.iii	PYTHON code	73

B Appendix B	
Growth and remodeling with application to abdominal aortic aneurysms	77
C Appendix C	
Histology and biaxial mechanical behavior of abdominal aortic aneurysm tissue samples	103
References	116

List of Tables

1	AAA diameter and rupture correlation.	5
2	Material parameters of elastin	47
3	Material parameters of collagen fibers	47

List of Figures

1	Type of arterial aneurysms	4
2	Structure of an elastic artery	8
3	Equibiaxial test performed on human artery sample	10
4	Configuration and motion of a continuum body.	12
5	A typical finite element mesh model of AAA	26
6	Finite element simulation of artery wall stress	27
7	The changes of radius	49
8	The changes of mass fractions	50
9	The stretches of matrix material on a fiber direction	50
10	The stretches of healthy and remodeled collagen fibers	51
11	Changes of the recruitment variables over a twelve-year period	52
12	The von Mises stress distribution	53
13	The changes of the Cauchy stress component of healthy and diseased tissues over a twelve-year period	54
14	The changes of the axial component of the Cauchy stress of healthy and diseased tissues	54

List of Symbols

θ	angle
τ	shear stress
σ	Cauchy stress tensor
λ	stretch ratio
\mathbf{F}	deformation gradient tensor
W	strain energy function
\mathbf{I}	identity tensor
ϵ	strain tensor
\mathbf{B}	Left Cauchy-Green deformation tensor
p	pressure
\mathbf{C}	Right Cauchy-Green deformation tensor
T, t	time
U	strain energy
δ_{ij}	Kroenecker delta
ρ	density
∇	gradient operator
\mathcal{B}	configuration
\mathbf{X}, \mathbf{x}	position vector
\mathbf{R}	proper orthogonal tensor
J	Jacobian determinant
V	volume
I_i	principal invariants

M	orientation vector
χ	vector function
P	nominal stress tensor
G	deposition tensor
r	remodeling factor
m	mass density production rate
Q	survival function
E	unit base vector
N	unit normal vector

Growth and Remodeling of Human Abdominal Aorta Aneurysm

Doctoral Examining Committee:

Prof. Luis Dorfmann (committee chair)

Department of Civil and Environmental Engineering, Tufts University

Prof. Helen Suh

Department of Civil and Environmental Engineering, Tufts University

Prof. Robert Viesca

Department of Civil and Environmental Engineering, Tufts University

Prof. James Adler

Department of Mathematics, Tufts University

Dr. Robert Peattie

Department of Surgery, Tufts Medical Center

Statement

An arterial aneurysm is defined as a local dilation of a blood vessel with respect to the original artery. The risk of abdominal aortic aneurysm (AAAs) increases dramatically in the presence of the following factors: age older than 60 years, smoking, hypertension and Caucasian ethnicity.

Patient with AAAs can be treated with medical therapy, antibiotic therapy, risk factor reduction, surgical repair or endovascular repair depends on the size of the aneurysm and the symptoms. The mortality of AAA rupture is as high as 90% before the patients reach the operating room, which suggests the prediction of AAA development or rupture very important.

There are enormous researches done to study the biomechanical behavior of aneurysm tissues, however, most of which focused on the diseased tissue, which left the most critical factor, the development of AAA unaddressed. This inspires us to focus on the changes of tissue components and structures, and to predict the biomechanical behavior over a long period of time.

Chapter 1

1 Introduction

An arterial aneurysm is a local dilation of a blood vessel with respect to the original artery (Figure 1). When an aortic diameter is at least one and one-half times the normal diameter at the level of the renal arteries, the abdominal aortic aneurysm (AAA) is formed. Generally, a segment of abdominal aorta with a diameter of greater than 3.0 cm is considered an aortic aneurysm [91]. Approximately 80% of aortic aneurysms occur between the renal arteries and the aortic bifurcation. Each year in the United States, AAA rupture causes more than 15,000 deaths, with an additional 1400 deaths resulting from the 45,000 repair procedures performed to prevent rupture [114], and the incidence of AAA has been steadily increasing with up to 8% of men over the age of 60 affected [115].

The cause of AAA is still not clear, but there are several factors such as smoking, hypertension, hypercholesterolemia and male sex are generally known as significant risk factors [10]. Management options for patients with aneurysm include:

1. Medical therapy which may be helpful in patient with small to medium sized aneurysm;
2. Antibiotic therapy which is based on evidence of chronic inflammation;
3. Risk factor reduction which includes blood pressure and lipids control;
4. Surgical repair which usually requires open-abdomen operation;

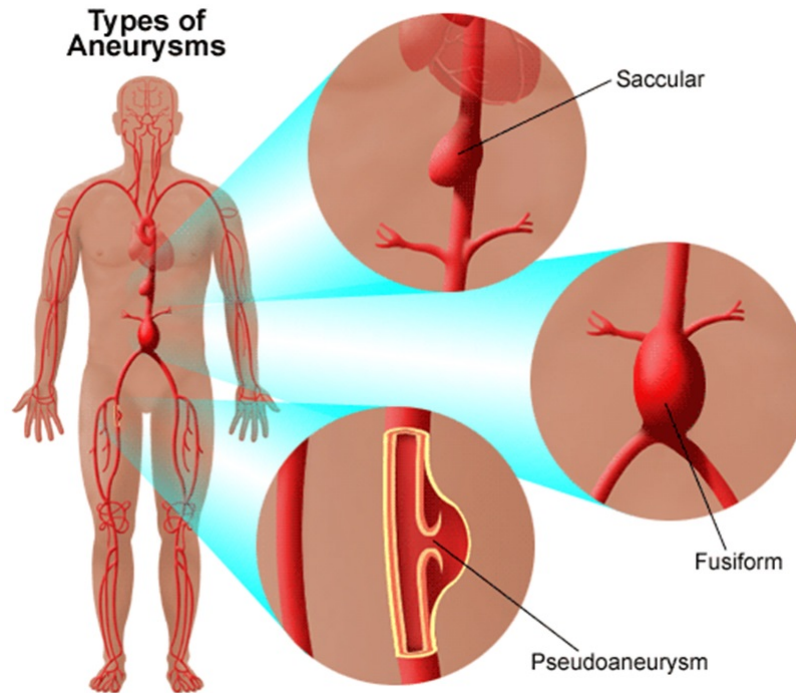


Figure 1: Type of arterial aneurysms[119].

5. Endovascular repair which inserts an endograft into the lumen that excludes the aneurysm from blood flow.

However, any medication strategy for the treatment of AAA must address rupture as well as expansion of artery wall. The AAA rupture is a biological process that involves biomechanical, cellular and proteolytic influences and biomechanical factors. The irreversible damage to the structure of artery wall results in dilatation or even rupture when stress in wall exceeds the strength limit. Meanwhile, different approaches regarding patient variables are adopted when predicting AAA expansion or rupture.

1.1 Aneurysm rupture factors

1.1.1 Diameter

The diameter of aneurysm is a factor of AAA rupture. Many studies were performed to find correlation between AAA rupture rate and diameter. Brewster et al. [13] published the data addressing the relation, shown in Table 1. The tests were based on autopsy and didn't represent the in vivo conditions. Some other problems include low rates of autopsy following patient decease and errors in AAA diameter measurement. More importantly, the rupture risk of larger diameter is more difficult to get because most large AAA were surgically repaired.

Table 1: AAA diameter and rupture correlation.

Aneurysm diameter(cm)	Risk of rupture
≤ 4.0	0.2-0.4%
4.0-4.9	0.5-5%
5.0-5.5	3-15%
6.0-6.9	10-20%
7.0-7.9	20-40%
≥ 8.0	30-50%

Research data by Brewster et al. [13]. Aneurysm with larger diameter has higher risk of rupture.

1.1.2 Expansion rates

Studies show the rapid AAA expansion rate is associated with increasing rupture risk [19, 74]. The findings show larger AAA expansion rates will more likely induce the AAA ruptures. It's found that larger AAA will usually be accompanied by larger expansion rates (5.3 mm/year for AAA with diameter less than 4 cm versus 7.4 mm/year for AAA with 5 cm diameter or more [74]).

1.1.3 Blood pressure

Foster et al. [36] reviewed 75 patients with AAA and observed that 72% of patients died had diastolic hypertension. Peattie et al. [94] studied pulsatile flow in fusiform models of AAAs, and they concluded that larger aneurysms in vivo may be subject to more frequent and intense turbulence than smaller aneurysms.

1.1.4 Biomechanical factors

The biomechanical method used in predicting AAA rupture is based on stress in artery wall. The basic principle of AAA expansion is increasing stress or decreasing artery wall stiffness. Many material models and simulation methods were proposed. We will do a detailed review and later adopt some of the theories and suggest a continuous material model that can simulate AAA development.

1.1.5 Other factors

Other factors associated with AAAs are male gender, cigarette smoking, atherosclerosis and genetics. Reasons for gender related differences remain unclear, but older (over 65) men are about six times more likely than older women to have an AAA [48]. Enevoldsen et al.[29] found smoking increases the risk up to seven times.

1.2 Basic background of soft tissue simulation

The continuum biomechanics consists of three general areas of study: identification of fundamental concepts; formulation of constitutive relations; and solution of boundary value problems [87]. It follows the basic postulates of mechanics such as law of mass conservation, energy balance and momentum balance, other basic concepts such as stress, strain and elasticity is valid as well. As a result, more and more studies are focusing on formulating a reliable constitutive relation to solve the boundary value problems. Fung [39] pointed out that the greatest needs in living tissue simulation are collecting data in different loading conditions and generalizing a theory that can best describe the stress and strain relation. However, the process is not easy, as the properties of biological material vary from individual to individual, part to part and change with time and environment. Additionally, even for a given sample, as the components are usually not uniform, the mechanical behaviors are usually different in each direction.

The human infrarenal aorta is about 12 *cm* long, 2 *cm* in diameter and 2 *mm* thick. By dry weight, the artery wall consists of about 40% collagen

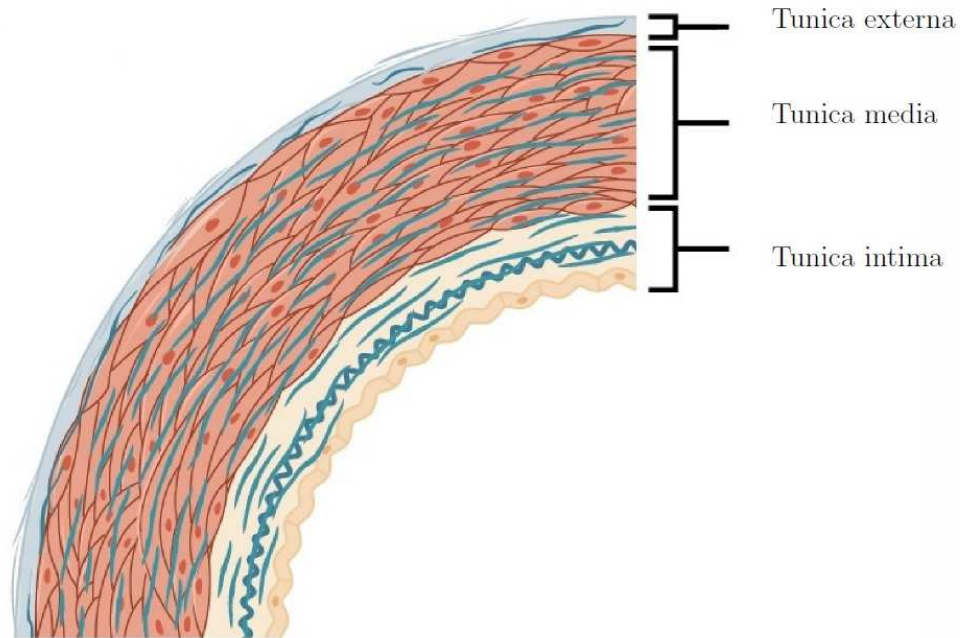


Figure 2: Structure of an elastic artery. Constructed by OpenStax.

fibers, 40% elastin and ground substance and 20% vascular smooth muscle cells [52]. The healthy abdominal aorta is a transitional elastic artery and as pointed out by Fung et al.[41], it's composed of three layers (intima, media and adventitia) (Figure2). The intima consists of a layer of endothelium and connective tissues on the intact internal elastic lamina (IEL). The media has about 30 concentric elastic lamellae which are composed of elastic lamina (contributes to 2/3 the thickness of the total elastic lamina), smooth muscle and extracellular matrix contents. The adventitia is the outermost layer and mainly composed of collagen fibers [64, 65, 144].

Contrary to the healthy artery, the AAA tissues changed greatly in each tunica. The AAA intima appears to have thickened smooth muscle as the intima undergoes cellular alteration. The causes are not well agreed. Sary

et al.[120] thought it's due to expansion of resident intimal cells, while others [111, 141] believed this is due to cell migration from media into intima. The thickening intima typically forms two distinct laminated layers, a superficial subendothelial layer and a musculoelastic layer. The mid layer media undergoes penetration from both intima and adventitia. The lipid core erodes the underlying media and the adventitial vasa vasorum network penetrates the media as well [85]. Additionally, the elastic tissue degradation stimulates the production of peptides, which accelerates the angiogenesis [86, 106], and this process disrupts the media structure with large vascularised region of media consisting of reduced elastic tissue and smooth muscle cells. The intima atherosclerosis and media neovascularization result in great medial smooth muscle loss due to cell death because of apoptosis [11, 53, 77], and the AAAs has approximately 50% less smooth muscle cells compared to that of healthy artery. Adventitia is observed thickening progressively due to the proliferation and expansion of the vasa vasorum network. Chronic intraluminal thrombus (ILT) is often observed incorporated into the AAA intima. The ILT consists of layer of fresh red clot, thrombus and fibrinolysed abluminal layer. ILT thickens the artery wall and limits the oxygen transport which resulting in hypoxia-associated degeneration [84, 136]. Moreover, ILT blocks the leukocytes and platelets, resulting in increase of matrix metalloproteinases (MMP), which has strong impact on AAA pathogenesis [56, 105, 138]. Recent studies show the presence of ILT also impacts the blood flow and increases local wall stress [96].

In most lab tests and simulations, due to the difficulties in distinguishing the behaviors of each layer, the artery wall is usually treated as one

layer structure. As early as 1880, Roy [109] has observed the arteries behave anisotropically. Figure 3 shows one of the test stress and strain curves by Dr. Francesco Pancheri in our laboratory performed on human artery tissue sample. It's clearly shown that although the same stretch is applied simultaneously on both directions, the corresponding stresses are not the same.

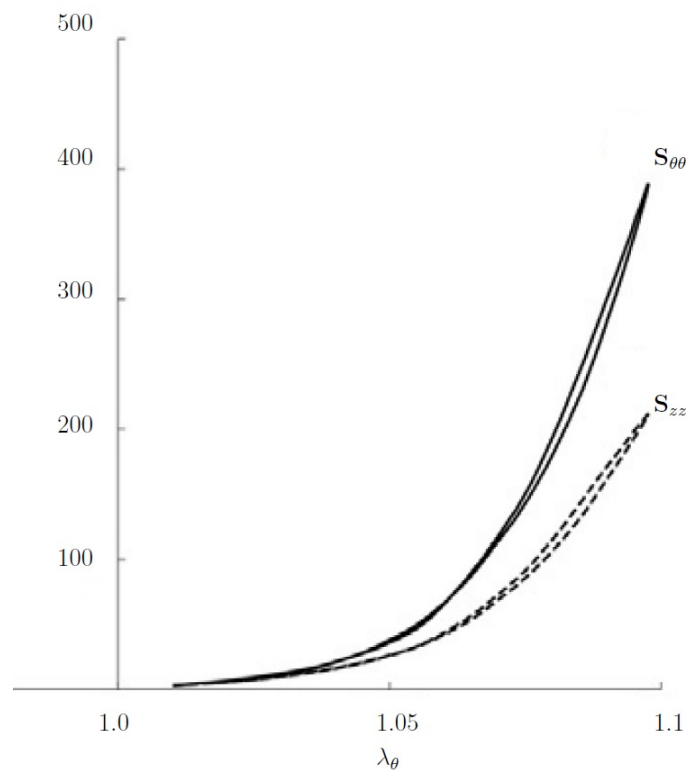


Figure 3: Equibiaxial test performed on human artery sample. Longitudinal and circumferential directions are stretched up to 1.1.

In summary, the soft tissues exhibit complicated behaviors and different individual tissues usually require different models. In our research, we focus the study on human abdominal aortic aneurysm material models. Consti-

tutive relation describes the response of a material subjected to loads or deformation, which depends on the constitution of the material. Due to the complexity of artery tissue which includes multiple components and various microstructures, many studies were primarily based on the behaviors of interest, as a result of which, many material models and theories were proposed in different aspects, and they are capable of describing relations under specific conditions but not in general. In our following introductions, we will review the most adopted and most recent material models and theories, but since the continuous mechanics theory will be used, it's best to briefly explain the nonlinear theory of elasticity.

Chapter 2

2 Nonlinear theory of elasticity

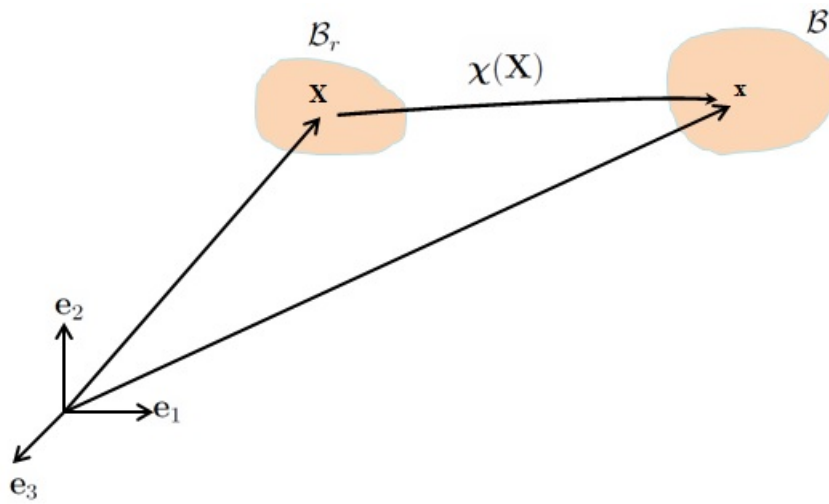


Figure 4: Configuration and motion of a continuum body.

Figure 4 shows the motion of a continuum body in the three-dimensional Euclidean space. The stress-free configuration is denoted as \mathcal{B}_r , and an arbitrary material point is chosen and described by its position vector \mathbf{X} . A mechanical deformation applied to the body, and the material point \mathbf{X} occupies the new position \mathbf{x} under motion vector χ in current deformed configuration denoted as \mathcal{B} . χ is a vector field that specifies the place \mathbf{x} of \mathbf{X} , and is called the motion of the body \mathcal{B} . In other words, the motion vector χ is a one-to-one mapping from reference configuration to current configuration.

The deformation gradient tensor \mathbf{F} relative to reference configuration \mathcal{B}_r

is defined by

$$\mathbf{F} = \text{Grad} \mathbf{x} \quad (2.1)$$

where Grad is gradient operator with respect to \mathbf{X} . The Cartesian components of \mathbf{F} are $F_{i\alpha} = \partial x_i / \partial X_\alpha$, where x_i and X_α are components of \mathbf{x} and \mathbf{X} respectively.

At each point \mathbf{X} , the deformation gradient \mathbf{F} has the following unique polar decomposition

$$\mathbf{F} = \mathbf{R}\mathbf{U} \quad \text{or} \quad F_{i\alpha} = R_{i\beta} U_{\beta\alpha} \quad (2.2)$$

where $\mathbf{R}^T \mathbf{R} = \mathbf{I}$, $\mathbf{U} = \mathbf{U}^T$, $()^T$ is transpose operator. \mathbf{R} is a proper orthogonal tensor with $\det \mathbf{R} = 1$, called the rotational tensor. \mathbf{U} is the unique, positive definite, symmetric right stretch tensor and it measures local stretching or contraction along their mutually orthogonal eigenvectors, which is a change of local shape. For example, the spectral form of stretch can be expressed as

$$\mathbf{U} = \sum_{i=1,2,3} \lambda_i \mathbf{u}^i \otimes \mathbf{u}^i \quad (2.3)$$

where λ_i and \mathbf{u}^i are principal stretches and principal directions of \mathbf{U} , and symbol \otimes indicates tensor product.

To consider the change in volume, we adopt the volume ratio definition $J = \det \mathbf{F} > 0$, which also expresses the relation between volume in reference configuration and current configuration

$$dv = JdV \quad (2.4)$$

where dv and dV denote the volume element in current and reference configurations respectively. It's apparent that for incompressible material (volume keeps constant), $J = \det \mathbf{F} = 1$.

From equation (2.2) and equation (2.3), we have

$$J = \det \mathbf{F} = \det \mathbf{U} = \lambda_1 \lambda_2 \lambda_3 \quad (2.5)$$

We introduce the right Cauchy-Green tensor \mathbf{C}

$$\mathbf{C} = \mathbf{F}^T \mathbf{F} \quad (2.6)$$

\mathbf{C} is an important strain measure in material coordinates. Note that \mathbf{C} is symmetric and positive definite at each \mathbf{X} , thus,

$$\mathbf{C} = \mathbf{F}^T \mathbf{F} = (\mathbf{F}^T \mathbf{F})^T = \mathbf{C}^T \quad (2.7)$$

Similarly, the left Cauchy-Green tensor \mathbf{B} can be defined as

$$\mathbf{B} = \mathbf{F} \mathbf{F}^T \quad (2.8)$$

Accordingly, the three principal invariants for \mathbf{C} can be defined by

$$\begin{aligned} I_1 &= \text{tr} \mathbf{C} \\ I_2 &= \frac{1}{2} [(\text{tr} \mathbf{C})^2 - \text{tr}(\mathbf{C}^2)] \\ I_3 &= \det \mathbf{C} = J^2 \end{aligned} \quad (2.9)$$

where tr is the trace of the tensor, recall equation (2.5), the invariants above can be rewritten in terms of principal stretches expressed as

$$\begin{aligned} I_1 &= \lambda_1^2 + \lambda_2^2 + \lambda_3^2 \\ I_2 &= \lambda_1^2 \lambda_2^2 + \lambda_2^2 \lambda_3^2 + \lambda_1^2 \lambda_3^2 \\ I_3 &= \lambda_1^2 \lambda_2^2 \lambda_3^2 \end{aligned} \quad (2.10)$$

In our following studies of human tissue, the material behaves anisotropically because of the embedded fibers, as a result, additional invariants are introduced to express this deformation,

$$I_4 = \mathbf{A} \cdot \mathbf{CA} \quad (2.11)$$

$$I_6 = \mathbf{A}' \cdot \mathbf{CA}'$$

where \mathbf{A} and \mathbf{A}' specify the two set of fiber orientations in reference configuration.

For an incompressible anisotropic material, which $I_3 = 1$, the derivations of equation (2.9) and equation (2.11) are given by

$$\begin{aligned} \frac{\partial I_1}{\partial \mathbf{F}} &= 2\mathbf{F}^T & \frac{\partial I_2}{\partial \mathbf{F}} &= 2(I_1\mathbf{F}^T - \mathbf{F}^T\mathbf{F}\mathbf{F}^T) \\ \frac{\partial I_4}{\partial \mathbf{F}} &= 2\mathbf{A} \otimes \mathbf{FA} & \frac{\partial I_6}{\partial \mathbf{F}} &= 2\mathbf{A}' \otimes \mathbf{FA}' \end{aligned} \quad (2.12)$$

2.1 Hyperelastic material strain energy function

We briefly introduce the finite hyperelastic theory which was introduced by Green and Adkins [47]. The strain energy W is defined per unit volume in the reference configuration. For the case in which W is solely a function of \mathbf{F} , which $W = W(\mathbf{F})$. We now restrict the attention to homogeneous materials only in which the distribution of the internal constituents are assumed to be uniform on the continuum scale. The strain energy $W(\mathbf{F})$ quantifies the amount of energy associated for the deformation from reference configuration to the current loaded configuration. The Cauchy stress can be written as

$$\boldsymbol{\sigma} = \mathbf{F} \frac{\partial W(\mathbf{F})}{\partial \mathbf{F}} - p\mathbf{I} \quad (2.13)$$

where p is hydrostatic pressure.

For an incompressible anisotropic material, the form of strain energy W can be rewritten in terms of independent invariants I_1, I_2, I_4, I_6 . We rewrite $W = W(I_1, I_2, I_4, I_6)$. To get the explicit form of Cauchy stress in terms of invariants, we apply the chain rule on equation (2.12), the Cauchy stress takes the following form:

$$\sigma = 2(W_1 + I_1 W_2)\mathbf{B} - 2W_2\mathbf{B}^2 + 2W_4\mathbf{a} \otimes \mathbf{a} + 2W_6\mathbf{a}' \otimes \mathbf{a}' - p\mathbf{I} \quad (2.14)$$

where $W_i = \partial W / \partial I_i$, and \mathbf{B} is predefined left Cauchy-Green tensor. \mathbf{a} and \mathbf{a}' are the push forward form of \mathbf{A} and \mathbf{A}' respectively with $\mathbf{a} = \mathbf{F}\mathbf{A}$ and $\mathbf{a}' = \mathbf{F}\mathbf{A}'$. When fiber terms I_4, I_6 are not presented, the above expression yields a standard isotropic material.

2.2 Isotropic materials loading responses

The purpose of introducing the strain energy function is to mathematically describe the material mechanical responses under loading conditions. To be able to achieve that, we need to express the stress and stretch in each direction explicitly. In the following discussion, we will show the material responses under uniaxial loading and biaxial loading conditions.

2.2.1 Responses under uniaxial loading

Under uniaxial loading conditions, loads are applied on one direction only, all other directions are free to move, thus

$$\sigma_1 = \sigma, \quad \sigma_2 = \sigma_3 = 0 \quad (2.15)$$

and for incompressible homogeneous material,

$$\lambda_1 = \lambda, \quad \lambda_2 = \lambda_3 = \lambda^{-1/2} \quad (2.16)$$

The principal invariants in equation (2.10) take the form

$$\begin{aligned} I_1 &= \lambda^2 + 2\lambda^{-1} \\ I_2 &= 2\lambda + \lambda^{-2} \end{aligned} \quad (2.17)$$

recall equation (2.14), the non-zero stress component is

$$\sigma = 2W_1(\lambda^2 - \lambda^{-1}) + 2W_2(\lambda - \lambda^{-2}) \quad (2.18)$$

where W_1 and W_2 are defined in the previous chapter and they are related to strain energy specified.

From equation (2.16), it's apparent that the deformation is related to λ only, thus, we can introduce an alternative strain energy function $\bar{W}(\lambda)$ which depends on λ only. Using the chain rule and replacing W_i in equation (2.18), the non-zero stress component can be rewritten as

$$\sigma = \lambda \bar{W}_\lambda \quad (2.19)$$

where \bar{W}_λ is the derivative of \bar{W} with respect to λ which $\bar{W}_\lambda = \partial \bar{W} / \partial \lambda$.

2.2.2 Responses under biaxial loading

Materials under biaxial loading conditions, loads are applied on two principal directions, the third direction is free to move, which $\sigma_3 = 0$. For incompressible material,

$$\lambda_3 = \lambda_1^{-1} \lambda_2^{-1} \quad (2.20)$$

recall equation (2.10), the two principal invariants are

$$\begin{aligned} I_1 &= \lambda_1^2 + \lambda_2^2 + \lambda_1^{-2}\lambda_2^{-2} \\ I_2 &= \lambda_1^{-2} + \lambda_2^{-2} + \lambda_1^2\lambda_2^2 \end{aligned} \quad (2.21)$$

Substituting the above expressions into equation (2.14), we have

$$\begin{aligned} \sigma_1 &= 2(\lambda_1^2 - \lambda_1^{-2}\lambda_2^{-2})W_1 + 2(\lambda_1^2\lambda_2^2 - \lambda_1^{-2})W_2 \\ \sigma_2 &= 2(\lambda_2^2 - \lambda_1^{-2}\lambda_2^{-2})W_1 + 2(\lambda_1^2\lambda_2^2 - \lambda_2^{-2})W_2 \end{aligned} \quad (2.22)$$

similarly to uniaxial loading conditions, the strain energy function W depends on λ_1, λ_2 only, thus, the strain energy function can be rewritten as $\bar{W}(\lambda_1, \lambda_2)$, substituting into equation (2.22), the above expressions yield a simple form:

$$\begin{aligned} \sigma_1 &= \lambda_1 \bar{W}_1 \\ \sigma_2 &= \lambda_2 \bar{W}_2 \end{aligned} \quad (2.23)$$

where $\bar{W}_i = \partial \bar{W} / \partial \lambda_i$.

Chapter 3

3 Aneurysm material models review

Due to the complexity of aneurysm, many research groups have devoted their attention to the study of artery wall materials with different efforts. Among these attempts, when classified by the length of simulation, they can be divided into two major aspects. One focuses on instantaneous stress strain relations such as loading under uniaxial or biaxial test protocols and the other focuses on long term stress strain relation by taking time factor into consideration, such as considering mass or material components change as a result of artery wall evolution. It appears that loss of elastin initiates the dilatation, turnover of collagen promotes enlargement, and local high stress leads to rupture. In particular, AAAs may have 90% less elastin than normal aorta [14]. The significantly weakened media appears to be compensated structurally by a thickened, fibrotic adventitia. Although the amount of intramural collagen in an AAA may not differ significantly from that in the non-aneurysmal aorta, there may be different degrees of undulation, re-alignment toward the circumferential direction, increased cross-linking, and varying distributions along the length of the lesion [14, 82]. With the help of modern technology, a lot of new techniques are adopted in AAA simulation, among which, FEM simulation is more commonly used now.

3.1 Constitutive models

Since pointed out by Fung [39], many constitutive models were proposed based on the specific tests on material samples [26, 39, 54, 57, 80]. Many models were built in improvement of the previous models by adding more variables to account for more mechanical behaviors, thus, we will selectively show the most adopted models and some newly proposed models.

3.1.1 Fung-Type model

To simulate the complicated behavior of biological materials, Fung et al. [40] proposed a material model that is suitable to simulate arbitrary 3D state of deformations. The general form is

$$W = \frac{1}{2}c[e^Q - 1] \quad (3.1)$$

where $c > 0$ is a stress-like material parameter and Q is given by

$$Q = b_1 E_{\Theta\Theta}^2 + b_2 E_{ZZ}^2 + b_3 E_{RR}^2 + 2b_4 E_{\Theta\Theta} E_{ZZ} + 2b_5 E_{ZZ} E_{RR} + 2b_6 E_{RR} E_{\Theta\Theta} + b_7 E_{\Theta Z}^2 + b_8 E_{RZ}^2 + b_9 E_{\Theta R}^2 \quad (3.2)$$

b_i ($i = 1, 2, \dots, 9$) are dimensionless material parameters and E_{AB} for $(A, B = R, \Theta, Z)$ are the components of the Green-Lagrange strain tensor $\mathbf{E} = (\mathbf{C} - \mathbf{I})/2$ referred to the cylindrical polar coordinates (R, Θ, Z) in the reference configuration.

As a very basic 3-D material model, the Fung-type model has been applied in many special cases and most extensively in 2-D structures where the non-zero terms in equation (3.2) are b_1, b_2, b_4 , which corresponds to the membrane structures.

3.1.2 Humphrey and Yin model

Humphrey and Yin [62] noticed the anisotropic behavior of soft tissues and they proposed a material model that considers both isotropic behavior and the additional anisotropic behavior. Further, they noticed most stress stretch curves are in exponential shapes, as a result, the material model is in exponential form.

$$W = c_1 \{ \exp[c_2(I_1 - 3)] - 1 \} + c_3 \{ \exp[\alpha(\alpha - 1)^2] - 1 \} \quad (3.3)$$

where c_1, c_2, c_3 are material constants determined by fitting to experimental data, α is the stretch in fiber direction and is defined as $\alpha^2 = I_4$ where I_4 is material invariants to express the deformation on fiber directions. The definitions are shown in the non-linear elasticity chapter [Eq(2.11)].

Humphrey and Yin model is one of the first material models to consider the anisotropic behavior by adding an additional fiber term which has been widely adopted and modified in the subsequent analysis. Holzapfel model is one of them.

3.1.3 Holzapfel model

As the arterial wall is usually considered as a heterogeneous composite structure with multiple layer features, and each layer has anisotropic behaviors, to account for these behaviors, Holzapfel et al. [55] proposed a most commonly used anisotropic material model which assumes the artery wall material as a fiber-reinforced material with collagen fiber orientations render the material orthotropic behavior. As a result, the strain energy W is split into two parts, W_{iso} associated with isotropy which is mostly elastin matrix and W_{aniso}

associated with anisotropy which is due to the collagen fibers.

$$W = W_{\text{iso}} + W_{\text{aniso}} \quad (3.4)$$

which can be further specified as

$$W = \mu(I_1 - 3) + \frac{k_1}{2k_2} \sum_{i=4,6} \{\exp[k_2(I_i - 1)^2] - 1\} \quad (3.5)$$

where μ, k_1 are stress-like material parameter and k_2 is dimensionless material constant. I_1 is material invariant, I_4, I_6 indicate the material invariants to express the deformation on fiber directions. The definitions are shown in the non-linear elasticity chapter [Eq(2.11)].

The Holzapfel material model is sufficient to capture the basic mechanical behavior of soft tissues in the experiments, and for multi-layer structure with different mechanical response, the same material model can still be applied with different sets of material parameter for each layer. Holzapfel model requires relatively fewer material parameters and makes it very useful in the material simulation.

Many recent models are modified based on the Holzapfel model, of which, Baek et al. [7] added mass related terms to consider material mass changes over time. Driessen et al. [27] and Watton et al. [139] modified the I_i terms to be a function related to fiber angle and fiber length respectively to account for the fiber geometry changes over time.

3.1.4 Baek and Humphrey model

Baek et al. [7] considered each material constituents k : individual strain-energy function W^k , rates of mass density production m^k , and survival functions $Q^k \in [0, 1]$ and $q^k \in [0, 1]$ that account for the half-lives of collagen

fibers. They propose, for each constituent, the strain energy function takes the form of:

$$w^k(s) = \frac{M^k(0)}{\rho(s)} Q^k(s) W^k(\lambda_{n(0)}^k(s)) + \int_0^s \frac{m^k(\tau)}{\rho(s)} q^k(s - \tau) W^k(\lambda_{n(\tau)}^k(s)) d\tau \quad (3.6)$$

where M^k are apparent mass densities defined per surface area and $\lambda_{n(\tau)}^k$ are stretches relative to evolving natural configurations defined at the time of deposition $\tau \in [0, s]$. The values of mass production $m^k(\tau)$ and mass survival $q^k(s)$ depend on collagen half lives and stress values.

In the following studies, Sheidaei et al. [113], Wilson et al. [142] and Valentin et al. [49, 128, 129, 130, 131] employed similar formulation and applied to AAA analysis.

3.1.5 Watton and Hill model

Watton et al. [139] paid special attention to the geometry change of collagen fibers over a long period of time. Based on their theory, as the aneurysm develops, the length of collagen fiber under stress free conditions gets longer over time to prevent extreme stretches in fibers and the stretch of collagen fibers tends to be maintained at a certain value. They modified the Holzapfel model and proposed a strain energy function in the form of:

$$W = c(\epsilon_{11} + \epsilon_{22} + \epsilon_{33}) + \sum k(\exp(a\epsilon_c^2) - 1) \quad (3.7)$$

which contrary to the standard I_4 term in Holzapfel model, the Green strain ϵ_c is related to the recruitment factor r and has the form $\epsilon_c = [\epsilon_e + (1 - r^2)/2]/r^2$, where r is the recruitment factor which quantifies the prestretch

required for the collagen fiber to be straightened and ϵ_e is the Green strain of the elastin resolved in the fiber direction.

Watton and Hill model focuses more on the collagen fiber terms and they assume collagen fibers are the major load bearers, the change of which leads to the expansion of artery and causes the dilation.

3.1.6 Volokh model

Volokh [134] introduced a growth and failure model. The growth is done within the framework of continuum mechanics based on the one-to-one mapping of material configurations during the tissue evolution, and the constitutive description of failure is based on the concept of energy limiters. The model has the strain energy function in the form of:

$$\psi(t) = \int_{-\infty}^t g(t, t_{dp}) \dot{m}(t_{dp}) f(t, t_{dp}) dt_{dp} \quad (3.8)$$

where \dot{m} is a dimensionless rate of the constituent production; f is the strain energy of the deposited constituent; t_{dp} is the time of constituent deposition and $g(t, t_{dp})$ is life cycle function.

They assumed isotropic development of aneurysm and considered averaged incompressible continuum, and model fiber deposition and failure by using the following strain energy: $f = \phi\{1 - \exp[-W/\phi]\}$, where ϕ is the energy limiter, which is the bond energy for the particle potential, and W is the strain energy of intact (without failure) material.

This model has been applied to the simulation of thin axisymmetric membranes.

3.1.7 Other models

During the attempts to simulate the biological tissue mechanical behaviors, there were many material models proposed, of which, Rivlin and Saunders [104] proposed the Polynomial model, and it's been modified by the following works by Chang et al. [15], Hartmann and Neff [51] and Laksari et al. [71]. Yeoh [145] developed the hyperelastic material model which depends on the first strain invariant. Varga model and Gent model by Gent [45] are also widely used on different purposes of simulation. Gasser et al.[42, 43, 44] proposed a damage model based on the histology studies and implemented into FEM simulation. Fillinger et al. [34] and Venkatasubramaniam et al. [133] focused on the peak wall stress and they found the stress is a more significant factor than maximum diameter when predicting AAA ruptures. Vorp et al. [135], Vande Geest et al. [132], Long et al. [76] and other groups took intraluminal thrombus (ILT) into consideration and they believe there is a positive correlation between ILT and AAA rupture risk. Homogenous wall material properties have been primarily assumed in 2D and 3D stress analysis, and combined with patient data, the results were used to predict AAA rupture risk [2, 26, 31, 33, 43, 63, 79, 95, 99, 103, 125]. The specific forms will not be listed.

3.2 Finite element simulation

With the development of computer based simulation software packages, more and more studies use finite element based simulation (FEM) (Figure 5) to estimate the mechanical behaviors of complicated structures and materials. A

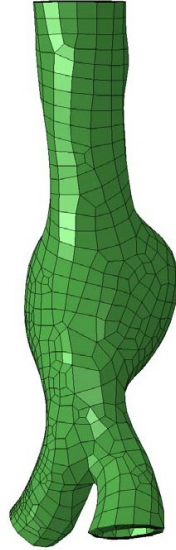


Figure 5: A typical finite element mesh model of AAA. The artery wall has uniform thickness and the geometry is built from patient CT-scan images.

standard FEM output is shown in Figure 6. Similarly to the material model evolution, the FEM models also developed. Many inappropriate assumptions such as uniform wall thickness, stress-free diastolic pressure reference configuration were used in the early simulations or based on the interest of the researches. Later on, more complicated studies including more material constituents such as calcification and thrombus, patient based blood vessel structures and anisotropic material models were adopted. The most representative efforts are listed.

Raghavan et al. [100] introduced the isotropic material model in a uniform thickness structure based on patient AAA CT-Scan image contour. By considering the Von Mises stress, they managed to predict the highest stress zone and the possible location of rupture. In the following studies, Wang et

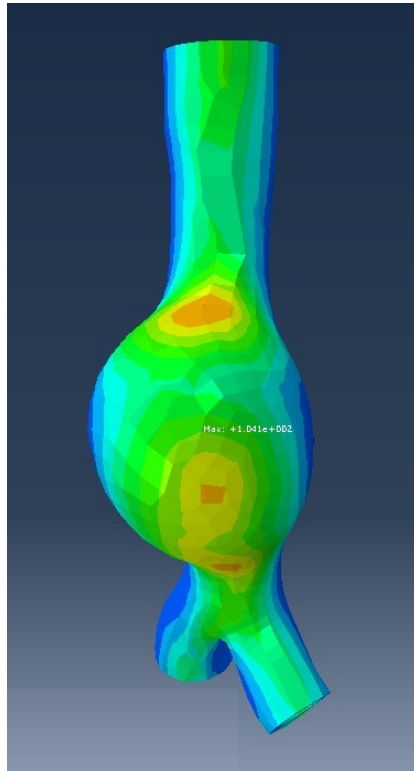


Figure 6: Finite element simulation of artery wall stress. Constant internal pressure is applied to the patient specific blood vessel of uniform wall thickness. The figure shows Von-Mises stress distribution.

al. [138] and Speelman et al. [117] refined the artery wall structure by considering thrombus and calcification respectively. With the development of the simulation packages, anisotropic material models were incorporated in the simulation, the works including [103, 107], which used anisotropic Holzapfel material model and considered multiple fiber orientations. Gasser et al. [43] did a deeper study by considering various thrombus thickness of different patients to find the maximum stress related to the change and predict the rupture risk.

We should be aware that although more complicated material models and patient specific artery wall structures are able to be imported into the FEM, however, due to the high variety of human artery wall constituents in different locations and time as well as complicated blood flow due to various blood pressure and artery wall effects, the localized rupture seems impossible to predict. The FEM simulation is helpful to understand where the larger stress zone is and how the stress distributes under given conditions.

3.3 Mixture theory

The immediate mechanical response of soft tissues has been well studied, even for anisotropic behaviors and different stress stretch relations after unloading. However, as part of tissue evolution mechanism, the tissues change continuously in aspects of material constituents and microstructures. The material evolution under time or different loading environment is not clear, because of which, there's a pressing need to take time factor into the simulation, especially when we need to predict the future tissue behaviors. Naturally, the mixture theory came into our mind. The mixture theory has been applied to the study of biological tissues, cells and bones for decades [66, 67, 108, 116, 121]. The major application of this theory has been focused on modeling the mechanics and migration of mixture components. The recent works consider more about growth and remodeling problems, where growth means the mass exchange of some components and remodeling indicates structure changes of the component, both of which are the result of chemical reactions.

For the growth phenomenon, there are usually two types of growth, sur-

face growth and volume growth. Surface growth implies the deposition of newly generated material onto an existing body, therefore, the reference configuration of the new materials should be defined at each time of material growth and boundary of the mixture should be redefined. Volume growth means changes in the apparent density whose reference configuration was defined at an earlier time. For example, bone growth is a result of new materials deposited on surfaces and artery wall tissue growth is a result of smooth muscle cells, fibers incorporated into the matrix. Negative growth is also possible, which can be caused by degradation. To describe the growth at tissues, cells or bones, because of the complexity of each components which includes different properties, half life rate, the general behavior cannot be added up linearly, and the mixtures must obey the mixture theory. In our study, we will introduce the mixture theory in general and mostly focus on the growth of artery tissues in the later chapters.

The currently widely adopted continuum theory was introduced by Truesdell and Noll [127] and developed by Batchelor [9], in which contrast to a chemical compound, a mixture containing two or more components can be separated and each retains its individual properties no matter separated or mixed. The total mass of the mixture is simply the summation of the mass of each component. As each component will retain its own properties, it must satisfy individual equilibrium and the summation must yield the general classical equation of motion. The study of individual motion makes it possible to consider the mass exchange, the change in linear momentum and stored energy. In the following analysis, we will talk in details. Although the human tissues usually contain a large portion of water, for the purpose

of simulating the mechanical behavior of the mixture, we don't consider the interactions between liquid and solid components.

Skalak [116] and Tozern [126] did great studies in considering stress free configuration evolvement of fiber network structures. The new stress free configuration is achieved either by longer fiber length due to remodeling or increasing amount of units due to growth.

Rodriguez et al. [108] and Taber [122] did further study by assuming the material growth speed depends on the stress level of the objects. The larger stress endured, the faster growth speed is.

Humphrey [58] in the later study suggests the focus should be on the turnover of material constituents and the configurations at which the turnover occurs. The soft tissue is consisted of elastin which serves as an amorphous extracellular matrix, collagen fibers as an oriented major load carrier and water which takes the largest volume portion. In the following studies, Humphrey and Rajagpal [61] introduced a constrained mixture theory, and by using the rule of mixture model, they provided a simplified model to account for the growth and remodeling of soft tissues. Kuhl et al. [70] and Baek and Humphrey [8] applied the theory into computational analysis.

3.4 Remodeling theory

The two major load carrying constituents, elastin matrix and collagen fibers, have very different half lives, of which elastin has a longer half life of about 40 years in human and collagen fiber has a shorter half life about several months to several years [4]. The speed of degradation of elastin is reported increasing during aging and hypertension according to He and Roach [52], because of

which, the elastin matrix is insufficient to carry the pressures. Because the collagen fibers are so stiff when straightened, loss of elastin matrix will be accompanied by a continuous turnover of collagen fibers during the expansion of AAAs. Freestone et al. [38] and Baaijens et al. [6] observed thickening of adventitia of AAA wall via the deposition of collagen fibers which reinforce the artery wall and they concluded the turnover of collagen fibers should be a protective response to the degradation of elastin matrix to restore the balance between deformation and load carrying.

Remodeling of soft tissues is induced by biochemical and biomechanical reactions [37, 50], which will result in changes in tissue microstructure and its mechanical properties. As part of the healing process, the remodelling process initiates in response to tissue damage, excessive loadings and environmental stimuli [18]. As described by Young [146], the wound healing can be broken down into four distinct phases of haemostasis, inflammation, proliferation and tissue remodelling. Haemostasis is an immediate response of the body to prevent exsanguination, the damaged vessels rapidly constrict through the contraction of smooth muscle by increasing cytoplasmic calcium level; During inflammation process, the original mechanical barriers are no longer intact, the neutrophils infiltrate the wound and migrate in sustained level; Proliferation is when the defect begins to be repaired, it incorporates angiogenesis and collagen deposition; Remodelling is the final stage, as the healing can take a relatively long period of time, the balance between synthesis and degradation of the collagen and other proteins should be achieved gradually and the fibers will become well organized.

The remodelling of arteries responding to external changes has been rec-

ognized and studied by various approaches. Fung [41], Rachev and Meister [98] and Rodriguez et al. [108] suggested remodelling based on the change of thickness, opening angles. Driessen et al. [27, 28], Kroon and Holzapfel [69], Menzel [83] put more interest on fiber reorientation during structure evolving. Humphrey [58] and Watton et al. [139] focused on the microstructure addressing the remodelling of collagen and considering the stretched and stress free lengths for a uniaxial model.

Chapter 4

4 Growth and remodeling with application to AAA

4.1 Hyperelasticity

Consider a deformable material, which in the absence of mechanical loads is unstressed and occupies the reference configuration \mathcal{B}_r . The location of a material particle in \mathcal{B}_r is identified by its position vector \mathbf{X} relative to some fixed origin. The material is endowed with a structure characterized by preferred directions typically associated with the mean orientation of two families of collagen fibers identified by unit vectors $\mathbf{M}(\mathbf{X})$ and $\mathbf{M}'(\mathbf{X})$. Let \mathcal{B} denote the configuration of the body after deformation from \mathcal{B}_r , with \mathbf{x} indicating the position occupied by the material particle which was at \mathbf{X} in \mathcal{B}_r .

The theory of hyperelasticity is formulated in terms of a strain-energy function W , defined per unit reference volume, that describes the mechanical response of an elastic material. For an anisotropic solid with two preferred directions W depends, by objectivity, on the deformation gradient \mathbf{F} through the right Cauchy–Green tensor $\mathbf{C} = \mathbf{F}^T \mathbf{F}$ and on the structure tensors $\mathbf{M} \otimes \mathbf{M}$ and $\mathbf{M}' \otimes \mathbf{M}'$ and we write $W = W(\mathbf{C}, \mathbf{M} \otimes \mathbf{M}, \mathbf{M}' \otimes \mathbf{M}')$.

For computational convenience the deformation gradient is decomposed

as

$$\mathbf{F} = J^{1/3} \bar{\mathbf{F}}, \quad (4.1)$$

where $\bar{\mathbf{F}}$ is the isochoric contribution to the deformation satisfying $\det \bar{\mathbf{F}} = 1$ and $J = \det \mathbf{F}$. Note that J is positive and relates an infinitesimal volume element dv in \mathcal{B} to its counterpart dV in \mathcal{B}_r via

$$dv = JdV. \quad (4.2)$$

Associated with the decomposition (4.1) is the isochoric right Cauchy–Green tensor $\bar{\mathbf{C}} = \bar{\mathbf{F}}^T \bar{\mathbf{F}}$. Then, the dependence of W on \mathbf{C} is generalized into dependence on $\bar{\mathbf{C}}$ and J such that

$$\bar{W}(\bar{\mathbf{C}}, J, \mathbf{M} \otimes \mathbf{M}, \mathbf{M}' \otimes \mathbf{M}') = W(\mathbf{C}, \mathbf{M} \otimes \mathbf{M}, \mathbf{M}' \otimes \mathbf{M}'). \quad (4.3)$$

To solve the governing equations numerically, it is common practice to decompose the energy function into a part that depends on $\bar{\mathbf{C}}$ and on the structure tensors, and a part that depends on J . This can be written as

$$\bar{W} = \bar{W}_{\text{iso}}(\bar{\mathbf{C}}, \mathbf{M} \otimes \mathbf{M}, \mathbf{M}' \otimes \mathbf{M}') + \bar{W}_{\text{vol}}(J), \quad (4.4)$$

where \bar{W}_{iso} and \bar{W}_{vol} denote, respectively, the isochoric (volume-preserving) and dilatational (volumetric) contributions.

The material is said to be isotropic if the strain energy is an isotropic function of the three tensors $\mathbf{C}, \mathbf{M} \otimes \mathbf{M}, \mathbf{M}' \otimes \mathbf{M}'$. Therefore, as elaborated by Spencer [118], the integrity basis in three dimensions is given by the invariants

$$I_1 = \text{tr} \mathbf{C}, \quad I_2 = \frac{1}{2}[I_1^2 - \text{tr}(\mathbf{C}^2)], \quad I_3 = \det \mathbf{C} \equiv J^2, \quad (4.5)$$

and

$$I_4 = \mathbf{M} \cdot (\mathbf{C}\mathbf{M}), \quad I_5 = \mathbf{M} \cdot (\mathbf{C}^2\mathbf{M}), \quad I_6 = \mathbf{M}' \cdot (\mathbf{C}\mathbf{M}'), \quad I_7 = \mathbf{M}' \cdot (\mathbf{C}^2\mathbf{M}'). \quad (4.6)$$

Alternatively, if the energy is taken as the sum of isochoric and dilatational parts, the invariants are replaced by the isochoric counterparts together with J . Hence, by replacing \mathbf{C} with $\bar{\mathbf{C}}$ in the definitions (4.5) and (4.6) we obtain $\bar{I}_3 = 1$ and

$$\bar{I}_i = \begin{cases} J^{-2/3} I_i, & i = 1, 4, 6, \\ J^{-4/3} I_i, & i = 2, 5, 7, \end{cases} \quad (4.7)$$

where an overbar now identifies the isochoric invariants. It follows that relation (4.3) has the alternative form

$$\bar{W}(\bar{I}_1, \bar{I}_2, \bar{I}_4, \bar{I}_5, \bar{I}_6, \bar{I}_7, J) = W(I_1, I_2, I_3, I_4, I_5, I_6, I_7). \quad (4.8)$$

4.2 Fiber deposition and remodeling

Fiber deposition and remodeling are often described as two independent events, which may be a simplifying assumption. Therefore, in [75] a general theory is developed that connects the two events and is used to simulate the axisymmetric expansion of an abdominal aortic aneurysm. In this chapter, for completeness, only a summary of the main ingredients of the theory is included.

Consider a mixture with constituents elastin and oriented collagen to represent the aortic wall with the mechanical contribution of smooth muscle cells being omitted, as in [54, 139]. In the reference configuration the mixture occupies the region \mathcal{B}_r and, at time t , the current configuration $\mathcal{B}(t)$.

Following [7, 61, 68, 69], the variable t is used to identify all admissible configurations. Specifically, prior to $t = 0$ the vessel is in a mechanobiologically stable regime, where a loss of existing material is compensated by the production of new material without inducing a permanent dilatation [20, 21]. By contrast, for $t > 0$ the vessel is in a mechanobiologically unstable regime where a minor loss of wall material or a small increase in blood pressure may initiate an aneurysm formation.

The reference location of the constituent i is identified by the position vector \mathbf{X}^i and the location at time t by the function χ^i such that

$$\mathbf{x} = \chi^i(\mathbf{X}^i, t). \quad (4.9)$$

At time t , therefore, all constituents of the mixture occupy the same location \mathbf{x} and, by definition, experience the same deformation.

For what follows it is convenient to recall the phenomenon of fiber remodeling, which is defined as a continuous adaptation of the microstructure and is often described in terms of a recruitment variable r , see detailed discussions in [75, 139]. It represents the macroscopic stretch of the mixture, in the direction of the oriented fibers, when the collagen begin to bear load.

At time τ , where $0 < \tau < t$, the mixture occupies the configuration $\mathcal{B}(\tau)$ with the deformation relative to \mathcal{B}_r defined by the gradient $\mathbf{F}(\tau)$. A new collagen fiber is now deposited with deposition stretch equal to the stretch of the mixture in the fiber direction. Imagine that the material is now unloaded from $\mathcal{B}(\tau)$ to the reference configuration \mathcal{B}_r . The newly deposited fiber ceases to carry load in an intermediate configuration $\mathcal{B}_0(\tau)$ and, upon further unloading, assumes a wavy shape. The deformation gradient in the intermediate configuration, $\mathbf{F}_r(\tau)$, relative to the reference configuration is

obtained as

$$\mathbf{F}_r(\tau) = (\mathbf{F}^c(\tau))^{-1} \mathbf{F}(\tau), \quad (4.10)$$

where the superscript ^c stands for collagen and $\mathbf{F}^c(\tau)$ specifies the corresponding elastic deformation with respect to the intermediate configuration, see Fig. 2 in [75].

The collagen fiber, which was deposited at time τ continuously adapts its microstructure as the mixture evolves from $\mathcal{B}(\tau)$ to the current configuration $\mathcal{B}(t)$. If the mixture is now unloaded, the fiber will become stress-free in an evolved intermediate configuration, denoted $\mathcal{B}_0(t, \tau)$. The deformation gradient of the mixture in the intermediate configuration $\mathcal{B}_0(t, \tau)$, relative to the reference configuration \mathcal{B}_r , is then obtained as

$$\mathbf{F}_r(t, \tau) = (\mathbf{F}^c(t, \tau))^{-1} \mathbf{F}(t). \quad (4.11)$$

Relations (4.10) and (4.11) can be combined to obtain the elastic deformation of a fiber in the current configuration $\mathcal{B}(t)$ with respect to the evolving intermediate configuration $\mathcal{B}_0(t, \tau)$. The corresponding gradient is given by

$$\mathbf{F}^c(t, \tau) = \mathbf{F}(t) \mathbf{F}^{-1}(\tau) \mathbf{F}^c(\tau) \mathbf{F}_r(\tau) \mathbf{F}_r^{-1}(t, \tau), \quad (4.12)$$

where we note that $\mathbf{F}_r(t, \tau)$ depends on $\mathbf{F}_r(\tau)$.

4.3 Mass balance

Growth is associated with a local increase in mass, achieved via the production of new material that exceeds the removal of existing material. This suggests that the mass balance at time t of constituent i includes density production and survival functions denoted, respectively, $m^i(\mathbf{x}, t)$ and $Q^i(t, \tau)$.

The latter defines the amount of constituent i , produced at time τ , that survives to the current time t . Then, for use in numerical simulations, the mass balance equation is expressed in Lagrangian form by

$$\rho_r^i(\mathbf{x}, t) = \rho_r^i(\mathbf{x}, 0) Q^i(t, 0) + \int_0^t m_r^i(\mathbf{x}, \tau) Q^i(t, \tau) d\tau, \quad (4.13)$$

where $\rho_r^i(\mathbf{x}, t)$ is the mass density at time t defined per unit reference volume of the mixture, and $\rho_r^i(\mathbf{x}, 0)$ is the density in the mechanobiological stable state. The referential density production term $m_r^i(\mathbf{x}, \tau) = J m^i(\mathbf{x}, \tau)$, with J defined in (4.2).

Note that the mixture is taken as incompressible prior to the initiation of growth, therefore $\rho_r^i(\mathbf{x}, 0) = \rho^i(\mathbf{x}, 0)$. At time $t > 0$, the mass density $\rho^i(\mathbf{x}, t)$ is determined by the mass of constituent i per current volume of mixture. The total mass density is then obtained by

$$\rho(\mathbf{x}, t) = \sum_i \rho^i(\mathbf{x}, t), \quad (4.14)$$

which, following [7, 128, 131], is assumed *constant*, i.e. $\rho(\mathbf{x}, t) = \rho(\mathbf{x})$. However, the rate of mass production of one constituent is not, in general, equal to the rate of removal of another and therefore $\sum m^i \neq 0$.

4.4 Energy function

In the theory of mixtures the Cauchy stress $\boldsymbol{\sigma}$ is taken as the sum of the stresses in each constituent [7, 128]. We obtain

$$\boldsymbol{\sigma}(t) = J^{-1} \mathbf{F}(t) \frac{\partial W(t)}{\partial \mathbf{F}(t)} = J^{-1} \mathbf{F}(t) \frac{\partial \sum_i W^i(t)}{\partial \mathbf{F}(t)}, \quad (4.15)$$

where $W^i(t)$ denotes the strain energy density of constituent i , $\mathbf{F}(t)$ is the deformation gradient of the mixture in the current configuration $\mathcal{B}(t)$ relative to the reference configuration \mathcal{B}_r and $J = \det \mathbf{F}(t)$.

Following a common practice in the theory of growth, the energy density W is expressed in terms of the internal energy U , which is defined per unit mass. It follows that the energy density of constituent i can be written as

$$W^i(t) = \rho_r^i(0) Q^i(t, 0) U^i(\mathbf{F}^i(t)) + \int_0^t m_r^i(\tau) Q^i(t, \tau) U^i(\mathbf{F}^i(t, \tau)) d\tau, \quad (4.16)$$

where $U^i(\mathbf{F}^i(t))$ represents the internal energy at time t of constituent i , produced in the homeostatic state. The tensor $\mathbf{F}^i(t)$ identifies the associated deformation relative to the reference configuration \mathcal{B}_r . Likewise, $U^i(\mathbf{F}^i(t, \tau))$ defines the internal energy at time t of constituent i produced at time τ subject to the deformation gradient $\mathbf{F}^i(t, \tau)$.

4.5 Application to aneurysm development

The theory is now adapted to model the non-axisymmetric dilatation of an abdominal aorta, triggered by a local deterioration of the material properties. Following the development in [75], a thick-walled tube with circular cross-sectional area is taken as the reference configuration. This is defined in terms of cylindrical polar coordinates (R, Θ, Z) by

$$A \leq R \leq B, \quad 0 \leq \Theta \leq 2\pi, \quad -L \leq Z \leq L, \quad (4.17)$$

where A, B denote the internal and external radii and $2L$ the length of the tube. In the homeostatic state the tube is subject to a constant internal pressure and axial stretch and maintains the axisymmetric geometry. It is

specified in terms of cylindrical polar coordinates (r, θ, z) as

$$a \leq r \leq b, \quad 0 \leq \theta \leq 2\pi, \quad -l \leq z \leq l, \quad (4.18)$$

where a, b are the internal and external radii and $2l$ the current length. Here, the variable r denotes the cylindrical polar coordinate and should not be confused with the recruitment variable r introduced in Section 4.2.

4.5.1 Constitutive model

The form (4.4) is now replaced by

$$\bar{W}(t) = \sum_i \bar{W}_{\text{iso}}^i(t) + \bar{W}_{\text{vol}}(t) = \sum_i \rho_r^i(t) \bar{U}_{\text{iso}}^i(t) + \bar{W}_{\text{vol}}(t), \quad (4.19)$$

where the energy \bar{W}_{iso} consists of contributions from the isotropic base matrix and from the two families of collagen fibers. A purposely written user subroutine is developed and the commercially available finite element package ABAQUS is used to solve the corresponding equations.

4.5.2 Isotropic matrix

Wilson et al. [143] and Valentin et al. [131] report that elastin is not continuously produced in a mature arterial wall. Therefore, specializing the formulation (4.16) to elastin gives

$$\bar{W}_{\text{iso}}^e(t) = \rho_r^e(0) Q^e(t, 0) \bar{U}_{\text{iso}}^e(\bar{\mathbf{F}}(t)), \quad (4.20)$$

where the superscript e refers to elastin. Following standard practice, the mechanical response is specified by

$$\bar{U}_{\text{iso}}^e(t) = \frac{1}{2} c^e (\bar{I}_1(t) - 3), \quad (4.21)$$

where c^e is a material parameter [54, 128, 130, 131]. The definition of constrained mixtures implies that the deformation of the matrix material coincides with the macroscopic deformation [75]. The deformation of elastin in the current configuration relative to the reference configuration is then described by $\mathbf{F}(t)$. The first isochoric invariant is defined in (4.7) and is calculated as $\bar{I}_1(t) = \text{tr} \bar{\mathbf{C}}(t)$, where $\bar{\mathbf{C}}(t) = \bar{\mathbf{F}}^T(t) \bar{\mathbf{F}}(t)$ and $\bar{\mathbf{F}}(t) = J^{-1/3} \mathbf{F}(t)$.

Prior to the initiation of growth, the vessel wall is in a stable regime where any loss of existing material is naturally compensated by production of new [20, 21, 22]. In this study we assume that the unstable regime is initiated by matrix degradation over an axial distance defined by $\pm L_d$. The geometric extension and the rate of degradation is detailed by the function $Q^e(t, 0)$. To keep equations manageable, assume that degradation is independent of the radial distance R . Specifically, for $|Z| \leq L_d/3$ and for $0 \leq \Theta \leq 150^\circ$, let that the survival function have the form

$$Q^e(t, 0) = \left[1 - q^e \left(1 - \frac{\Theta}{150} \right)^2 \right]^t, \quad (4.22)$$

where q^e is a material constant and $\Theta = 0$ defines the region of maximum degradation. For $L_d/3 \leq |Z| \leq L_d$ and for $0 \leq \Theta \leq 150^\circ$ use

$$Q^e(t, 0) = \left\{ 1 - q^e \left[1 - \left(\frac{|Z| - L_d/3}{2L_d/3} \right)^2 \right] \left[1 - \frac{\Theta}{150} \right]^2 \right\}^t. \quad (4.23)$$

For $150^\circ \leq \Theta \leq 180^\circ$ or for $|Z| \geq L_d$ the function $Q^e(t, 0) = 1$ and therefore no degradation occurs. Age-related degradation of elastin is, in general, not significant and therefore not included.

4.5.3 Collagen fibers

The referential mass density of constituent i at time t is given by (4.13).

When specialized to collagen we obtain

$$\rho_r^c(t) = \rho_r^c(0) Q^c(t, 0) + \int_0^t m_r^c(\tau) Q^c(t, \tau) d\tau, \quad (4.24)$$

where $m_r^c(\tau)$ denotes the amount of collagen production at time τ and $Q^c(t, \tau)$ is the survival function. The isochoric contribution to the energy (4.19) is then computed by evaluating

$$\bar{W}_{\text{iso}}^c(t) = \rho_r^c(0) Q^c(t, 0) \bar{U}_{\text{iso}}^c(\bar{\mathbf{F}}^c(t, 0)) + \int_0^t m_r^c(\tau) Q^c(t, \tau) \bar{U}_{\text{iso}}^c(\bar{\mathbf{F}}^c(t, \tau)) d\tau. \quad (4.25)$$

The internal energy of two families of oriented collagen fibers is often specified by

$$\bar{U}_{\text{iso}}^c(\bar{\mathbf{F}}^c(t, \tau)) = \frac{k^c}{2k} \sum_{j=4,6} \left\{ \exp \left[k (\bar{I}_j - 1)^2 \right] - 1 \right\}, \quad (4.26)$$

where k^c is a stress-like material parameter k is a dimensionless constant [2, 54, 92, 131]. The isochoric invariants \bar{I}_4, \bar{I}_6 are defined in (4.7) and have the explicit forms

$$\bar{I}_4 = \mathbf{M} \cdot [\bar{\mathbf{C}}^c(t, \tau) \mathbf{M}], \quad \bar{I}_6 = \mathbf{M}' \cdot [\bar{\mathbf{C}}^c(t, \tau) \mathbf{M}'], \quad (4.27)$$

where the unit vectors \mathbf{M}, \mathbf{M}' are defined in Section 4.1. The tensor $\bar{\mathbf{C}}^c(t, \tau) = (\bar{\mathbf{F}}^c(t, \tau))^T \bar{\mathbf{F}}^c(t, \tau)$, where $\bar{\mathbf{F}}^c(t, \tau)$ is the isochoric counterpart of $\mathbf{F}^c(t, \tau)$, see Equation (4.12). Equivalent steps are followed to determine the energy of collagen that is produced in the homeostatic state and remains part of the mixture at time t . The invariants (4.27) are calculated by replacing $\bar{\mathbf{C}}^c(t, \tau)$ with $\bar{\mathbf{C}}^c(t, 0) = (\bar{\mathbf{F}}^c(t, 0))^T \bar{\mathbf{F}}^c(t, 0)$.

The survival functions $Q^c(t, 0)$ and $Q^c(t, \tau)$ account for the deterioration of collagen and, following [142, 143], are take as

$$Q^c(t, \tau) = \exp \left[- \int_{\tau}^t \bar{q}^c(\bar{\tau}) d\bar{\tau} \right], \quad (4.28)$$

where $\bar{q}^c(\bar{\tau})$ is a time- and stretch-dependent degradation function. The explicit formulation used in this study is

$$\bar{q}^c(\bar{\tau}) = q^c \left(1 + w_u^c \Delta T_{\lambda}^c(\bar{\tau})^2 \right), \quad (4.29)$$

where q^c is connected to the half-life of collagen in the homeostatic state by $t_{1/2}^{c,h} = \ln(2)/q^c$. The function w_u^c is taken as $w_u^c = (t_{1/2}^{c,h}/t_{1/2}^{c,u} - 1)$, where $t_{1/2}^{c,u}$ is the half-life of collagen in the unloaded state. The expression for $\Delta T_{\lambda}^c(\bar{\tau})$ is given by

$$\Delta T_{\lambda}^c(\bar{\tau}) = \frac{\lambda^c(\bar{\tau}) - \lambda_h^c}{\lambda_h^c}, \quad (4.30)$$

where $\lambda^c(\bar{\tau})$ is the stretch at $\bar{\tau} \in [\tau, t]$ of the collagen fiber deposited at τ and λ_h^c is the corresponding stretch in the homeostatic state. Equation (4.30) entails a faster deterioration of collagen with increasing fiber stretch. For clarity of presentation, the dependence of the stretch on the radial location is not shown in (4.30).

Data show that collagen content of the arterial wall increases with aneurysm dilatation [93]. Hence, it is reasonable to assume that the production of collagen depends on the fiber stretch, so that

$$m_r^c(\tau) = m_r^c(0) \left(1 + k_{\lambda}^c \Delta T_{\lambda}^c(\tau) \right), \quad (4.31)$$

where $m_r^c(0)$ is the rate of production prior to aneurysm formation [142, 143]. The form of $\Delta T_{\lambda}^c(\tau)$ is identical to (4.30) with $\bar{\tau}$ replaced by τ and k_{λ}^c is a scaling factor.

The intermediate configuration of the mixture evolves with fiber remodeling as elaborated in Section 4.2. To implement the model within a finite element framework, expressions for $\mathbf{F}_r(\tau)$ and $\mathbf{F}_r(t, \tau)$ are needed in terms of the recruitment variable r . Keeping the fiber orientations \mathbf{M} constant during the deformation from the reference to the intermediate configuration, we use

$$\begin{aligned}\mathbf{F}_r(\tau) &= r(\tau)\mathbf{M} \otimes \mathbf{M} + \frac{1}{\sqrt{r(\tau)}} (\mathbf{I} - \mathbf{M} \otimes \mathbf{M}), \\ \mathbf{F}_r(t, \tau) &= r(t, \tau)\mathbf{M} \otimes \mathbf{M} + \frac{1}{\sqrt{r(t, \tau)}} (\mathbf{I} - \mathbf{M} \otimes \mathbf{M}).\end{aligned}\quad (4.32)$$

Similarly, the intermediate configuration of the fibers aligned with the unit vector \mathbf{M}' is defined by the recruitment variable r' and by expressions similar to (4.32). In what follows, all relation involving r carry over directly to r' .

The microstructure of collagen adapts continuously with the expanding aneurysmal wall, correspondingly, the recruitment variable changes. This is reflected by

$$r(t, \tau) = r(\tau) + \int_{\tau}^t r^c(\bar{\tau}) \Delta T_{\lambda}^c(\bar{\tau}) d\bar{\tau}, \quad (4.33)$$

where the function $\Delta T_{\lambda}^c(\bar{\tau})$ is defined in (4.30) and $r^c(\bar{\tau})$ is a time dependent scaling function of the form

$$r^c(\bar{\tau}) = 0.6 - \frac{0.4}{\pi} \arctan(5\bar{\tau} - 21.25). \quad (4.34)$$

It follows that $\mathbf{F}_r(t, \tau)$ depends on $\mathbf{F}_r(\tau)$, as expected. Remodeling is initiated starting from the homeostatic state where the recruitment variable $r(0)$ is constant and known [75].

4.5.4 Volumetric contribution

The volumetric contribution $\bar{W}_{\text{vol}}(t)$ to the total stored energy (4.19) has the form

$$\bar{W}_{\text{vol}}(t) = \frac{1}{2} \kappa \left(\frac{J(t)}{J(t^-)} - 1 \right)^2, \quad (4.35)$$

where $J(t)$ accounts for the volume change due to growth, $J(t^-)$ is the change during the previous time increment and κ is penalty parameter to enforce the volumetric response in the homeostatic state [1, 131]. The special case of isotropic growth is discussed in, for example, [12, 32].

4.6 Computational model and results

The theory, described in Section 4.1 and specialized in Section 4.5 to model the formation of a non-axisymmetric aneurysm, is implemented into a non-linear finite element package as a user defined subroutine. In this section, for completeness of presentation, the main aspects of the computational model are summarized and we refer to [75] for details.

4.6.1 Model parameters

A thick-walled cylindrical tube with inner and outer radii $A = 10$ mm and $B = 12$ mm and of total length $2L = 120$ mm is taken as the reference geometry of the finite element model. From equations (4.22) and (4.23) follows that the deformed shape has a plane a symmetry, hence only half of the tube is considered. The model uses 18,648 hexahedral elements connected at 24,130 nodes, with four elements through the thickness. The boundary conditions at the entrance and exit allow radial expansion and no axial dis-

placements. Therefore, prior to aneurysm formation the axial stretch $\lambda_z = 1$ and constant. A uniform pressure of 120 mmHg (16 kPa) is applied to the inner surface to represent the in vivo load condition. Time-dependent pressure measurements in rigid phantoms and the corresponding calculated wall stress distribution are reported in [3].

4.6.2 Material parameters

In the homeostatic state the overall density is uniform and constant and the convenient notation $\rho_r = \rho(\mathbf{x}, 0)$ is introduced, see (4.14). In this model, similar to [143], the initial mass fractions of elastin $\rho_r^e(0)$ and collagen $\rho_r^c(0)$ are specified in terms of ρ_r .

The shear stiffness and the initial density of elastin as well as the values needed to define material degradation are summarized in Table 2. Model parameters for collagen are given in Table 3. These include the initial density, the values to define the stored energy (4.26), the survival function (4.28), collagen density production (4.31) and fiber recruitment (4.33). The parameters that describe collagen degradation and density production are based on results in [72, 140, 143]. The angle φ defines the orientations of the unit vectors \mathbf{M} and \mathbf{M}' by

$$\mathbf{M} = \cos \varphi \mathbf{E}_\Theta + \sin \varphi \mathbf{E}_Z, \quad \mathbf{M}' = \cos \varphi \mathbf{E}_\Theta - \sin \varphi \mathbf{E}_Z, \quad (4.36)$$

where \mathbf{E}_Θ and \mathbf{E}_Z are unit basis vectors in the circumferential and axial directions, respectively. The penalty parameter in the volumetric contribution energy (4.35) is taken as $\kappa = 100,000$ kPa.

Table 2: The initial mass fraction, the parameters of the energy contribution (4.21) and of the survival functions (4.22) and (4.23). The overall density $\rho_r = 1050 \text{ kg/m}^3$.

Summary of material parameters for elastin			
$\rho_r^e(0) \text{ (kg/m}^3\text{)}$	$c^e \text{ (J kg}^{-1}\text{)}$	q^e	$L_d \text{ (mm)}$
$0.6 \rho_r$	120	0.1	45

Table 3: Material parameters of collagen that define the energy (4.26), the survival function (4.28), the collagen production (4.31) and the recruitment function (4.33). The overall density $\rho_r = 1050 \text{ kg/m}^3$.

Summary of material parameters for collagen							
$\rho_r^c(0) \text{ (kg/m}^3\text{)}$	$k^c \text{ (J kg}^{-1}\text{)}$	k	$\varphi \text{ (}^\circ\text{)}$	$t_{1/2}^{c,h} \text{ (years)}$	$t_{1/2}^{c,u} \text{ (years)}$	k_λ^c	$r(0)$
$0.4 \rho_r$	75.2	11.2	± 15	0.8	0.2	50	1.03

4.6.3 Results

In the homeostatic state, defined by $t \leq 0$, the arterial wall is in a stable regime. At $t = 0$ elastin starts to degrade locally, softens the arterial wall, induces a localized dilatation and an increase in collagen stretch. This stimulates faster degradation of existing and increased deposition of new collagen. At the same time the microstructure adapts to the new environment resulting in a continuous enlargement of the aneurysm bulge.

Figure 7(a) depicts the changes of the outer radius at the most critical region of the abdominal aorta. Results are shown as a function of the axial po-

sition over a twelve-year period with an applied inner pressure of 120 mmHg (16 kPa). The change from the reference to the homeostatic state is much smaller compared to those associated with aneurysm dilatation. For reference, the dashed horizontal line represents the outer diameter $b = 12.94$ mm in the homeostatic state. The results in Fig. 7(b) represent the changes of the outer radius at the location diametrically opposite. Since in this region the material properties do not degrade, the changes are much smaller and also depend on the size of the aneurysm bulge.

Figure 8 shows the mass fractions of elastin and collagen over a twelve-year time frame. Prior to aneurysm formation, in the homeostatic state, the values for elastin and collagen are $\rho_r^e(0) = 0.6\rho_r$ and $\rho_r^c(0) = 0.4\rho_r$ of the reference density $\rho_r = 1050 \text{ kg/m}^3$, respectively. The results clearly show that aneurysm dilatation increases production of collagen and a continuous reduction of elastin. During this time period, the overall mass density of the mixture increases by 9.8% to $\rho_r(\mathbf{x}, 12 \text{ years}) = 1152 \text{ kg/m}^3$.

The stretch of elastin of a healthy and a diseased section of the arterial wall is calculated in the fiber direction and the results are depicted in Fig. 9. The deformation of the healthy tissue is evaluated on the inner wall where the corresponding stretch initially increases from $\lambda^e(0) = 1.09$ to $\lambda^e(4) = 1.105$ and slightly decreases afterwards. These changes occur because the axial stretch of the model is no longer uniform and constant if it contains an expanding aneurysm. Stretches for the diseased section are evaluate on the inner and outer walls of the vessel at the location of maximum dilatation and are shown by solid and dashed lines, respectively.

Adaptation of the collagen microstructure is accelerated by a dilating

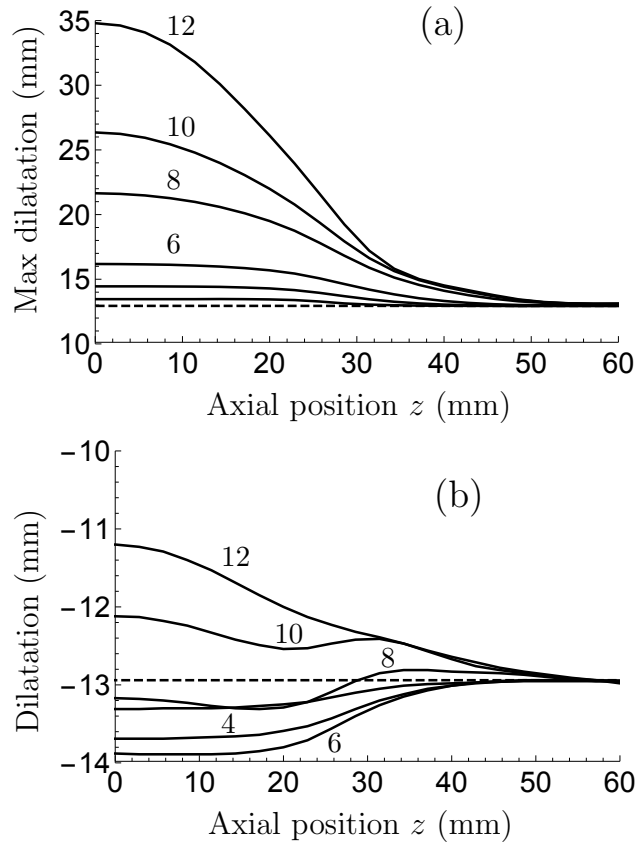


Figure 7: Non-axisymmetric dilatation of an abdominal aneurysm over a twelve-year period. Image (a) shows dilatation of the most critical region as a function of the axial position at 2 years increments. The dashed horizontal lines represent the outer radius $b = 12.94$ mm during the homeostatic state. Image (b) represents the dilation of the region diametrically opposed where no material deterioration occurs.

aneurysm bulge and this is clearly reflected by the results reported in Fig. 10. Stretches are again calculated on the inner wall of the non dilated vessel and on the inner and outer walls at the location of maximum dilatation. The stretch of collagen depends on the intermediate configurations and,

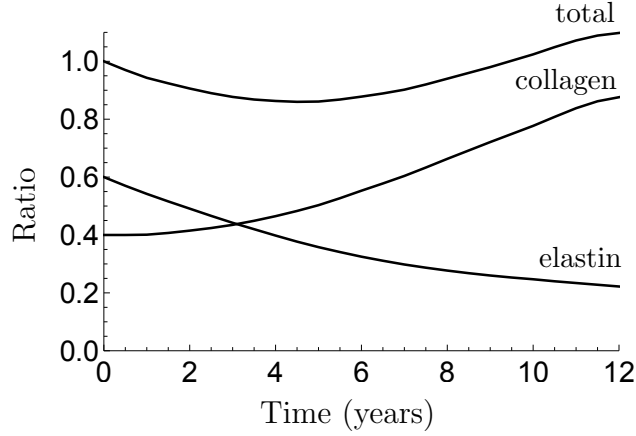


Figure 8: The mass fractions of elastin $\rho_r^e(t)$ and collagen $\rho_r^c(t)$ as a function of time. In the homeostatic state these are $\rho_r^e(0) = 0.6\rho_r$ and $\rho_r^c(0) = 0.4\rho_r$, where the overall reference density $\rho_r = 1050 \text{ kg/m}^3$.

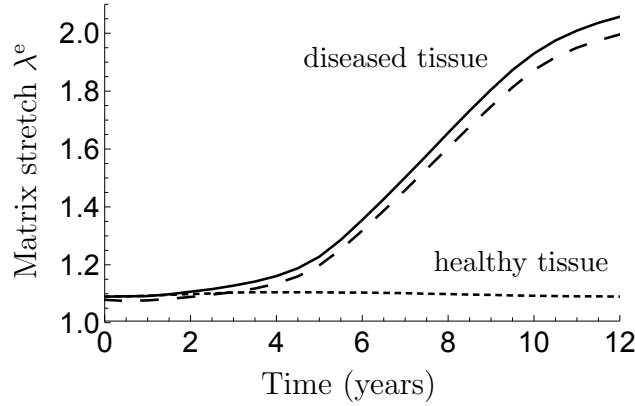


Figure 9: Stretches of the diseased matrix material on the inner and outer vessel walls at the location of maximum dilatation are shown by solid and dashed lines, respectively. The stretch of the healthy material is evaluated on the inner surface.

for healthy tissue, is calculated by $\lambda^c(t) = \lambda^e(t)/r(0)$, where the variable $r(0) = 1.03$ and constant. During dilatation, the intermediate configuration continuously evolves and the fiber stretch does not increase monotonically,

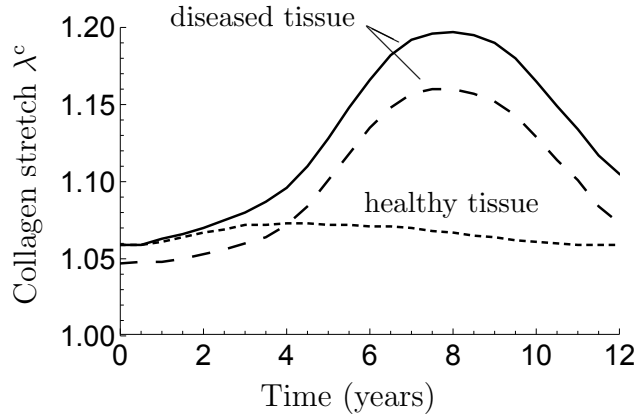


Figure 10: Healthy and remodeled collagen fiber stretches. Diseased fibers are evaluated on the inner and outer vessel walls at the location of maximum dilatation and are shown by solid and dashed lines, respectively. The stretch of the healthy fiber is evaluated on to the inner surface.

compare to Fig. 9. In particular, the collagen stretch at time t is obtained by $\lambda^c(t) = \lambda^e(t)/r(t)$ with the change of the recruitment variable $r(t)$ shown in Fig. 11.

Von Mises stress contour plots are generally used to visualize the stress distributions in the arterial wall. For ease of comparison we also adopt this as our stress measure, which is defined by $\sigma_{\text{vm}} = \sqrt{3\bar{\boldsymbol{\sigma}} : \bar{\boldsymbol{\sigma}}/2}$, where $\bar{\boldsymbol{\sigma}}$ denotes the deviatoric part of the Cauchy stress tensor (4.15). The wall stress distribution on the inner surface of the aneurysmal wall is then visualized in Fig. 12 for two representative times. Eight years after aneurysm initiation the von Mises stress varies between $68 < \sigma_{\text{vm}} < 235$ kPa, after twelve years this range changes to $68 < \sigma_{\text{vm}} < 925$ kPa with the larger value now exceeding tissue strength. During bulge dilatation thinning of the arterial wall occurs and is clearly visible.

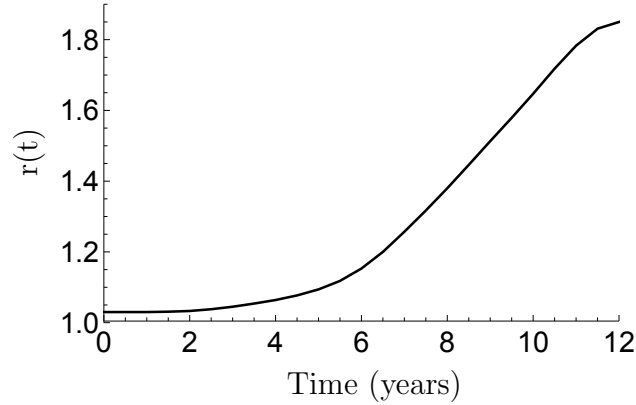


Figure 11: Changes of the recruitment variable $r(t)$ with time. The results show that adaptation of collagen microstructure is amplified by the dilatation of the aneurysmal bulge.

The circumferential Cauchy stress components over the same time period are shown in Fig. 13. The responses of the diseased material are evaluated next to the inner and outer walls where the maximum dilatation occurs and are depicted by solid and dashed lines, respectively. The healthy material response is recorded next to the inner wall and is shown by the dotted line. The change of the axial Cauchy stress component is illustrated as a function of time in Fig. 14. The response of the diseased tissue is again evaluated at the location of maximum dilatation with the values now being almost independent of the radial distance. The axial stress component in the non-dilated section of the tube is essentially constant over the considered time period.

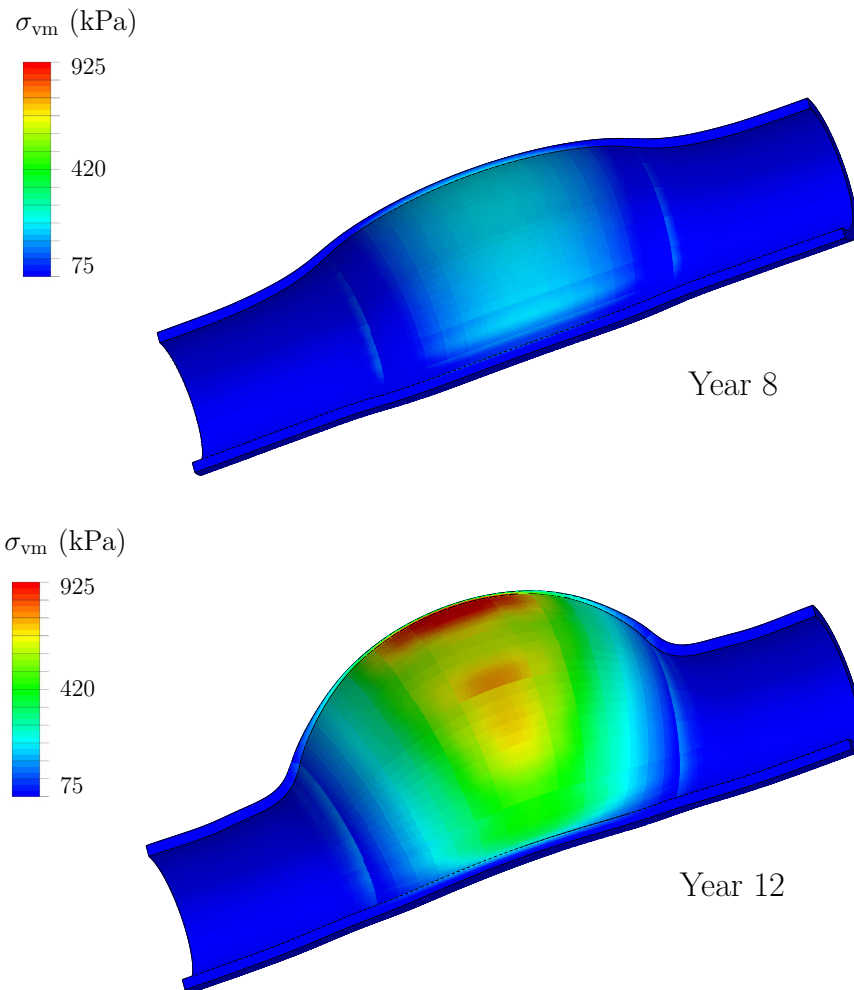


Figure 12: The von Mises stress distributions on the inner surface of a developing non-axisymmetric abdominal aortic bulge with a physiological pressure of 120 mmHg (16 kPa). Images show results for years 8 and 12.

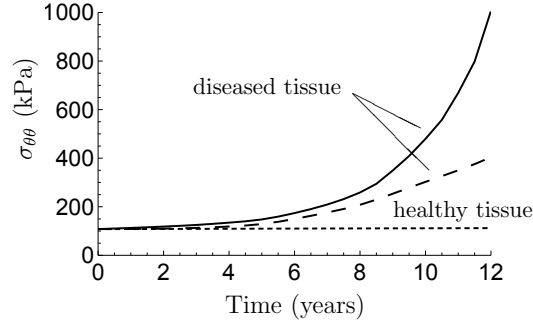


Figure 13: Changes of the circumferential Cauchy stress components of healthy and diseased arterial tissues as a function of time. The responses of the diseased tissue are evaluated next to the inner and outer vessel walls where maximum dilatation occurs and are shown by solid and dashed lines, respectively. The stress of the healthy section is taken next to the inner wall.

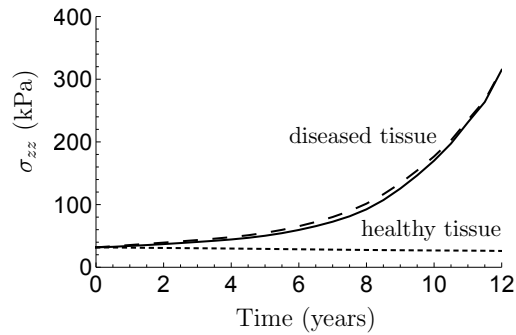


Figure 14: Changes of the axial Cauchy stress components of healthy and diseased arterial tissues. The responses of the diseased material are evaluated next to the inner and outer vessel wall where maximum dilatation occurs and are shown by solid and dashed lines, respectively. The stress of the healthy section is again evaluated next to the inner wall.

Chapter 5

5 Concluding remarks

In this work, a general three-dimensional formulation of the growth and remodeling theory has been implemented into the commercially available finite element package ABAQUS. The user-defined FORTRAN subroutine (UMAT) was used to the simulation of the pressurization of a thick-walled 3D cylinder to study the formation and dilatation of an abdominal aortic aneurysm. We used C3D8R element, a general purpose linear brick element with reduced integration. Compared with the C3D8 element, C3D8R element shares the same shape function but has one integration point located in the middle of the element, which avoids the locking phenomena. Locking in FEM occurs in lower order elements because element kinematics are not able to represent the correct solution. The two most common types of lockings are shear locking and pressure locking, which shearing locking occurs when elements are subjected to bending and pressure locking occurs when material is incompressible. For example, shear locking is observed when first-order solid elements are used to model thin-structures and it's especially true when they are subjected to bending loads.

The model depicts the changes of the outer radius of a dilating abdominal aorta as a function of axial position over a twelve-year period with an applied pressure of 16 kPa (120 mmHg). Numerical results show first the changes from the unloaded reference state with inner radius 10mm and outer radius

12 mm to the homeostatic state with inner radius 10.92mm and outer radius 12.77 mm, then the subsequent increase in radii over time. The time course of bulge development over twelve years is nonlinear, and over the period from years 8 to 12, as the bulge expanded, the maximum von Mises stress increased almost four times, from 235 to 925 kPa (Figure 12). The model also shows the significant changes in the material constituents, which in the normal aorta, the majority of the components is elastin matrix, but in the aneurysm tissue, the elastin matrix decreased greatly to 20%, and the majority constituent is the collagen fibers. This matches the observation by Carmo et al.[14] (Figure 8) that AAAs may have 90% less elastin than normal.

Results show that the mixture theory of growth and remodeling predicts the development of inhomogeneous mechanical properties and dilatation of the diseased section of the arterial wall. We found that the rate of expansion depends primarily on the rate of production and removal of elastin and collagen as well as on the change in microstructure. The degradation of elastin and deposition of collagen fibers with larger recruitment factors result in the dilation of aneurysm. The general three-dimensional formulation adopted in this study allows evaluating both in-plane stress and out-of-plane shear stress distribution in the arterial wall.

The model developed here is the first mathematical model considering both the growth and shapes of fibers in AAA. Abdominal aortic aneurysm simulations considering dilation over a long period of time have been created and analyzed by other literatures as well. Researches done by [7, 128, 129, 143] focus on the production and removal of collagen, and they are further developed to capture pressure-induced changes in geometry and mechanical

behavior in arteries. However, the turnover of existing collagen fibers are not addressed. As pointed out by [58, 101], the continuous microstructure of collagen changes result in the evolution of its stress-free configuration. Watton et al.[139, 140] focused on the collagen waviness changes over time, and introduced the collagen fiber remodeling. They assumed that the stress-driven recruitment factor of the fibers leads to the aneurysm bulge development. Baek et al.[7], Davarani et al.[25], Gleason et al.[46] and Watton et al.[140] did FEM simulation of AAA formation, but limited to the membrane assumption. The impact of other material constituents such as smooth muscle cells, intraluminal thrombus were considered by Baek et al.[7], Zulliger et al.[147].

Our results clearly indicate the mass, shape and distribution of material constituents are all changing, as well as the dilation and peak stress in the artery wall. Although we assume the collagen recruitment factor, mass generation speed and degradation speed are key factors in this model, we don't indicate these are the reasons that cause aneurysm, further histology and pathology studies are quite necessary to find out how or why aneurysm occurs. Furthermore, some of the assumptions such as rate of elastin degradation, collagen growth speed are all based on author's assumption, we tried to consider as many factors as possible, such as duration of aneurysm occurs, the speed of deformation, yet, these assumptions are still in need of modification based on future histology study.

During the development of aneurysm, the strain in elastin becomes fairly large. The assumption of elastic matrices Neo-Hookean SEF may not be valid at this stretch, however, the load carried by elastin at such high stretch

is minor compared to load carried by collagen, so the problem may not be significant to our calculation.

The fiber directions used in our study are in plane. Collagen orientations in the normal aorta, as well as in the aneurysmatic aorta are dispersed [35, 44, 97, 110, 124], and the approximation by two families of collagen fibers is rather conceptual. In addition, also the undulation of collagen fibers is dispersed, and collagen fibers gradually engage when loading the vascular wall. 3D spatial distribution of fibers can be implemented, however, more parameters will be assumed for the model. Given the outputs of current histology study, we think the in-plane fiber assumption should work for now, but we are well aware the real artery wall structure is more complicated than 2D assumptions, more studies should be done to improve the mathematical model.

This model can be applied to multi-layer artery wall, eg. adventitia, media and intima. In this work, the calculation is based on single layer structure, because currently we are more interested in how this model works in structure rather than simulating a complicated realistic aneurysm wall. However, we did present a thick-walled model to simulate the aneurysm growth, which is because during the growth of artery wall, there will be volume change which makes the change of wall thickness non-negligible. The numerical calculation results meet our expectation quite well, the material gets softer with time which results in the expansion of artery but gets stiffer faster to prevent further larger deformation.

Parameters used in this work are based on a specific patient sample. In order to fit the model outputs into other specific patient aneurysm develop-

ment, several studies or experiments need to be done. For example, in order to get better ideas of how much the structure changed during the aneurysm development, a sequence of histology studies should be done to take a closer look at the mass and shape changes of fibers; patient CT scan series should be helpful too, which together with the histology study can narrow down the range of parameters and improve the SEF assumption.

Related to the biomechanics and biology of AAAs, the most pressing need is developing computational models that can predict the evolving artery wall stress and strength based on clinically available data, such as:

1. Determine why and how male gender, smoking, atherosclerosis are more susceptible to developing AAAs;
2. Identify a suitable way to present the stress for characterizing multidimensional state of stress locally, which can help identify the failure criteria, thus to quantify the rupture risk;
3. Evaluate collagen fibers evolution, including mass, orientation, dimension and how they change with aneurysm progression.

There is a pressing need to develop a patient-specific model that can better predict the aneurysm development or rupture, we hope our approach will stimulate the experimental and computational research that will contribute to this long term goal.

A Appendix A

A.i ABAQUS input file code

```

*Heading
** Job name: Finemesh Model name: Model-1
** Generated by: Abaqus/CAE 6.11-2
*Preprint, echo=NO, model=NO, history=NO, contact=NO
**
**'Read in material parameters'**
*Parameter
*INCLUDE, Input='UMAT parameters'.inp
** PARTS
**
*Part, name=Part-1
*End Part
**
** ASSEMBLY
**
*Assembly, name=Assembly
**
**'Define model nodes and elements'**
*Instance, name=Part-1-1, part=Part-1
*Node
    1,      10.,      0.,      60.
    2,  9.98716545,  0.506491661,  60.
    3,  9.94869328,  1.01168323,  60.
    ...
 19358,  1.21401989,  11.9384317,  0.
 19359,  0.607790053,  11.9845982,  0.
 19360,      0.,      12.,      0.
*Element, type=C3D8R
    1,  3873,  3874,  3906,  3905,  1,  2,  34,  33
    2,  3874,  3875,  3907,  3906,  2,  3,  35,  34
    3,  3875,  3876,  3908,  3907,  3,  4,  36,  35
    ...
14878, 19325, 19326, 19358, 19357, 15453, 15454, 15486, 15485
14879, 19326, 19327, 19359, 19358, 15454, 15455, 15487, 15486
14880, 19327, 19328, 19360, 19359, 15455, 15456, 15488, 15487
**'define node sets and element sets'**
*Nset, nset=_PickedSet3, internal, generate
    1, 19360, 1
*Elset, elset=_PickedSet3, internal, generate
    1, 14880, 1
*Elset, elset=Set-1, internal, generate
    3659, 3720, 1
...
*Elset, elset=Set-edge-4, internal, generate
    11161, 11625, 1
**'define cylindrical orientation'**
*Orientation, name=Ori-1, system=CYLINDRICAL
    0.,      0.,      0.,      0.,      0.,      1.
3, 0.
**'define multiply sections associated with material definition'**
** Section: Section-1
*Solid Section, elset=Set-1, orientation=Ori-1, stack direction=1,
controls=EC-1, material=Material-1
,
...
** Section: Section-204
*Solid Section, elset=Set-edge-4, orientation=Ori-1,stack direction=1,

```

```

controls=EC-1, material=Material-e-4
,
**
*End Instance
**
*Nset, nset=_PickedSet5, internal, instance=Part-1-1
...
*Elset, elset=_PickedSet5, internal, instance=Part-1-1
...
*Nset, nset=_PickedSet6, internal, instance=Part-1-1
...
*Elset, elset=_PickedSet6, internal, instance=Part-1-1
...
*Nset, nset=_PickedSet7, internal, instance=Part-1-1
...
*Elset, elset=_PickedSet7, internal, instance=Part-1-1
...
*Nset, nset=_PickedSet37, internal, instance=Part-1-1, generate
...
*Elset, elset=_PickedSet37, internal, instance=Part-1-1, generate
...
*Elset, elset=Interst, instance=Part-1-1
...
*Elset, elset=__PickedSurf4_S2, internal, instance=Part-1-1, generate
1, 3720, 1
*Surface, type=ELEMENT, name=_PickedSurf4, internal
__PickedSurf4_S2, S2
**'define cylindrical coordinates and associate it with the model'**
*Nset, nset="_T-Part-1-1-Datum csys-1", internal
_PickedSet5,
_PickedSet6,
_PickedSet7,
*Transform, nset="_T-Part-1-1-Datum csys-1", type=C
0., 0., 0., 0., 0., 1.
*End Assembly
**
**'Assign element controls'**
** ELEMENT CONTROLS
**
*Section Controls, name=EC-1, ELEMENT DELETION=YES, hourglass=ENHANCED
1., 1., 1.
**'define material properties'**
** MATERIALS
**
*Material, name=Material-1
*User Material, constants=7
<P111>,<P112>,<P113>,<P114>,<P115>,<P116>,<P117>
...
*Material, name=Material-e-4
*User Material, constants=7
<P30411>,<P30412>,<P30413>,<P30414>,<P30415>,<P30416>,<P30417>
**
**'define BCs'**
** BOUNDARY CONDITIONS
**
** Name: BC-1 Type: Displacement/Rotation
*Boundary

```

```

_PickedSet5, 2, 2
** Name: BC-2 Type: Displacement/Rotation
*Boundary
_PickedSet6, 2, 2
_PickedSet6, 3, 3
** Name: BC-3 Type: Displacement/Rotation
*Boundary
_PickedSet7, 2, 2
_PickedSet7, 3, 3
** -----
**
** STEP: Step-1
**
*Step, name=Step-1, nlgeom=YES, inc=10000
*Static, stabilize=0.0008, allsdtol=0, continue=NO
0.1, 1., 1e-09, 1.
**
** 'define mesh controls' **
*Adaptive Mesh Controls, name=Ada-1, geometric enhancement=YES
1.0, 0.
*Adaptive Mesh, elset=_PickedSet37, controls=Ada-1, frequency=1, mesh
sweeps=10, op=NEW
**
** LOADS
**
** Name: Load-1 Type: Pressure
*Dload
_PickedSurf4, P, 16.
**
** CONTROLS
**
*Controls, reset
*Controls, parameters=time incrementation
, , , , , , 55, , ,
**
** OUTPUT REQUESTS
**
*Restart, write, frequency=0
**
** FIELD OUTPUT: F-Output-1
**
*Output, field, frequency=5
*Node Output
RF, U
*Element Output, directions=YES
EE, EVOL, LE, P, S
**
** HISTORY OUTPUT: H-Output-1
**
*Output, history, variable=PRESELECT
*End Step

```

A.ii UMAT code

```

SUBROUTINE UMAT(STRESS, STATEV, DDSDE, SSE, SPD, SCD, RPL,
1 DDSDDT, DRPLDE, DRPLDT, STRAN, DSTRAN, TIME, DTIME, TEMP, DTEMP,
2 PREDEF, DPRED, CMNAME, NDI, NSHR, NTENS, NSTATV, PROPS, NPROPS,
3 COORDS, DROT, PNEWDT, CELENT, DFGRD0, DFGRD1, NOEL, NPT, LAYER,
4 KSPT, KSTEP, KINC)
C
C   INCLUDE 'ABA_PARAM.INC'
C
C   CHARACTER*80 CMNAME
C   DIMENSION STRESS(NTENS), STATEV(NSTATV), DDSDE(NTENS, NTENS),
1   DDSDDT(NTENS), DRPLDE(NTENS), STRAN(NTENS), DSTRAN(NTENS),
2   PREDEF(1), DPRED(1), PROPS(NPROPS), COORDS(3), DROT(3, 3),
3   DFGRD0(3, 3), DFGRD1(3, 3), TIME(2)
C
C   LOCAL ARRAY
C
C   DIMENSION FR1(3), FR2(3), DISTGR(3,3), FC1(3),
1   FC2(3), F1CF1(6), F1CF1D(6), F2CF2(6), F2CF2D(6),
2   BBAR(6), BBARD(6), CBAR(6), DEL(6),
3   H(6,6), A1(6,6), A2(6,6)
C
C   PARAMETER(ZERO=0.D0, ONE=1.D0, TWO=2.D0, THREE=3.D0, FOUR=4.D0,
1   SIX=6.D0, CNINE=9.D0)
C
C -----
C   UMAT FOR HYPERELASTICITY. CANNOT BE USED FOR PLANE STRESS
C   (WITH ABAQUS PLANE STRESS OPTION). DESCRIPTION OF REQUIRED
C   INPUT PARAMETERS ARE GIVEN BELOW. FIBERS DIRECTION SHOULD
C   BE IN DEGREE (ANGLE WITH CIRCUMFERENTIAL DIRECTION).
C -----
C   PROPS(1) - EMU(c10)
C   PROPS(2) - ALPHA1(angle)
C   PROPS(3) - EMU1(k1)
C   PROPS(4) - ALPHA2(angle)
C   PROPS(5) - J-growth
C   PROPS(6) - D1 PARAMETER (SEE ABAQUS THEORY MANUAL)
C   PROPS(7) - RM (RMODELLING FACTOR)
C -----
C
C   ELASTIC MATERIAL PROPERTIES
C
C   REAL(KIND=16) EMU, ALPHA1, EMU1, F1ANG, ALPHA2, EMU2, F2ANG, JG, D1,
RM
C   EMU=DBLE(PROPS(1)*TWO)
C   ALPHA1=DBLE(PROPS(2))
C   EMU1=DBLE(PROPS(3))
C   F1ANG=DBLE(PROPS(4)*(3.14)/(180.0))
C   ALPHA2=DBLE(PROPS(2))
C   EMU2=DBLE(PROPS(3))
C   F2ANG=DBLE(PROPS(4)*(3.14)/(180.0))
C   JG=DBLE(PROPS(5))
C   D1=DBLE(PROPS(6))
C   RM=DBLE(PROPS(7))
C
C   DEFINING FIBER DIRECTION 1
C

```

```

FR1(1) = ZERO
FR1(2) = COS(F1ANG)
FR1(3) = SIN(F1ANG)
C
C   DEFINING FIBER DIRECTION 2
C
FR2(1) = ZERO
FR2(2) = COS(F2ANG)
FR2(3) = -SIN(F2ANG)
C
C   JACOBIAN AND DISTORTION TENSOR
C
DET=(ONE/JG)*(DFGRD1(1, 1)*DFGRD1(2, 2)*DFGRD1(3, 3)
1   -DFGRD1(1, 2)*DFGRD1(2, 1)*DFGRD1(3, 3))
2   +(ONE/JG)*(DFGRD1(1, 2)*DFGRD1(2, 3)*DFGRD1(3, 1)
3   +DFGRD1(1, 3)*DFGRD1(3, 2)*DFGRD1(2, 1)
4   -DFGRD1(1, 3)*DFGRD1(3, 1)*DFGRD1(2, 2)
5   -DFGRD1(2, 3)*DFGRD1(3, 2)*DFGRD1(1, 1))
SCALE=DET**(-ONE/THREE)
DO K1=1, 3
  DO K2=1, 3
    DISTGR(K2, K1)=SCALE*DFGRD1(K2, K1)
  END DO
END DO
C
C   FIBER IN CURRENT DIRRECTION (FBAR-FC1) & (FBAR-FC2)
C
FC1(1) = DISTGR(1,1)*FR1(1) + DISTGR(1,2)*FR1(2)
1   + DISTGR(1,3)*FR1(3)
FC1(2) = DISTGR(2,1)*FR1(1) + DISTGR(2,2)*FR1(2)
1   + DISTGR(2,3)*FR1(3)
FC1(3) = DISTGR(3,1)*FR1(1) + DISTGR(3,2)*FR1(2)
1   + DISTGR(3,3)*FR1(3)
C
FC2(1) = DISTGR(1,1)*FR2(1) + DISTGR(1,2)*FR2(2)
1   + DISTGR(1,3)*FR2(3)
FC2(2) = DISTGR(2,1)*FR2(1) + DISTGR(2,2)*FR2(2)
1   + DISTGR(2,3)*FR2(3)
FC2(3) = DISTGR(3,1)*FR2(1) + DISTGR(3,2)*FR2(2)
1   + DISTGR(3,3)*FR2(3)
C
C   DEFINING F1CF1 TENSOR
C
F1CF1(1) = FC1(1)**TWO
F1CF1(2) = FC1(2)**TWO
F1CF1(3) = FC1(3)**TWO
F1CF1(4) = FC1(1)*FC1(2)
F1CF1(5) = FC1(1)*FC1(3)
F1CF1(6) = FC1(2)*FC1(3)
C
C   DEFINING F1CF1D TENSOR (DEVIATORIC)
C
TF1CF1 = F1CF1(1)+F1CF1(2)+F1CF1(3)
F1CF1D(1) = F1CF1(1)-TF1CF1/THREE
F1CF1D(2) = F1CF1(2)-TF1CF1/THREE
F1CF1D(3) = F1CF1(3)-TF1CF1/THREE
F1CF1D(4) = F1CF1(4)

```

```

F1CF1D(5) = F1CF1(5)
F1CF1D(6) = F1CF1(6)
C
C   DEFINING F2CF2 TENSOR
C
F2CF2(1) = FC2(1)**TWO
F2CF2(2) = FC2(2)**TWO
F2CF2(3) = FC2(3)**TWO
F2CF2(4) = FC2(1)*FC2(2)
F2CF2(5) = FC2(1)*FC2(3)
F2CF2(6) = FC2(2)*FC2(3)
C
C   DEFINING F2CF2D TENSOR (DEVIATORIC)
C
TF2CF2 = F2CF2(1)+F2CF2(2)+F2CF2(3)
F2CF2D(1) = F2CF2(1)-TF2CF2/THREE
F2CF2D(2) = F2CF2(2)-TF2CF2/THREE
F2CF2D(3) = F2CF2(3)-TF2CF2/THREE
F2CF2D(4) = F2CF2(4)
F2CF2D(5) = F2CF2(5)
F2CF2D(6) = F2CF2(6)
C
C   CALCULATE ISO LEFT CAUCHY-GREEN DEFORMATION TENSOR
C
BBAR(1)=DISTGR(1, 1)**TWO+DISTGR(1, 2)**TWO+DISTGR(1, 3)**TWO
BBAR(2)=DISTGR(2, 1)**TWO+DISTGR(2, 2)**TWO+DISTGR(2, 3)**TWO
BBAR(3)=DISTGR(3, 3)**TWO+DISTGR(3, 1)**TWO+DISTGR(3, 2)**TWO
BBAR(4)=DISTGR(1, 1)*DISTGR(2, 1)+DISTGR(1, 2)*DISTGR(2, 2)
1      +DISTGR(1, 3)*DISTGR(2, 3)
BBAR(5)=DISTGR(1, 1)*DISTGR(3, 1)+DISTGR(1, 2)*DISTGR(3, 2)
1      +DISTGR(1, 3)*DISTGR(3, 3)
BBAR(6)=DISTGR(2, 1)*DISTGR(3, 1)+DISTGR(2, 2)*DISTGR(3, 2)
1      +DISTGR(2, 3)*DISTGR(3, 3)
C
C   DEFINING BBARD = DEV(BBAR) (DEVIATORIC)
C
TRBBAR=BBAR(1)+BBAR(2)+BBAR(3)
BBARD(1)= BBAR(1)-TRBBAR/THREE
BBARD(2)= BBAR(2)-TRBBAR/THREE
BBARD(3)= BBAR(3)-TRBBAR/THREE
BBARD(4)= BBAR(4)
BBARD(5)= BBAR(5)
BBARD(6)= BBAR(6)
C
C   CALCULATE ISO RIGHT CAUCHY-GREEN DEFORMATION TENSOR
C
CBAR(1)=DISTGR(1, 1)**TWO+DISTGR(2, 1)**TWO+DISTGR(3, 1)**TWO
CBAR(2)=DISTGR(1, 2)**TWO+DISTGR(2, 2)**TWO+DISTGR(3, 2)**TWO
CBAR(3)=DISTGR(3, 3)**TWO+DISTGR(1, 3)**TWO+DISTGR(2, 3)**TWO
CBAR(4)=DISTGR(1, 1)*DISTGR(1, 2)+DISTGR(2, 1)*DISTGR(2, 2)
1      +DISTGR(3, 1)*DISTGR(3, 2)
CBAR(5)=DISTGR(1, 1)*DISTGR(1, 3)+DISTGR(2, 1)*DISTGR(2, 3)
1      +DISTGR(3, 1)*DISTGR(3, 3)
CBAR(6)=DISTGR(1, 2)*DISTGR(1, 3)+DISTGR(2, 2)*DISTGR(2, 3)
1      +DISTGR(3, 2)*DISTGR(3, 3)
C
C   INVARIANT I4

```

```

C
  CI4 = (FR1(1)*(CBAR(1)*FR1(1)+CBAR(4)*FR1(2)+CBAR(5)*FR1(3))
1      +FR1(2)*(CBAR(4)*FR1(1)+CBAR(2)*FR1(2)+CBAR(6)*FR1(3))
2
+FR1(3)*(CBAR(5)*FR1(1)+CBAR(6)*FR1(2)+CBAR(3)*FR1(3)))/(RM**TWO)
C
C   FIBER CANNOT GO IN COMPRESSION
  IF(CI4 .LT. ONE) CI4=ONE
C
C   INVARIANT I6
C
  CI6 = (FR2(1)*(CBAR(1)*FR2(1)+CBAR(4)*FR2(2)+CBAR(5)*FR2(3))
1      +FR2(2)*(CBAR(4)*FR2(1)+CBAR(2)*FR2(2)+CBAR(6)*FR2(3))
2
+FR2(3)*(CBAR(5)*FR2(1)+CBAR(6)*FR2(2)+CBAR(3)*FR2(3)))/(RM**TWO)
C
C   FIBER CANNOT GO IN COMPRESSION
  IF(CI6 .LT. ONE) CI6=ONE
C
C   CALCULATE THE STRESS
C
C   NEOHOOKEAN BASE MATRIX MODEL
  W1J = EMU/(TWO*DET)
  W11J = ZERO
C
  W4J=EMU1*(CI4-ONE)*EXP(ALPHA1*(CI4-ONE)**TWO)/DET
W44J=EMU1*EXP(ALPHA1*(CI4-ONE)**TWO)*(TWO*ALPHA1*(CI4-ONE)**TWO+ONE)/DET
W6J=EMU2*(CI6-ONE)*EXP(ALPHA2*(CI6-ONE)**TWO)/DET
W66J=EMU2*EXP(ALPHA2*(CI6-ONE)**TWO)*(TWO*ALPHA2*(CI6-ONE)**TWO+ONE)/DET
  EK=TWO/D1*(TWO*DET-ONE)
  PR=TWO*(DET-ONE)/D1
  DO K1=1,NDI
    STRESS(K1)=TWO*(W1J*BBARD(K1)+W4J*F1CF1D(K1)
1      +W6J*F2CF2D(K1))+PR
  END DO
  DO K1=NDI+1,NDI+NSHR
    STRESS(K1)=TWO*(W1J*BBARD(K1)+W4J*F1CF1D(K1)
1      +W6J*F2CF2D(K1))
  END DO
C
C   DEFINING A UNIT TENSOR DEL
C
  DEL(1) = ONE
  DEL(2) = ONE
  DEL(3) = ONE
  DEL(4) = ZERO
  DEL(5) = ZERO
  DEL(6) = ZERO
C
C   CALCULATION OF FORTH ORDER H TENSOR
C
  DO K1 = 1,3
    DO K2 = 1,3
      DO K3 = 1,3
        DO K4 = 1,3

```

```

IF (K1 .EQ. K2) THEN
  K5 = K1
ELSE
  K5 = K1+K2+1
END IF
IF (K3 .EQ. K4) THEN
  K6 = K3
ELSE
  K6 = K3+K4+1
END IF
IF (K1 .EQ. K3) THEN
  K7 = K1
ELSE
  K7 = K1+K3+1
END IF
IF (K2 .EQ. K4) THEN
  K8 = K2
ELSE
  K8 = K2+K4+1
END IF
IF (K1 .EQ. K4) THEN
  K9 = K1
ELSE
  K9 = K1+K4+1
END IF
IF (K2 .EQ. K3) THEN
  K10 = K2
ELSE
  K10 = K2+K3+1
END IF

```

C

```

1          H(K5,K6) = (DEL(K7)*BBAR(K8)+DEL(K8)*BBAR(K7)
                +DEL(K9)*BBAR(K10)+DEL(K10)*BBAR(K9))/TWO
          END DO
        END DO
      END DO
    END DO

```

C

C

CALCULATION OF FORTH ORDER A1 TENSOR FIBER SET ONE

C

```

DO K1 = 1,3
  DO K2 = 1,3
    DO K3 = 1,3
      DO K4 = 1,3
        IF (K1 .EQ. K2) THEN
          K5 = K1
        ELSE
          K5 = K1+K2+1
        END IF
        IF (K3 .EQ. K4) THEN
          K6 = K3
        ELSE
          K6 = K3+K4+1
        END IF
        IF (K1 .EQ. K3) THEN
          K7 = K1
        ELSE

```

```

        K7 = K1+K3+1
    END IF
    IF (K2 .EQ. K4) THEN
        K8 = K2
    ELSE
        K8 = K2+K4+1
    END IF
    IF (K1 .EQ. K4) THEN
        K9 = K1
    ELSE
        K9 = K1+K4+1
    END IF
    IF (K2 .EQ. K3) THEN
        K10 = K2
    ELSE
        K10 = K2+K3+1
    END IF
C
        A1(K5,K6) = (DEL(K7)*F1CF1(K8)+DEL(K8)*F1CF1(K7)
1          +DEL(K9)*F1CF1(K10)+DEL(K10)*F1CF1(K9))/TWO
    END DO
    END DO
    END DO
    END DO
C
C    CALCULATION OF FORTH ORDER A2 TENSOR FIBER SET TWO
C
    DO K1 = 1,3
    DO K2 = 1,3
    DO K3 = 1,3
    DO K4 = 1,3
        IF (K1 .EQ. K2) THEN
            K5 = K1
        ELSE
            K5 = K1+K2+1
        END IF
        IF (K3 .EQ. K4) THEN
            K6 = K3
        ELSE
            K6 = K3+K4+1
        END IF
        IF (K1 .EQ. K3) THEN
            K7 = K1
        ELSE
            K7 = K1+K3+1
        END IF
        IF (K2 .EQ. K4) THEN
            K8 = K2
        ELSE
            K8 = K2+K4+1
        END IF
        IF (K1 .EQ. K4) THEN
            K9 = K1
        ELSE
            K9 = K1+K4+1
        END IF
        IF (K2 .EQ. K3) THEN

```

```

        K10 = K2
    ELSE
        K10 = K2+K3+1
    END IF
C
        A2(K5,K6) = (DEL(K7)*F2CF2(K8)+DEL(K8)*F2CF2(K7)
1          +DEL(K9)*F2CF2(K10)+DEL(K10)*F2CF2(K9))/TWO
        END DO
    END DO
END DO
END DO
C
C  CALCULATE THE STIFFNESS
C
C  CALCULATION OF FORTH ORDER DDSDE TENSOR
C
DO K1 = 1,3
DO K2 = 1,3
DO K3 = 1,3
DO K4 = 1,3
IF (K1 .EQ. K2) THEN
K5 = K1
ELSE
K5 = K1+K2+1
END IF
IF (K3 .EQ. K4) THEN
K6 = K3
ELSE
K6 = K3+K4+1
END IF
C
IF (K5 .LT. 4 .AND. K6 .LT. 4) THEN
1      DDSDE(K5,K6) = FOUR*W11J*BBARD(K5)*BBARD(K6)+
2      FOUR*W44J*F1CF1D(K5)*F1CF1D(K6)+
3      FOUR*W66J*F2CF2D(K5)*F2CF2D(K6)+
4      TWO*W1J*(H(K5,K6)-TWO*(DEL(K5)*BBAR(K6)+
5      BBAR(K5)*DEL(K6))/THREE+
6      TWO*TRBBAR*DEL(K5)*DEL(K6)/CNINE)+
7      TWO*W4J*(A1(K5,K6)-TWO*(DEL(K5)*F1CF1(K6)+
8      F1CF1(K5)*DEL(K6))/THREE+
9      TWO*CI4*DEL(K5)*DEL(K6)/CNINE)+
1     TWO*W6J*(A2(K5,K6)-TWO*(DEL(K5)*F2CF2(K6)+
2     F2CF2(K5)*DEL(K6))/THREE+
3     TWO*CI6*DEL(K5)*DEL(K6)/CNINE)+EK
ELSE
1     DDSDE(K5,K6) = FOUR*W11J*BBARD(K5)*BBARD(K6)+
2     FOUR*W44J*F1CF1D(K5)*F1CF1D(K6)+
3     FOUR*W66J*F2CF2D(K5)*F2CF2D(K6)+
4     TWO*W1J*(H(K5,K6)-TWO*(DEL(K5)*BBAR(K6)+
5     BBAR(K5)*DEL(K6))/THREE+
6     TWO*TRBBAR*DEL(K5)*DEL(K6)/CNINE)+
7     TWO*W4J*(A1(K5,K6)-TWO*(DEL(K5)*F1CF1(K6)+
8     F1CF1(K5)*DEL(K6))/THREE+
9     TWO*W6J*(A2(K5,K6)-TWO*(DEL(K5)*F2CF2(K6)+
1    F2CF2(K5)*DEL(K6))/THREE+
2    TWO*CI6*DEL(K5)*DEL(K6)/CNINE)

```

```
                END IF
            END DO
        END DO
    END DO
C
C    WRITE(*,*) 'zo', CI4
RETURN
END
```

A.iii PYTHON code

```

import math
import numpy as np
#'read in parameters'#
Me0,Mc0,M0,k1,k2,c1,theta,r0,Th,rff,D1,kdc=np.loadtxt('Parabase.py')
t='current time step'
wuc=(Th-70)/365.0
kqc=math.log10(2)/Th*365
rgbase=Mc0*(1-math.exp(-kqc))

lch1,lch2,lch3,...,lch202,lch203,lch204=np.loadtxt('lch.inp')
LCr=[lch1,lch2,lch3,...,lch202,lch203,lch204]
mcp1,mcp2,mcp3,...,mcp202,mcp203,mcp204=np.loadtxt('Y10mass-c.inp')
mcp=[mcp1,mcp2,mcp3,...,mcp202,mcp203,mcp204]
rmt1,rmt2,rmt3,...,rmt202,rmt203,rmt204=np.loadtxt('rt10.inp')
rrtp=[rmt1,rmt2,rmt3,...,rmt202,rmt203,rmt204]

#'define variables'#
Met = np.zeros(204)
JG = np.zeros(204)
ccl = np.zeros(204)
Mct =np.zeros(204)
kk1=np.zeros(204)
rrt=np.zeros(204)
LLE = np.zeros((204,6))
LC = np.zeros(204)
LCt = np.zeros(204)
LCtt=np.zeros(204)
dlt=np.zeros(204)
kkt=np.zeros(204)
qt=np.zeros(204)
mgc=np.zeros(204)
Mctt = np.zeros(204)
rrrt = np.zeros(204)
mep=np.zeros(204)
mtotalt=np.zeros(204)
mtotalp=np.zeros(204)

from odbAccess import *
#'read in ABAQUS odb values (deformation tensor)'#
odb = openOdb('./Previous time step'.odb')
lastFrame = odb.steps['Step-1'].frames[-1]
strain = lastFrame.fieldOutputs['EE']
stress = lastFrame.fieldOutputs['S']
Interst = odb.rootAssembly.elementSets['INTERST']
setstrain = strain.getSubset(region=Interst,position=CENTROID)
for el in range(0,204):
    for nd in range(0,6):
        LLE[el,nd]=setstrain.values[el].data[nd]
    LC[el]=((2*LLE[el,1]+1)*cos(theta/180*3.14)**2\
            +4*(LLE[el,5])*cos(theta/180*3.14)*sin(theta/180*3.14)\
            +(2*LLE[el,2]+1)*sin(theta/180*3.14)**2)**0.5
    LCt[el]=LC[el]/rrtp[el]
    if LCt[el]<1:
        LCt[el]=1.0
    dlt[el]=LCt[el]-LCr[el]
    if dlt[el]<0:
        dlt[el]=0.0

```

```

    mea=0.1
# 'define current elastin mass value' #
for nnel in range(0,51):
    Met[nnel]=Me0*(mea*((50.0-nnel)/50.0)**2+1-mea)**t
    Met[nnel+51]=Met[nnel]
    Met[nnel+102]=Met[nnel]
    Met[nnel+153]=Met[nnel]
for eel in range(0,204):
    kkt[eel]=kqc+kqc*wuc*(dlt[eel]/LCr[eel])**2
    qt[eel]=exp(-kkt[eel])
    mgc[eel]=rgbase*(kdc*dlt[eel]/LCr[eel]+1)
    mep[eel]=Met[eel]/0.9
    Mctt[eel]=mcp[eel]*qt[eel]+mgc[eel]
    mtotalt[eel]=(Met[eel]+Mctt[eel])
    mtotalp[eel]=(mcp[eel]+mep[eel])
    rrrt[eel]=rrtp[eel]+rff/365*dlt[eel]/LCr[eel]
for jgel in range(0,204):
    JG[jgel]=mtotalt[jgel]/mtotalp[jgel]
# 'define current collagen mass value' #
for nel in range(0,51):
    Mct[nel+153]=max(Mctt[nel],Mctt[nel+51],Mctt[nel+102],Mctt[nel+153])
    Mct[nel]=min(Mctt[nel],Mctt[nel+51],Mctt[nel+102],Mctt[nel+153])
    Mct[nel+51]=Mct[nel]+(Mct[nel+153]-Mct[nel])/3.0
    Mct[nel+102]=Mct[nel]+(Mct[nel+153]-Mct[nel])/3.0*2.0

    rrt[nel]=min(rrrt[nel],rrrt[nel+51],rrrt[nel+102],rrrt[nel+153])
    rrt[nel+153]=max(rrrt[nel],rrrt[nel+51],rrrt[nel+102],rrrt[nel+153])
    rrt[nel+51]=rrt[nel]+(rrt[nel+153]-rrt[nel])/3.0
    rrt[nel+102]=rrt[nel]+(rrt[nel+153]-rrt[nel])/3.0*2.0
for eeel in range(0,204):
    ccl[eeel]=Met[eeel]*c1/JG[eeel]
    kkl[eeel]=Mct[eeel]*k1/JG[eeel]

# 'define current SEF umat values' #
tt=open('.'current time step'para.inp','w')
tt.write('*Heading')
tt.write("\n")
tt.write('*Preprint, echo=NO, model=NO, history=NO, contact=NO')
tt.write("\n")
tt.write('*Parameter')
tt.write("\n")
tt.write('P111='+repr(ccl[50])+'\n'+ 'P112='+repr(k2)+'\n'+ 'P113='+repr(k
k1[50])+'\n'+ 'P114='+repr(theta)+'\n'+ 'P115='+format((JG[50]),'.5e')+'\n
'+ 'P116='+repr(D1)+'\n'+ 'P117='+repr(rrt[50]))
tt.write("\n")
...
tt.write('P30411='+repr(ccl[153])+'\n'+ 'P30412='+repr(k2)+'\n'+ 'P30413='
+repr(kkl[153])+'\n'+ 'P30414='+repr(theta)+'\n'+ 'P30415='+format((JG[153
]),'.5e')+'\n'+ 'P30416='+repr(D1)+'\n'+ 'P30417='+repr(rrt[153]))
tt.write("\n")
tt.close()
# 'write current collagen mass values' #
mm=open('.'current time step'mass-c.inp','w')
mm.write(repr(Mct[0])+'\n'+repr(Mct[1])+'\n'+repr(Mct[2])+'\n'+repr(Mct[
3])+'\n'+repr(Mct[4])+'\n'+repr(Mct[5])+'\n'+repr(Mct[6])+'\n'+repr(Mct[
7])+'\n'+repr(Mct[8])+'\n')
...

```

```
mm.write(repr(Mct[200])+"\n"+repr(Mct[201])+"\n"+repr(Mct[202])+"\n"+repr(Mct[203]))
mm.close()
#'write current collagen recruitment values'#
ll=open('.'current collagen r values'.inp','w')
ll.write(repr(rrt[0])+"\n"+repr(rrt[1])+"\n"+repr(rrt[2])+"\n"+repr(rrt[3])+"\n"+repr(rrt[4])+"\n"+repr(rrt[5])+"\n"+repr(rrt[6])+"\n"+repr(rrt[7])+"\n"+repr(rrt[8])+"\n")
...
ll.write(repr(rrt[200])+"\n"+repr(rrt[201])+"\n"+repr(rrt[202])+"\n"+repr(rrt[203]))
ll.close()
```

B Appendix B

Growth and remodeling with application to abdominal aortic aneurysms

Reference

Wenjian Lin, Mark D. Iafrazi, Robert A. Peattie, Luis Dorfmann

Growth and remodeling with application to abdominal aortic aneurysms

W. J. Lin · M. D. Iafrati · R. A. Peattie ·
L. Dorfmann 

Received: 12 March 2017 / Accepted: 29 May 2017 / Published online: 13 June 2017
© Springer Science+Business Media Dordrecht 2017

Abstract In this paper, we apply a mixture theory of growth and remodeling to study the formation and dilatation of abdominal aortic aneurysms. We adapt the continuum theory of mixtures to formalize the processes of production and removal of constituents from a loaded body. Specifically, we consider a mixture of elastin and collagen fibers which endow the material with anisotropic properties. An evolving recruitment variable defines the intermediate configuration from which the elastic stretch of collagen is measured. General formulations of the equations governing homeostatic state and aneurysm development are provided. In the homeostatic state, the idealized geometry of the aorta is a thick-walled tube subject to constant internal pressure and axial stretch. The formation of an aneurysm induces an increase of mass locally achieved via production of new material that exceeds the removal of old material. The combined effects of loss of elastin, degradation of existing and deposition of new collagen, as well as fiber remodeling results in a continuous enlargement of the aneurysm bulge. The numerical method makes use of a purposely written material subroutine, called UMAT, which is based on the constitutive formulation provided in the paper. Numerical results based on patient-based material parameters are illustrated.

Keywords AAA · Abdominal aortic aneurysm · Finite element analysis · Growth · Homeostatic state · Mixture theory · Remodeling

1 Introduction

Abdominal aortic aneurysm (AAA) is a permanent, degenerative, and local expansion of the abdominal aortic wall that is potentially life-threatening if it progresses to rupture. Despite a long history of research into the causes and the mechanical behavior of AAAs, systems capable of predicting risk of rupture on a patient-specific basis with sufficient accuracy for clinical use have not yet been developed. Therefore, there remains a major incentive to

W. J. Lin · L. Dorfmann (✉)
Department of Civil Engineering, Tufts University Medford, Medford, MA 02155, USA
e-mail: luis.dorfmann@tufts.edu

M. D. Iafrati · R. A. Peattie
Department of Surgery, Tufts Medical Center, Boston, MA 02111, USA

L. Dorfmann
Department of Biomedical Engineering, Tufts University, Medford, MA 02155, USA

improve the accuracy of biomechanical models that can guide clinical management decisions. Our contribution, in this paper, is to present a three-dimensional theory to simulate, beginning from the homeostatic state, the formation and adaptation of an abdominal aortic aneurysm. By means of a mixture theory of growth and remodeling, we predict the development of inhomogeneous mechanical properties and an axisymmetric dilatation of the diseased aortic wall.

The principal load-bearing elements of the aorta wall are collagen and elastin. In the healthy aorta, at low strain levels, collagen fibers carry only a small share of the wall loading due to the inherent waviness of collagen fibrils [1–3]. Moreover, unloaded tissue shows a distribution of fibrils of varying wavelengths. Physiologic pressures expand the wall to strain levels at which collagen fibrils straighten and begin to carry load [4,5]. Increases in loading or strain beyond rest-state levels then result in the straightening of increasing numbers of fibrils. The consequent recruitment of progressively greater numbers of fibrils into the load-bearing process leads to the well-known exponential stiffening of wall tissue samples under load [6–8].

Within the native aorta wall *in vivo*, collagen fibers are thought to be in a continuous state of resorption and new deposition. Turnover rates can vary from 3–90 days under healthy conditions [9]. In particular, the half-life of collagen fibers in rat aorta and mesenteric arteries has been found to be 60–70 days in normal animals, but only 17 days in the context of hypertension [10]. A general agreement has emerged that total elastin content in the AAA wall is significantly reduced compared with healthy tissue [11,12]. In contrast, changes to collagen mass are not yet clear. Increased collagen and ground matrix volumes are reported by He and Roach [11]; other authors have suggested total deposited collagen mass remains unchanged [13] or decreases [14,15].

Two- and three-dimensional constitutive laws of isotropic and anisotropic material behaviors have been developed and used to estimate the mechanical response of AAAs. Note that wall stress calculations to date have primarily assumed the wall to be characterized by homogeneous mechanical properties [8,16–22]. Inhomogeneous properties, different in media and adventitia, were used in [23]. These numerical results, combined with patient data, are used as biomechanical rupture risk parameters [16,18,24–27].

The interaction between mechanical stretch and collagen microstructure is quantified in [28,29]. The resulting mathematical theory was used to illustrate the effect of collagen remodeling on the dilatation of an abdominal aortic aneurysm. The formulation introduces recruitment variables to characterize the changes in the microstructure of the arterial wall, which lead to the formation of aneurysms. Homogenization and mixture theories are combined to capture growth and remodeling of soft tissues induced by altered stimuli [30]. This approach has been used to evaluate evolving, thin-walled, intracranial fusiform aneurysms with special attention to the production, removal, and alignment of collagen [31]. The theory is further developed to capture pressure- and flow-induced changes in geometry, structure, and mechanical behavior in diverse arteries [32,33]. A parametric study to evaluate the effects of collagen turnover and loss of functional elastin on the formation of abdominal aortic aneurysm is reported in [34]. These works demonstrate that evolving material properties play a fundamental role in the formation and in the spatio-temporal changes of AAAs, in particular on radial dilatation, axial expansion, wall thickness, fiber stretch, and maximum wall stress. The finite element method is used to model the evolving geometry, vasoactive capacity and arterial dilatation of a multilayered, human abdominal aorta [35,36].

The present paper is organized as follows. Section 2 summarizes relevant equations of continuum mechanics and specializes the theory applicable to materials endowed with a structure. In Sect. 3, we adapt the continuum theory of mixtures to formalize the processes of production and removal of constituents from a loaded body. The deposition of new and the remodeling of embedded fibers is illustrated for a mixture of elastin and collagen. Growth is defined in Sect. 4 as an increase in mass locally, achieved via production of new material that exceeds the removal of old material. In Sect. 5, we write the total stored energy as the sum of isochoric and dilatational parts, measured per unit reference mass. The governing equations of the homeostatic state and of aneurysm development are derived in Sect. 6. Functions of the volumetric energy, of the isotropic matrix, and of the embedded collagen fibers are specialized to account for local degradation, new material production, and fiber remodeling. Section 7 describes the computation model, lists the material parameters, and reports numerical results. Section 8 contains concluding remarks.

2 Basic equations of continuum mechanics

2.1 Kinematics of continua

The region \mathcal{B}_r occupied by an unloaded body is typically chosen as the reference configuration from which the deformation is measured. The location of a material particle in \mathcal{B}_r is identified by its position vector \mathbf{X} relative to some fixed origin. Let \mathcal{B} denote the configuration of the body after deformation from \mathcal{B}_r , with \mathbf{x} denoting the position vector occupied by the material particle which was at \mathbf{X} in \mathcal{B}_r . The deformation is described in terms of the vector function χ through $\mathbf{x} = \chi(\mathbf{X})$, $\mathbf{X} \in \mathcal{B}_r$, and it is assumed that χ has sufficient regularity for the ensuing analysis.

The deformation gradient tensor \mathbf{F} relative to the configuration \mathcal{B}_r is defined by

$$\mathbf{F} = \text{Grad } \chi(\mathbf{X}) = \text{Grad } \mathbf{x}, \quad (2.1)$$

where Grad is the gradient operator with respect to \mathbf{X} . The deformation gradient has Cartesian components $F_{i\alpha} = \partial x_i / \partial X_\alpha$, where $i, \alpha \in \{1, 2, 3\}$. Roman indices are associated with the current configuration \mathcal{B} and Greek indices with the reference configuration \mathcal{B}_r . We also use the standard notation J to denote the determinant of \mathbf{F}

$$J = \det \mathbf{F}. \quad (2.2)$$

Note that J , which by the condition of geometric compatibility of the displacement field, is positive and relates an infinitesimal volume element dv in \mathcal{B} to its counterpart dV in \mathcal{B}_r via

$$dv = J dV. \quad (2.3)$$

Associated with \mathbf{F} are the right and left Cauchy–Green deformation tensors defined, respectively, by

$$\mathbf{C} = \mathbf{F}^T \mathbf{F}, \quad \mathbf{B} = \mathbf{F} \mathbf{F}^T, \quad (2.4)$$

where the superscript T indicates the transpose of a second-order tensor. Of particular interest are the principal invariants of \mathbf{C} given by

$$I_1 = \text{tr} \mathbf{C}, \quad I_2 = \frac{1}{2}[I_1^2 - \text{tr}(\mathbf{C}^2)], \quad I_3 = \det \mathbf{C} \equiv J^2. \quad (2.5)$$

Suppose that in its reference configuration the material is endowed with a structure that is identified by the presence of preferred directions corresponding to unit vectors $\mathbf{M}(\mathbf{X})$ and $\mathbf{M}'(\mathbf{X})$, typically associated with the mean orientation of two families of collagen fibers. From these preferred directions are defined the *structure tensors* $\mathbf{M} \otimes \mathbf{M}$ and $\mathbf{M}' \otimes \mathbf{M}'$. Following [37,38], we note that the integrity basis for three symmetric second-order tensors in three dimensions includes the invariants (2.5), the invariants that depend on $\mathbf{M} \otimes \mathbf{M}$ and $\mathbf{M}' \otimes \mathbf{M}'$ and additionally a coupling invariant that involves both fiber directions. We focus attention here on the invariants that depend on \mathbf{M} and \mathbf{M}' , typically denoted I_4, I_5, I_6, I_7 and defined by

$$I_4 = \mathbf{M} \cdot (\mathbf{C}\mathbf{M}), \quad I_5 = \mathbf{M} \cdot (\mathbf{C}^2\mathbf{M}), \quad I_6 = \mathbf{M}' \cdot (\mathbf{C}\mathbf{M}'), \quad I_7 = \mathbf{M}' \cdot (\mathbf{C}^2\mathbf{M}'). \quad (2.6)$$

2.2 Hyperelasticity

The theory of hyperelasticity describes the elastic response of a material by means of a strain-energy function, defined per unit reference volume, which we denote by W . For an isotropic and homogeneous material, W depends only on the deformation gradient \mathbf{F} , and, by objectivity, it depends on \mathbf{F} through \mathbf{C} , and we write $W = W(\mathbf{C})$. For

an anisotropic elastic solid with two preferred directions, W depends on \mathbf{C} and on the structure tensors $\mathbf{M} \otimes \mathbf{M}$, $\mathbf{M}' \otimes \mathbf{M}'$, and we express this dependence by writing

$$W = W(\mathbf{C}, \mathbf{M} \otimes \mathbf{M}, \mathbf{M}' \otimes \mathbf{M}'). \quad (2.7)$$

The nominal and Cauchy stress tensors, denoted \mathbf{P} and $\boldsymbol{\sigma}$, respectively, are given by the standard formulas:

$$\mathbf{P} = \frac{\partial W}{\partial \mathbf{F}}, \quad \boldsymbol{\sigma} = J^{-1} \mathbf{F} \frac{\partial W}{\partial \mathbf{F}}, \quad (2.8)$$

with $\boldsymbol{\sigma}$ being symmetric. In Cartesian components,

$$P_{\alpha i} = \frac{\partial W}{\partial F_{i\alpha}}, \quad \sigma_{ij} = \sigma_{ji} = J^{-1} F_{i\alpha} \frac{\partial W}{\partial F_{j\alpha}}, \quad (2.9)$$

the first of which identifies the convention used here for the order of the indices in the differentiation with respect to a nonsymmetric second-order tensor. Here and henceforth, the summation convention for repeated indices is used. In the absence of body forces, the equilibrium equation can be written alternatively in terms of the nominal stress or Cauchy stress as

$$\text{Div } \mathbf{P} = \mathbf{0}, \quad \text{div } \boldsymbol{\sigma} = \mathbf{0}, \quad (2.10)$$

where Div and div are the divergence operators with respect to \mathbf{X} and \mathbf{x} , respectively.

The response of biological tissue to short-term transient loads is, in general, assumed incompressible. On the other hand, the behavior during growth and remodeling is characterized by a change in volume and hence $J \neq 1$. It is then convenient to separate the dependence of W on \mathbf{F} into dilatational and volume-preserving contributions, and for this purpose, following [39,40], we introduce the multiplicative decomposition:

$$\mathbf{F} = J^{1/3} \bar{\mathbf{F}}, \quad (2.11)$$

where $\bar{\mathbf{F}}$ is the isochoric contribution to the deformation, satisfying $\det \bar{\mathbf{F}} = 1$, and J describes the volume change. It follows that the isochoric right and left Cauchy–Green tensors are, respectively, given by

$$\bar{\mathbf{C}} = \bar{\mathbf{F}}^T \bar{\mathbf{F}}, \quad \bar{\mathbf{B}} = \bar{\mathbf{F}} \bar{\mathbf{F}}^T. \quad (2.12)$$

To account for the decomposition in the material properties, we separate the dependence on \mathbf{C} into dependence on $\bar{\mathbf{C}}$ and J , and define the modified strain-energy function \bar{W} by

$$\bar{W}(\bar{\mathbf{C}}, J, \mathbf{M} \otimes \mathbf{M}, \mathbf{M}' \otimes \mathbf{M}') = W(\mathbf{C}, \mathbf{M} \otimes \mathbf{M}, \mathbf{M}' \otimes \mathbf{M}'). \quad (2.13)$$

Following a common practice in computational mechanics, we decouple the energy function into the sum of a part that depends on $\bar{\mathbf{C}}$ and a part that depends on J . Here, we express this in the following form:

$$\bar{W} = \bar{W}_{\text{iso}}(\bar{\mathbf{C}}, \mathbf{M} \otimes \mathbf{M}, \mathbf{M}' \otimes \mathbf{M}') + \bar{W}_{\text{vol}}(J), \quad (2.14)$$

where \bar{W}_{iso} and \bar{W}_{vol} denote the volume-preserving (isochoric) and volumetric (dilatational) contributions.

For the considered structure, the strain energy must be an isotropic function of the three tensors \mathbf{C} , $\mathbf{M} \otimes \mathbf{M}$, $\mathbf{M}' \otimes \mathbf{M}'$, and W is then reduced to dependence on the invariants of the tensors listed in (2.5) and (2.6). Equivalently, it can be regarded as being dependent on the isochoric invariants together with J . We distinguish the isochoric invariants with an overbar. Thus, by replacing \mathbf{C} by $\bar{\mathbf{C}}$ in the definitions of the invariants involving \mathbf{C} , we obtain $\bar{I}_3 = 1$ and

$$\bar{I}_i = \begin{cases} J^{-2/3} I_i, & i = 1, 4, 6, \\ J^{-4/3} I_i, & i = 2, 5, 7. \end{cases} \tag{2.15}$$

For an illustration that includes dependence on both preferred directions, we consider an energy function that depends only on the invariants \bar{I}_1, \bar{I}_4 and \bar{I}_6 along with J

$$\bar{W} = \bar{W}_{\text{iso}}(\bar{I}_1, \bar{I}_4, \bar{I}_6) + \bar{W}_{\text{vol}}(J). \tag{2.16}$$

We are then able to decompose the Cauchy stress into the sum of an isochoric part, denoted $\bar{\sigma}$, and a volumetric part, denoted σ_{vol} , so that $\sigma = \bar{\sigma} + \sigma_{\text{vol}}$. The isochoric part may be written in the form:

$$\bar{\sigma} = 2J^{-1} [\bar{W}_1 \text{dev } \bar{\mathbf{B}} + \bar{W}_4 \text{dev}(\bar{\mathbf{m}} \otimes \bar{\mathbf{m}}) + \bar{W}_6 \text{dev}(\bar{\mathbf{m}}' \otimes \bar{\mathbf{m}}')], \tag{2.17}$$

where $\bar{W}_i = \partial \bar{W} / \partial \bar{I}_i, i = 1, 4, 6$ and $\bar{\mathbf{m}} = \bar{\mathbf{F}}\mathbf{M}$, and $\bar{\mathbf{m}}' = \bar{\mathbf{F}}\mathbf{M}'$ are the push forward versions of \mathbf{M} and \mathbf{M}' , respectively. The operator dev indicates the deviatoric part of a second-order tensor and is defined by

$$\text{dev}(\cdot) = (\cdot) - \frac{1}{3} \text{tr}(\cdot) \mathbf{I}, \tag{2.18}$$

where \mathbf{I} is the identity tensor. The volumetric part of the Cauchy stress has the form:

$$\sigma_{\text{vol}} = \bar{W}_J \mathbf{I}, \tag{2.19}$$

where $\bar{W}_J = \partial \bar{W} / \partial J$.

3 Biological growth and remodeling

In this section, we adapt the continuum theory of mixtures to formalize the processes of production and removal of constituents from a loaded body [41, 42]. In what follows, we focus attention to the main solid constituents of an arterial wall and neglect contributions of fluid content and all solid-fluid interactions [30]. Specifically, we consider a mixture of an isotropic elastin matrix, and embedded collagen fibers. These constituents are characterized by rates of production and removal and by constitutive equations with evolving natural configurations. The mechanical contributions of smooth muscle cells, following [28, 43], are ignored.

It is customary to identify the reference location of the constituent i by its position vector \mathbf{X}^i . The location of each constituent i at time t is determined by the vector function χ^i through

$$\mathbf{x} = \chi^i(\mathbf{X}^i, t), \tag{3.1}$$

which shows that the theory of mixtures considers each location \mathbf{x} as occupied simultaneously by all constituents i . Equation (3.1) further implies that each constituent i of the mixture undergoes an affine deformation, i.e. each constituent experience the same deformation as the mixture. This constraint is obviously an idealization of the real material behavior, but provides a good approximation of the actual material response. Mixtures subject to this constraint are referred to as *constrained mixtures* [30]. By the concepts of constrained mixture and evolving natural configurations of constituent i , produced at time τ , it follows that

$$\mathbf{F}^i(t, \tau) = \frac{\partial \mathbf{x}^i(t)}{\partial \mathbf{X}^i(\tau)} = \frac{\partial \mathbf{x}(t)}{\partial \mathbf{X}^i(\tau)}. \tag{3.2}$$

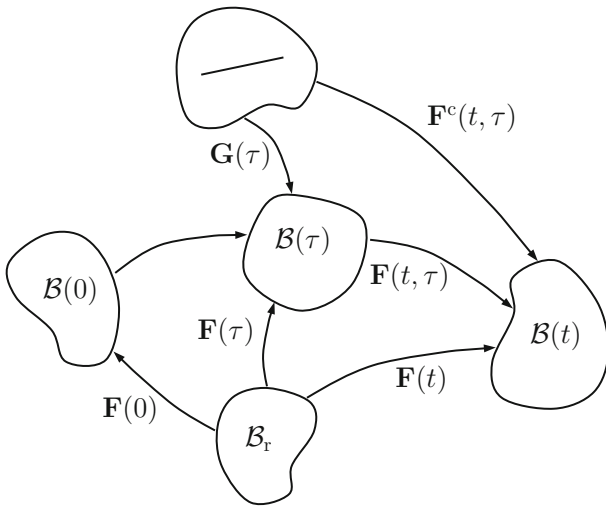


Fig. 1 $\mathcal{B}(0)$, $\mathcal{B}(\tau)$ and $\mathcal{B}(t)$ define the configurations of the mixture at times 0, τ and t , respectively. The corresponding deformations, with respect to the reference configuration \mathcal{B}_r , are quantified by $\mathbf{F}(0)$, $\mathbf{F}(\tau)$ and $\mathbf{F}(t)$. The deformation of a collagen fiber $\mathbf{G}(\tau)$, deposited into the mixture at time τ , is measured from its natural configuration. The total deformation of the fiber at time t , which was generated at time τ , is given by $\mathbf{F}^c(t, \tau)$

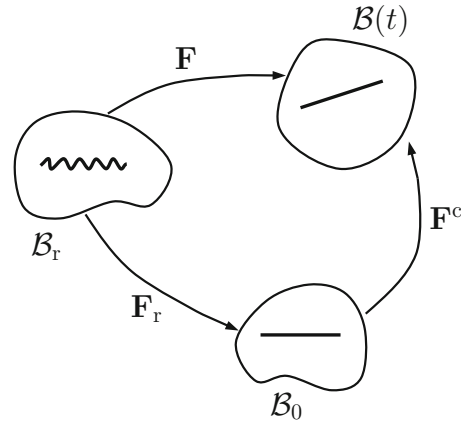


Fig. 2 Reference, intermediate and current configurations of the mixture. The unloaded state \mathcal{B}_r contains a distribution of fibrils of varying wavelengths. Physiologic loads deform the mixture from \mathcal{B}_r to $\mathcal{B}(t)$ and stretch collagen fibers. Fibers begin to carry load in the intermediate configuration \mathcal{B}_0

In biological tissue mechanical stress modulates a continuous turnover of its constituents [44]. In particular, turnover of collagen is much faster compared to elastin [9]. Therefore, attention is first focused on the formation of new collagen fibers and on the deposition into the mixture and then, in the next section, on fiber remodeling [45].

3.1 Fiber deposition

The kinematics of deposition of newly produced fibers is developed in [30,31,46,47]. Following the notation introduced in [48], we use the time variable t to identify individual loaded configurations, denoted $\mathcal{B}(t)$, which are elements in the set of all admissible configurations of the mixture. The time interval $-\infty < t < 0$ represents the homeostatic state of the arterial wall, with growth and remodeling activated at $t = 0$. Hence, $\mathcal{B}(0)$ denotes the loaded configuration at $t = 0$, into which the body is deformed relative to the reference \mathcal{B}_r with corresponding deformation gradient $\mathbf{F}(0)$, see Fig. 1. Suppose that at a specified time τ , with $0 \leq \tau \leq t$, a newly produced collagen fiber is stretched relative to its natural (stress-free) configuration and then deposited into the mixture occupying the configuration $\mathcal{B}(\tau)$. The deformation gradient associated with the deposition is given by the tensor $\mathbf{G}(\tau)$ [31]. Following deposition, we assume that the mixture with the newly embedded fiber undergoes an affine deformation (the fiber network deforms with the macroscopic deformation) to the current configuration $\mathcal{B}(t)$ characterized by the deformation gradient $\mathbf{F}(t, \tau)$. Therefore, the mixture at current time t can be thought of as reached in two steps with the deformation gradient decomposed according to

$$\mathbf{F}(t) = \mathbf{F}(t, \tau)\mathbf{F}(\tau), \tag{3.3}$$

where $\mathbf{F}(\tau)$ characterizes the deformation of the mixture occupying the configuration $\mathcal{B}(\tau)$ relative to the reference configuration \mathcal{B}_r . The total deformation of the collagen fiber generated at time τ and occupying the current configuration $\mathcal{B}(t)$ is then characterized by the gradient $\mathbf{F}^c(t, \tau)$, defined in Fig. 1. It has the form

$$\mathbf{F}^c(t, \tau) = \mathbf{F}(t)\mathbf{F}(\tau)^{-1}\mathbf{G}(\tau), \tag{3.4}$$

where the quantities on the right hand side must be known or specified by an evolution equation.

3.2 Fiber remodeling

In this section, we focus on the interaction between mechanical stretch and remodeling of *existing* collagen fibers [28,45]. Specifically, we define remodeling a continuous process where the microstructure of collagen changes resulting in the evolution of its stress-free configuration [9,48]. The microstructure of the newly formed collagen consists of long, oriented, and wavy macromolecules, which under tensile load first straighten and then begin to bear load. The remodeling process is conveniently described using the concept of recruitment variable defined in [28]. Briefly, the recruitment variable r is defined as the macroscopic stretch of the mixture, in the direction of the oriented fibers, when the collagen begin to bear load. Based on the definition of constrained mixtures, the macroscopic deformation \mathbf{F} coincides with the deformation of the matrix \mathbf{F}^e , where the superscript e refers to elastin.

The current configuration can be thought of as reached in two steps. First, traction forces deform the mixture from the reference configuration \mathcal{B}_r to an intermediate configuration, denoted \mathcal{B}_0 , where the collagen fibers straighten and begin to bear load, and subsequently to the current configuration $\mathcal{B}(t)$, see Fig. 2. The intermediate configuration \mathcal{B}_0 is, of course, not really a standard geometric configuration of the body. It is, in general, a geometrically incompatible configuration with gaps and overlaps between adjacent volume elements [49,50]. The macroscopic deformation gradient can therefore be decomposed as

$$\mathbf{F} = \mathbf{F}^c \mathbf{F}_r, \tag{3.5}$$

where \mathbf{F}_r determines the intermediate configuration with respect to \mathcal{B}_r . The gradient \mathbf{F}^c characterizes the deformation of the collagen with respect to the intermediate configuration and is used to calculate the elastic strain of the collagen fibers.

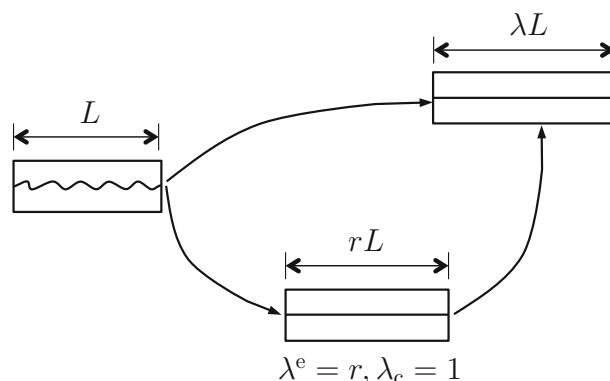
For purpose of illustration, it is convenient to focus on a transversely isotropic mixture subject to uniform extension in the direction of the oriented collagen fibers. The reference configuration is given by an elastic rod of total length L with embedded wavy collagen fibers with mean orientation along the axial direction [51], see Fig. 3. An axial force deforms the rod from the reference to the current configuration, which is characterized by the total length λL . The total stretch of the elastin matrix is then given by $\lambda^e = \lambda$. The intermediate configuration is reached when the total length of the sample becomes rL . The corresponding elastic stretches of the matrix and of the collagen fiber are, respectively, $\lambda^e = r$ and $\lambda^c = 1$. The fiber stretch in the current configuration with respect to the intermediate configuration is then given by

$$\lambda^c = \frac{\lambda}{r} = \frac{\lambda^e}{r}, \tag{3.6}$$

which is Eq. (3.5) specialized to uniform extension.

Biochemical processes induce alterations in the collagen microstructure and in the ability to carry load [52,53]. Equation (3.6) shows that an increasing value of r , for constant value of λ^e , reduces the value of λ^c and therefore the

Fig. 3 Uniaxial extension of transversely isotropic mixture showing intermediate configuration where the fibers straighten and begin to bear load



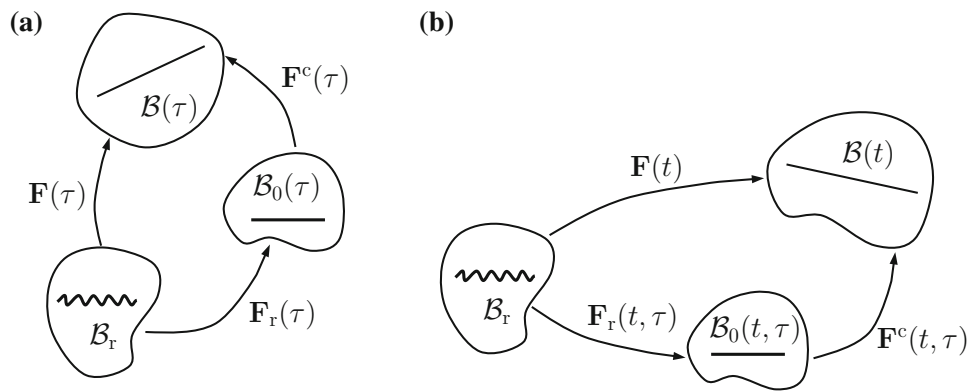


Fig. 4 Image **a** shows that at time τ a new collagen fiber is stretched and deposited into the mixture occupying $\mathcal{B}(\tau)$. The fiber begins to bear load in the intermediate configuration $\mathcal{B}_0(\tau)$. Imagine that at time t the mixture is unloaded from $\mathcal{B}(t)$ to the reference state \mathcal{B}_r . In **b** the fiber will first return to a straight, stress-free state, which represents the evolved intermediate state $\mathcal{B}_0(t, \tau)$, i.e. the natural configuration at time t of the fiber deposited at time τ

amount of load carried by the collagen fibers. Different values of r and their implications on the material response are considered in [28].

3.3 Fiber deposition and remodeling

The two events summarized in Sects. 3.1 and 3.2 are now combined to account for the deposition of new and the remodeling of embedded collagen fibers. Figure 4 shows the reference configuration \mathcal{B}_r and the deformed configurations of the body at times $t = \tau$ and at the current time t . The deformation gradients with respect to \mathcal{B}_r , corresponding to each configuration, are denoted by $\mathbf{F}(\tau)$ and $\mathbf{F}(t)$, respectively.

At time τ a new collagen fiber is deposited in a *stretched* state into the mixture occupying the configuration $\mathcal{B}(\tau)$, which is represented schematically by a straight line in Fig. 4a. The deposition stretch coincides with the stretch of the mixture in the direction of the newly deposited fiber. Hence, the stress in the new fiber is not equal to the stress in the existing material [30].

Imagine the mixture with the newly deposited fiber is now unloaded from $\mathcal{B}(\tau)$ to the reference configuration \mathcal{B}_r . The fiber will first return to the straighten, stress-free configuration, denoted $\mathcal{B}_0(\tau)$. The corresponding deformation gradient of the mixture is $(\mathbf{F}^c(\tau))^{-1}$. Upon further unloading of the mixture, characterized by $\mathbf{F}_r^{-1}(\tau)$, the fiber will cease to bear loads and assume a wavy shape. The deformation gradient in the intermediate configuration relative to the reference configuration has the form:

$$\mathbf{F}_r(\tau) = (\mathbf{F}^c(\tau))^{-1} \mathbf{F}(\tau), \quad (3.7)$$

which is Eq. (3.5) applied to the mixture at time τ .

The collagen fiber, deposited at time τ , undergoes affine deformation and will remodel as the mixture evolves from the configuration $\mathcal{B}(\tau)$ to $\mathcal{B}(t)$. Imagine that the mixture is now unloaded from the current configuration $\mathcal{B}(t)$ to the reference state \mathcal{B}_r , see Fig. 4b. The fiber will first return to a straighten, stress-free state, which represents an evolved intermediate state $\mathcal{B}_0(t, \tau)$. It is the natural configuration at time t of the fiber deposited at time τ . During the first part of the unloading, the deformation gradient of the mixture is denoted by $(\mathbf{F}^c(t, \tau))^{-1}$. Upon further unloading, the fiber will cease to bear loads and assume a different wavy state in the reference configuration. Unloading from the intermediate configuration $\mathcal{B}_0(t, \tau)$ is given by $\mathbf{F}_r^{-1}(t, \tau)$. It follows that the deformation gradient in the evolving intermediate configuration $\mathcal{B}_0(t, \tau)$ relative to the reference configuration \mathcal{B}_r is given by

$$\mathbf{F}_r(t, \tau) = (\mathbf{F}^c(t, \tau))^{-1} \mathbf{F}(t). \quad (3.8)$$

Combining equations (3.7) and (3.8) gives the deformation gradient of a fiber in the current configuration $\mathcal{B}(t)$ with respect to the evolving natural configuration $\mathcal{B}_0(t, \tau)$ as

$$\mathbf{F}^c(t, \tau) = \mathbf{F}(t)\mathbf{F}^{-1}(\tau)\mathbf{F}^c(\tau)\mathbf{F}_r(\tau)\mathbf{F}_r^{-1}(t, \tau), \tag{3.9}$$

where we emphasize that $\mathbf{F}_r(t, \tau)$ depends on $\mathbf{F}_r(\tau)$.

4 Growth and remodeling

We have not yet used the term *growth*, and therefore, for accurateness, a definition is warranted. We follow the suggestion given in [30] where growth describes an increase in mass locally, achieved via production of new material that exceeds removal of old material. Hence, detailed formulations of the rates of production and removal of constituents are critical to characterize growth and remodeling.

4.1 Mass balance

Consider the mass of constituent i per volume of mixture at time t , referred to as *apparent mass density* $\rho^i(\mathbf{x}, t)$, and the local rate of mass density production $m^i(\mathbf{x}, t)$ within the current configuration $\mathcal{B}(t)$. It follows that the mass balance can be written in the Eulerian form as

$$\frac{d}{dt} \int_{\mathcal{B}_t} \rho^i d v = \int_{\mathcal{B}_t} m^i d v. \tag{4.1}$$

Now, define an infinitesimal reference volume dV , which due to growth transforms into $d v$ in \mathcal{B}_t as given in (2.3). It follows that

$$\rho^i(\mathbf{x}, t) = \rho^i(0) + \frac{1}{J} \int_0^t m^i J d \tau, \tag{4.2}$$

where $\rho^i(0)$ denotes the apparent mass density of the constituent generated prior to the initiation of growth. The overall mass density of the mixture at time t is then given by

$$\rho(\mathbf{x}, t) = \sum_i \rho^i(\mathbf{x}, t), \tag{4.3}$$

which is assumed *constant*, hence $\rho(\mathbf{x}, t) = \rho(\mathbf{x}) = \sum_i \rho^i(\mathbf{x}, 0)$ [31,32,36]. Since the rate of mass production of one constituent is not, in general, equal to the rate of removal of another, it follows that $\sum m^i \neq 0$.

The mass balance equation in the form (4.2) only accounts for the production of new material. It does not address the continual removal of exiting material from the mixture. The mass balance equation is therefore augmented by introducing a survival function $Q^i(t, \tau)$ that specifies the fraction of constituent i , which is produced at time τ and survives to the current time t . The generalization of Eq. (4.2) yields

$$\rho_r^i(t) = \rho_r^i(0) Q^i(t, 0) + \int_0^t m_r^i(\tau) Q^i(t, \tau) d \tau, \tag{4.4}$$

where $\rho_r^i(t)$, $\rho_r^i(0)$, $m_r^i(\tau)$ denote quantities now defined per unit reference volume and $\rho_r(t) = \sum_i \rho_r^i(t)$. The survival function $Q^i(t, 0)$ represents the fraction of constituent i , produced prior to time $t = 0$, that survives to the current time t . Recall that the material response is assumed incompressible in the homeostatic state and therefore the mixture satisfies the internal constraint $J \equiv 1$ up to $t = 0$.

5 Energy function

A rule-of-mixture relation where the Cauchy stress $\boldsymbol{\sigma}$ is the sum of the stress in each constituent is introduced in [31,32]. From equation (2.8)₂, it follows that the Cauchy stress $\boldsymbol{\sigma}$ at time t is given by

$$\boldsymbol{\sigma}(t) = J^{-1}(t)\mathbf{F}(t)\frac{\partial W(t)}{\partial \mathbf{F}(t)} = J^{-1}(t)\mathbf{F}(t)\frac{\partial \sum_i W^i(t)}{\partial \mathbf{F}(t)}, \quad (5.1)$$

where $W^i(t)$ denotes the strain energy density of the constituent i , and $\mathbf{F}(t)$ characterizes the deformation of the mixture at time t relative to the reference configuration \mathcal{B}_r and $J = \det \mathbf{F}(t)$.

The formulation of constitutive equations is simplified if the strain energy density W is replaced by the internal energy density, denoted U . The strain energy is measured per unit reference volume, whereas the internal energy is usually measured per unit mass. For an elastic material, they are connected by

$$W = \rho_r U, \quad (5.2)$$

where ρ_r is the reference density. This suggests to write the energy density $W^i(t)$ in terms of the internal energy density $U^i(t)$. We now write

$$W^i(t) = \rho_r^i(0) Q^i(t, 0) U^i(\mathbf{F}^i(t)) + \int_0^t m_r^i(\tau) Q^i(t, \tau) U^i(\mathbf{F}^i(t, \tau)) d\tau, \quad (5.3)$$

where $U^i(\mathbf{F}^i(t))$ denotes the internal energy at time t of constituent i , which is present in the mixture in the homeostatic state. The gradient $\mathbf{F}^i(t)$ describes the deformation of constituent i with respect to the reference configuration \mathcal{B}_r . $U^i(\mathbf{F}^i(t, \tau))$ is the internal energy at time t of constituent i produced at time τ and $\mathbf{F}^i(t, \tau)$ characterizes the corresponding deformation.

The stored energy function (2.14), for an anisotropic mixture with two preferred directions and characterized by volume change J , has the specialized form:

$$\bar{W}(t) = \sum_i \bar{W}_{\text{iso}}^i(t) + \bar{W}_{\text{vol}}(t) = \sum_i \rho_r^i(t) \bar{U}_{\text{iso}}^i(t) + \bar{W}_{\text{vol}}(t), \quad (5.4)$$

where each constituent i is characterized by the energy function $\bar{W}_{\text{iso}}^i(t) = \rho_r^i(t) \bar{U}_{\text{iso}}^i(t)$.

6 Application to aneurysm development

The theory presented in Sect. 4 is now specialized to model local dilatation of an abdominal aorta, triggered by changes in the mechanical environment. The reference configuration \mathcal{B}_r of the aorta is represented as a thick-walled tube, which in terms of cylindrical polar coordinates (R, Θ, Z) is specified by

$$A \leq R \leq B, \quad 0 \leq \Theta \leq 2\pi, \quad -L \leq Z \leq L, \quad (6.1)$$

where A and B are the internal and external radii and $2L$ is the length of the tube. The associated unit basis vectors are $\mathbf{E}_R, \mathbf{E}_\Theta, \mathbf{E}_Z$ and the location of a material particle is identified by the position vector

$$\mathbf{X} = R\mathbf{E}_R + Z\mathbf{E}_Z. \quad (6.2)$$

6.1 Homeostatic state

In the homeostatic state, from $-\infty \leq t < 0$, the amount of material removed is balanced by newly created constituents and therefore no change in local mass occurs. From Eq. (2.3), assuming material incompressibility, it follows that $J \equiv 1$.

The idealized geometry of the aorta is maintained as a thick-walled cylindrical tube with circular cross-sectional area subject to constant internal pressure and axial stretch. The corresponding configuration is defined in terms of cylindrical polar coordinates (r, θ, z) with unit basis vectors $\mathbf{e}_r, \mathbf{e}_\theta, \mathbf{e}_z$ as

$$a \leq r \leq b, \quad 0 \leq \theta \leq 2\pi, \quad -l \leq z \leq l, \tag{6.3}$$

where a, b are the internal and external radii of the tube and $2l$ is the current length. Note that in Sects. 6.1 and 6.2 the variable r is used to denote the cylindrical polar coordinate and should not be confused with the recruitment variable r introduced in Section 3.2. Then, the condition of incompressibility yields

$$r = \sqrt{a^2 + \lambda_z^{-1} (R^2 - A^2)}, \quad \theta = \Theta, \quad z = \lambda_z Z, \tag{6.4}$$

where λ_z is the axial stretch. The current position of a particle, located at \mathbf{X} in the reference geometry, is identified by the position vectors \mathbf{x} . Using polar coordinates this is given by

$$\mathbf{x} = r\mathbf{e}_r + z\mathbf{e}_z, \tag{6.5}$$

and is used to calculate the deformation gradient \mathbf{F} as

$$\mathbf{F} = \frac{\partial \mathbf{x}}{\partial R} \otimes \mathbf{E}_R + \frac{1}{R} \frac{\partial \mathbf{x}}{\partial \Theta} \otimes \mathbf{E}_\Theta + \frac{\partial \mathbf{x}}{\partial Z} \otimes \mathbf{E}_Z = \frac{dr}{dR} \mathbf{e}_r \otimes \mathbf{E}_R + \frac{r}{R} \mathbf{e}_\theta \otimes \mathbf{E}_\Theta + \frac{dz}{dZ} \mathbf{e}_z \otimes \mathbf{E}_Z, \tag{6.6}$$

which is the spectral form of \mathbf{F} with respect to the cylindrical polar coordinates. The corresponding eigenvalues are the principal stretches in the radial, azimuthal and axial directions given, respectively, by

$$\lambda_1 = \frac{dr}{dR} = \lambda_2^{-1} \lambda_3^{-1}, \quad \lambda_2 = \frac{r}{R}, \quad \lambda_3 = \lambda_z. \tag{6.7}$$

It follows from (2.9)₁ that the nominal stress tensor \mathbf{P} has the spectral form:

$$\mathbf{P} = P_{Rr} \mathbf{E}_R \otimes \mathbf{e}_r + P_{\Theta\theta} \mathbf{E}_\Theta \otimes \mathbf{e}_\theta + P_{Zz} \mathbf{E}_Z \otimes \mathbf{e}_z, \tag{6.8}$$

and the equilibrium equation (2.10)₁ specializes to the single component

$$\frac{\partial P_{Rr}}{\partial R} + \frac{1}{R} (P_{Rr} - P_{\Theta\theta}) = 0. \tag{6.9}$$

The boundary conditions are considered next. In the current configuration the outer lateral surface $r = b$ is kept traction free, so that $\boldsymbol{\sigma} \mathbf{n} = \mathbf{0}$, where \mathbf{n} is the unit outward normal, i.e. $\mathbf{n} = \mathbf{e}_r$. On the inner surface, there is a pressure P , defined per unit deformed area such that $\boldsymbol{\sigma} \mathbf{n} = -P \mathbf{n}$ on $r = a$ with $\mathbf{n} = -\mathbf{e}_r$. Integrating over the inner surface, applying Nanson’s formula, gives the nominal traction per unit reference area

$$\mathbf{P}^T \mathbf{N} = -P \mathbf{F}^{-T} \mathbf{N}, \tag{6.10}$$

where the unit outward normal to the inner lateral surfaces in the reference configuration is $\mathbf{N} = -\mathbf{E}_R$. The boundary conditions on the inner and outer surfaces are then given as

$$P_{Rr} = \begin{cases} -P(F^{-1})_{Rr} = -P\lambda_2\lambda_3 & \text{on } R = A, \\ 0 & \text{on } R = B. \end{cases} \tag{6.11}$$

6.2 Aneurysm development

In the study of aneurysm development, we restrict attention to axisymmetric shapes, which requires some modifications to the theory presented in Sect. 6.1. The formation of an aneurysm is associated with a local change in mass and therefore, for constant density, $J \neq 1$. A typical material point in the deformed configuration is now identified by the position vector

$$\mathbf{x} = r\mathbf{e}_r + z\mathbf{e}_z, \tag{6.12}$$

where

$$r = r(R, Z), \quad \theta = \Theta, \quad z = z(R, Z). \tag{6.13}$$

The deformation gradient tensor is obtained as $\mathbf{F} = \text{Grad } \mathbf{x}$, where Grad is the gradient operator in cylindrical polar coordinates. The explicit form becomes

$$\begin{aligned} \mathbf{F} &= \frac{\partial \mathbf{x}}{\partial R} \otimes \mathbf{E}_R + \frac{1}{R} \frac{\partial \mathbf{x}}{\partial \Theta} \otimes \mathbf{E}_\Theta + \frac{\partial \mathbf{x}}{\partial Z} \otimes \mathbf{E}_Z, \\ &= r_R \mathbf{e}_r \otimes \mathbf{E}_R + \lambda_2 \mathbf{e}_\theta \otimes \mathbf{E}_\Theta + r_Z \mathbf{e}_r \otimes \mathbf{E}_Z + z_R \mathbf{e}_z \otimes \mathbf{E}_R + z_Z \mathbf{e}_z \otimes \mathbf{E}_Z, \end{aligned} \tag{6.14}$$

where $\lambda_2 = r/R$ and the subscripts R and Z indicate, respectively, the partial derivatives $\partial/\partial R$ and $\partial/\partial Z$ of the vector components r and z . The matrix of the deformation tensor \mathbf{F} and its inverse are given by

$$\mathbf{F} = \begin{pmatrix} r_R & 0 & r_Z \\ 0 & \lambda_2 & 0 \\ z_R & 0 & z_Z \end{pmatrix}, \quad \mathbf{F}^{-1} = J^{-1} \begin{pmatrix} \lambda_2 z_Z & 0 & -\lambda_2 r_Z \\ 0 & r_R z_Z - r_Z z_R & 0 \\ -\lambda_2 z_R & 0 & \lambda_2 r_R \end{pmatrix}, \tag{6.15}$$

where the change in volume satisfies the constraint

$$J = \det \mathbf{F} = \lambda_2(r_R z_Z - r_Z z_R). \tag{6.16}$$

From Eq. (2.9)₁, it follows that the nominal stress tensor \mathbf{P} has components, denoted \mathbf{P} , given by

$$\mathbf{P} = \begin{pmatrix} P_{Rr} & 0 & P_{Rz} \\ 0 & P_{\Theta\theta} & 0 \\ P_{Zr} & 0 & P_{Zz} \end{pmatrix}. \tag{6.17}$$

The radial and axial components of the equilibrium equation (2.10)₁ require

$$\frac{\partial}{\partial R}(R P_{Rr}) - P_{\Theta\theta} + \frac{\partial}{\partial Z}(R P_{Zr}) = 0, \tag{6.18}$$

$$\frac{\partial}{\partial R}(R P_{Rz}) + \frac{\partial}{\partial Z}(R P_{Zz}) = 0, \tag{6.19}$$

while the component in the circumferential direction is identically satisfied.

The equilibrium equations (6.18) and (6.19) can be integrated through the thickness in the reference configuration, to give

$$[RP_{Rr}]_A^B - \int_A^B P_{\Theta\theta} dR + \frac{\partial}{\partial Z} \int_A^B RP_{Zr} dR = 0, \quad (6.20)$$

$$[RP_{Rz}]_A^B + \frac{\partial}{\partial Z} \int_A^B RP_{Zz} dR = 0. \quad (6.21)$$

At this point, we again consider the boundary conditions. In the current configuration, there is a pressure P , defined per unit deformed area, applied to the inner surface, while the outer surface is traction free. It follows from (6.10) that these boundary conditions can be recast in terms of the nominal stress as

$$P_{Rr} = \begin{cases} -P(F^{-1})_{Rr} = -PJ^{-1}\lambda_2 z_Z & \text{on } R = A, \\ 0 & \text{on } R = B, \end{cases} \quad (6.22)$$

$$P_{Rz} = \begin{cases} -P(F^{-1})_{Rz} = PJ^{-1}\lambda_2 r_Z & \text{on } R = A, \\ 0 & \text{on } R = B. \end{cases} \quad (6.23)$$

It follows that Eqs. (6.20) and (6.21) specialize to

$$PAJ^{-1}\lambda_2(A, Z)z_Z(A, Z) - \int_A^B P_{\Theta\theta} dR + \frac{\partial}{\partial Z} \int_A^B RP_{Zr} dR = 0, \quad (6.24)$$

$$-PAJ^{-1}\lambda_2(A, Z)r_Z(A, Z) + \frac{\partial}{\partial Z} \int_A^B RP_{Zz} dR = 0, \quad (6.25)$$

where $\lambda_2(A, Z) = r(A, Z)/A$.

6.3 Constitutive model

Expressions of the internal energy, mass production and survival function must be specified to solve the equilibrium equations (6.9), (6.24) and (6.25). In addition, due to irregular geometry and boundary conditions, numerical methods must be used to solve the equations governing aneurysm development. Also note that the geometry and boundary conditions, as well as the natural configuration of some constituents, may evolve due to growth and remodeling.

6.3.1 Volumetric contribution

The form of the volumetric contribution $\bar{W}_{\text{vol}}(t)$ to the total energy (5.4) is taken as

$$\bar{W}_{\text{vol}}(t) = \frac{1}{2}\kappa \left(\frac{J(t)}{J(t^-)} - 1 \right)^2, \quad (6.26)$$

where κ is referred to as a penalty parameter to enforce the volumetric response during short-term events [36, 54]. Any volume change $J(t)$ is due to removal of existing and deposition of new materials and is obtained from (4.2), using (4.3), and $J(t^-)$ is the volume change during the previous time increment. Note that discrete time increments are used in (6.26) to describe the mechanics that otherwise is based on time-continuous quantities. Equivalent, time-continuous formulations are used in, for example, [23, 55].

Equation (6.26), combined with mass production/degradation equations like (4.4), imposes the very special case of ‘isotropic growth’. Limitations and unphysiological results associated with isotropic growth are addressed in [23, 55].

6.3.2 Isotropic matrix

The energy function contains contributions from the isotropic matrix and the embedded collagen fibers. Elastin is not continuously produced in a mature arterial wall [34,36]. Therefore, the contribution of the elastin matrix in Eq. (5.4) has the form

$$\bar{W}_{\text{iso}}^e(t) = \rho_r^e(0) Q^e(t, 0) \bar{U}_{\text{iso}}^e(\bar{\mathbf{F}}(t)), \quad (6.27)$$

where we recall that the superscript e denotes the constituent elastin. Following [32,35,36,43] the mechanical behavior is represented by the energy function

$$\bar{U}_{\text{iso}}^e(t) = \frac{1}{2} c^e (\bar{I}_1(t) - 3), \quad (6.28)$$

where c^e is a material parameter of the isotropic matrix. The deformation of elastin in the current configuration $\mathcal{B}(t)$, relative to the reference configuration \mathcal{B}_r , is described by $\mathbf{F}(t)$. It follows that the first isochoric invariant $\bar{I}_1(t) = \text{tr} \bar{\mathbf{C}}(t)$ where $\bar{\mathbf{C}}(t) = \bar{\mathbf{F}}^T(t) \bar{\mathbf{F}}(t)$ and $\bar{\mathbf{F}}(t) = J^{-1/3} \mathbf{F}(t)$.

In the homeostatic state, the blood vessels are in a so-called ‘mechanobiologically stable’ regime [56,57]. If this is the case, a loss of wall material can easily be compensated by growth and remodeling without a significant dilatation of the artery (that is, without an aneurysm). By contrast, if this is not the case—if the vessel is in a ‘mechanobiologically unstable’ regime—not only a minor loss of wall material but also any other minor perturbation (such as a minor increase in blood pressure) can cause an aneurysm. In this work, for simplicity, we assume that aneurysm formation is initiated by a localized degradation of the matrix material, which is accounted for by assuming that the degradation function $Q^e(t, 0)$ in (6.27) deviates from unity [28]. The age-related degradation of elastin is, in general, not significant and may therefore be neglected. For illustrative purpose, consider the axisymmetric function:

$$Q^e(t, 0) = \begin{cases} \left[1 + q^e \left(\frac{Z^2}{L_d^2} - 1 \right) \right]^t & \text{for } -L_d \leq Z \leq L_d, \\ 1 & \text{for } Z < -L_d, \quad Z > L_d, \end{cases} \quad (6.29)$$

where q^e is an elastin-specific material parameter and $\pm L_d$ is the axial distance over which degradation occurs. For illustrative purposes, we assume that the function $Q^e(t, 0)$ is independent of the radial distance R .

6.3.3 Collagen fibers

In this section, we focus on the stored energy of embedded collagen fibers, on the kinetics of turnover and on the remodeling.

The mass per unit reference volume of any constituent in the mixture at time t is given by (4.4), which, when specialized to collagen, has the form:

$$\rho_r^c(t) = \rho_r^c(0) Q^c(t, 0) + \int_0^t m_r^c(\tau) Q^c(t, \tau) d\tau, \quad (6.30)$$

where the superscript c stands for collagen. The survival functions, $Q^c(t, 0)$ and $Q^c(t, \tau)$, define, respectively, the fractions of collagen present in the homeostatic state and those generated at time τ that survive up to the current time t . Equation (6.30) also shows that the amount of collagen generated is quantified by the density production $m_r^c(\tau)$. It follows that the energy function (5.4), for isochoric deformation, becomes

$$\bar{W}_{\text{iso}}^c(t) = \rho_r^c(0) Q^c(t, 0) \bar{U}_{\text{iso}}^c(\bar{\mathbf{F}}^c(t, 0)) + \int_0^t m_r^c(\tau) Q^c(t, \tau) \bar{U}_{\text{iso}}^c(\bar{\mathbf{F}}^c(t, \tau)) d\tau. \tag{6.31}$$

Following [19,36,43], the stored energy of the two families of oriented fibers has the form:

$$\bar{U}_{\text{iso}}^c(\bar{\mathbf{F}}^c(t, \tau)) = \frac{k^c}{2k} \sum_{j=4,6} \left\{ \exp \left[k (\bar{I}_j - 1)^2 \right] - 1 \right\}, \tag{6.32}$$

where k^c is a material constant related to the degree of anisotropy generated by the fibers and k is a dimensionless parameter. The isochoric invariants \bar{I}_4, \bar{I}_6 , defined in (2.15), can be computed as

$$\bar{I}_4 = \mathbf{M} \cdot [\bar{\mathbf{C}}^c(t, \tau) \mathbf{M}], \quad \bar{I}_6 = \mathbf{M}' \cdot [\bar{\mathbf{C}}^c(t, \tau) \mathbf{M}'], \tag{6.33}$$

where we recall that \mathbf{M}, \mathbf{M}' are unit vectors in the natural configuration that define the preferred directions of the material. The isochoric right Cauchy-Green tensor $\bar{\mathbf{C}}^c(t, \tau) = (\bar{\mathbf{F}}^c(t, \tau))^T \bar{\mathbf{F}}^c(t, \tau)$, where $\bar{\mathbf{F}}^c(t, \tau) = J^{-1/3} \mathbf{F}^c(t, \tau)$ is the isochoric part of the deformation of a fiber generated at time τ and occupying the current configuration $\mathcal{B}(t)$. The deformation is measured from the intermediate configuration $\mathcal{B}_0(t, \tau)$, see Fig. 4. The energy of collagen $\bar{U}_{\text{iso}}^c(\bar{\mathbf{F}}^c(t, 0))$, which is part of the mixture in the homeostatic state at time $t = 0$ and survives to the current time t , has a form identical to (6.32). However, the deformation is now measured from the reference configuration \mathcal{B}_r such that $\bar{\mathbf{F}}^c(t, 0) = \bar{\mathbf{F}}(t) \bar{\mathbf{F}}_r^{-1}(t, 0)$, where $\bar{\mathbf{F}}_r^{-1}(0)$ is defined in (3.7). The isochoric right Cauchy-Green tensor used to evaluate the corresponding invariants \bar{I}_4, \bar{I}_6 is then calculated as $\bar{\mathbf{C}}^c(t, 0) = (\bar{\mathbf{F}}^c(t, 0))^T \bar{\mathbf{F}}^c(t, 0)$.

In (6.30), the degradation of collagen fibers is accounted for by the survival functions $Q^c(t, 0)$ and $Q^c(t, \tau)$. To quantify the effects of collagen turnover on the rupture risk of abdominal aortic aneurysms, we follow [34,58] and use

$$Q^c(t, \tau) = \exp \left[- \int_{\tau}^t \bar{q}^c(\bar{\tau}) d\bar{\tau} \right], \tag{6.34}$$

yielding results consistent with clinical observation on AAA development. For ease of reference, we briefly review the main ingredients of (6.34). The function $\bar{q}^c(\bar{\tau})$, using additive contributions, characterizes the time- and stretch-dependent degradations of the collagen content by

$$\bar{q}^c(\bar{\tau}) = q^c \left(1 + w_u^c \Delta T_{\lambda}^c(\bar{\tau})^2 \right), \tag{6.35}$$

where the rate parameter q^c captures the half-life of collagen in the homeostatic state as $t_{1/2}^{c,h} = \ln(2)/q^c$. The collagen-specific weighting function is defined as $w_u^c = (t_{1/2}^{c,h}/t_{1/2}^{c,u} - 1)$, where $t_{1/2}^{c,u}$ denotes the half-life of collagen in the unloaded state. The function $\Delta T_{\lambda}^c(\bar{\tau})$ is defined as

$$\Delta T_{\lambda}^c(\bar{\tau}) = \frac{\lambda^c(\bar{\tau}) - \lambda_h^c}{\lambda_h^c}, \tag{6.36}$$

where $\lambda^c(\bar{\tau})$ denotes the stretch of the collagen fiber produced at time τ , evaluated at $\bar{\tau} \in [\tau, t]$, and λ_h^c is the corresponding stretch in the homeostatic state. Equation (6.36) implies that the survival function $Q^c(t, \tau)$ decreases faster with increasing collagen fiber stretch. Recall that in a thick-walled tube under internal pressure, the stretch in the fiber direction depends on time and on the radial coordinate r . For clarity of presentation, the dependence on the variable r is not shown in (6.36). Other authors considered the radial dependence as an unphysiological condition and assumed a hemostatic initial state with uniform homeostatic collagen stretch [23,55].

Equation (6.30) shows that the total amount of collagen present in the mixture depends on the density production $m_r^c(\tau)$. Similar to (6.35), we define the stretch-mediated collagen production by

$$m_r^c(\tau) = m_r(0) \left(1 + k_\lambda^c \Delta T_\lambda^c(\tau)\right), \quad (6.37)$$

where $m_r(0)$ is the rate of production in the homeostatic state, referred to as basal rate of production in [34, 58]. The material parameter k_λ^c is a scaling parameter and $\Delta T_\lambda^c(\tau)$ has the form (6.36) with $\bar{\tau}$ replaced by τ .

The evolving intermediate configurations of the mixture are defined in Sect. 3.3 and shown schematically in Fig. 4. The corresponding deformations with respect to the reference configuration \mathcal{B}_r , at times τ and t , are characterized by $\mathbf{F}_r(\tau)$ and $\mathbf{F}_r(t, \tau)$. For illustrative purpose, assume that the fiber directions, specified by the unit vectors \mathbf{M} and \mathbf{M}' , are not altered by the deformation from the reference to the intermediate configuration. Therefore, to account for fiber remodeling, we define

$$\begin{aligned} \mathbf{F}_r(\tau) &= r(\tau) \mathbf{M} \otimes \mathbf{M} + \frac{1}{\sqrt{r(\tau)}} (\mathbf{I} - \mathbf{M} \otimes \mathbf{M}), \\ \mathbf{F}_r(t, \tau) &= r(t, \tau) \mathbf{M} \otimes \mathbf{M} + \frac{1}{\sqrt{r(t, \tau)}} (\mathbf{I} - \mathbf{M} \otimes \mathbf{M}) \end{aligned} \quad (6.38)$$

and similar expression for the fibers oriented along \mathbf{M}' . Recall that the recruitment variable r defines the remodeling of embedded collagen fibers. For a nonaxisymmetric dilatation, since there are two families of oriented fibers, it will, in general, not be possible to define a unique \mathbf{F}_r such that it maps from the reference configuration to an intermediate configuration where both fiber families are stress-free (and at the edge of recruitment) at the same time. It follows that separate recruitment variables need to be defined for each collagen fiber family combined with separate intermediate configurations \mathcal{B}_0 . In what follows, $r(\tau)$ and $r(t, \tau)$ denote the recruitment variables of a fiber generated at time τ and of the same fiber at time t . These quantities are related by

$$r(t, \tau) = r(\tau) + \int_\tau^t r^c \Delta T_\lambda^c(\bar{\tau}) d\bar{\tau}, \quad (6.39)$$

where r^c is a scaling factor for the stretch-mediated fiber remodeling and $\Delta T_\lambda^c(\bar{\tau})$ is given in (6.36). Equations (3.9) and (6.33) give, respectively, the deformation of the collagen with respect to the intermediate configuration and the corresponding invariants.

In the numerical simulation, we assume that in the homeostatic state the recruitment variable, denoted $r(0)$, is constant and known. At time τ , the recruitment variable of collagen produced in the homeostatic state changes as specified by (6.39), i.e.

$$r(\tau, 0) = r(0) + \int_0^\tau r^c \Delta T_\lambda^c(\bar{\tau}) d\bar{\tau}. \quad (6.40)$$

It follows that the stretch of a fiber at time τ , produced in the homeostatic state, is given by $\lambda^c(\tau, 0) = \lambda^e(\tau)/r(\tau, 0)$, see Eq. (3.6). Imagine that at time τ a new fiber is deposited into the mixture with the pre-stretch $\lambda^c(\tau) = \lambda^c(\tau, 0)$. It follows that the requirement variable of the newly deposited fiber $r(\tau) = r(\tau, 0)$.

7 Computational model and results

In order to illustrate the theory of the preceding sections, we now summarize the numerical results of a nonlinear finite element analysis that uses patient-based material parameters, if available, and published values otherwise. The numerical procedure makes use of a purposely written material subroutine, called UMAT, based on the constitutive formulations given in (6.26), (6.27) and (6.31), and uses Abaqus to solve the corresponding equations.

Table 1 Baseline values of the material parameters of elastin in the isochoric part of the energy (6.27) and (6.28) and in the degradation function (6.29)

Summary of material parameters for elastin			
$\rho_r^e(0)$ (kg/m ³)	c^e (J kg ⁻¹)	q^e	L_d (mm)
0.6 ρ_r	120	0.1	45

The overall density $\rho_r = 1050$ kg/m³

7.1 Model parameters

The reference geometry of the model, defined in Sect. 6, consists of a thick-walled tube of total length $2L = 120$ mm and inner and outer radii $A = 10$ mm and $B = 12$ mm, respectively, resulting in a uniform wall thickness of 2 mm. We assume that the axisymmetric shape is maintained during aneurysm development and therefore only one eighth of the cylindrical tube needs to be considered. The model uses 14,880 hexahedral elements connected at 19,360 nodes, with four elements through the thickness. Reduced integration and domain remeshing is used to avoid locking problems. The tube is allowed to expand radially at the entrance and exit, while axial displacements are held constant.

To simulate in vivo conditions, a uniform pressure of 16 kPa (120 mmHg) was applied to the inner surface of the tube [17].

7.2 Material parameters

The values of the material parameters c^e , k , k^c , used in the energy functions (6.28) and (6.32), are selected based on planar biaxial tests on tissue samples from a AAA resected during elective repair surgery [6, 19, 59]. During each test the axial stretch λ_z , corresponding to the direction \mathbf{E}_Z , was held constant at physiologically realistic values while the specimen was subjected to five loading-unloading cycles in the circumferential direction \mathbf{E}_Θ . Each specimen is assumed to include two families of parallel fibers oriented at angles $\pm\theta$ relative to the circumferential direction. The preferred directions are then defined by the unit vectors

$$\mathbf{M} = \cos\theta \mathbf{E}_\Theta + \sin\theta \mathbf{E}_Z, \quad \mathbf{M}' = \cos\theta \mathbf{E}_\Theta - \sin\theta \mathbf{E}_Z. \quad (7.1)$$

In the homeostatic state, the overall density is uniform and constant and equal to the reference density; hence $\rho(\mathbf{x}, 0) = \rho_r$. The initial mass fractions of elastin and collagen $\rho_r^e(0)$ and $\rho_r^c(0)$ are specified in terms of ρ_r ; see, for example, [34].

Equation (6.29) controls the local degradation of elastin in the region $Z = \pm L_d$ with the maximum amount defined by q^e at $Z = 0$. Degradation of collagen (6.34) is given in terms of half-life of the fibers in homeostatic tension $t_{1/2}^{c,h}$ and in the unloaded state $t_{1/2}^{c,u}$. The corresponding values are based on published data [29, 60].

The collagen mass density production $m_r^c(\tau)$, given in (6.37), is characterized by the scaling parameter k_λ^c and is within the range of values given in [34]. Finally, the amount of fiber remodeling is determined by the scaling factor r^c and by the recruitment variable in the homeostatic state $r(0)$ [29].

The penalty parameter in the function (6.26) was taken as $\kappa = 100,000$ kPa. Values of the material parameters for elastin are listed in Table 1, for collagen in Table 2.

7.3 Results

The first step in the simulation inflates the tube with an internal pressure of 16 kPa (120 mmHg) keeping $\lambda_z = 1$. The corresponding equilibrium configuration represents the homeostatic state for $t \leq 0$. In the healthy arterial wall,

Table 2 Baseline values of the material parameters of collagen in the isochoric part of the energy (6.31) and (6.32), in the degradation function (6.34), in collagen production (6.37) and in the recruitment function (6.39)

Summary of material parameters for collagen								
$\rho_r^c(0)$ (kg/m ³)	k^c (J kg ⁻¹)	k	θ (°)	$t_{1/2}^{c,h}$ (years)	$t_{1/2}^{c,u}$ (years)	k_λ^c	$r(0)$	r^c (year ⁻¹)
$0.4\rho_r$	75.2	11.2	± 15	0.8	0.2	50	1.03	0.8

The overall density $\rho_r = 1050\text{ kg/m}^3$

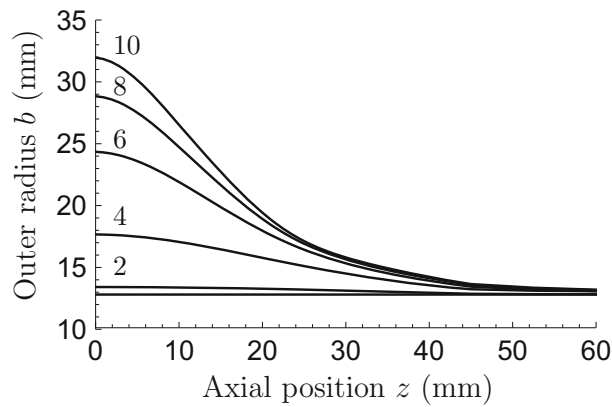


Fig. 5 The changes of the outer radius b of a dilating abdominal aorta over a 10-year period. The horizontal line represents the constant radius $b = 12.77\text{ mm}$ during the homeostatic state. The remaining graphs show the radius as a function of the axial position z at every second year. The change of radius from the unloaded state $B = 12\text{ mm}$ to the homeostatic state is not included

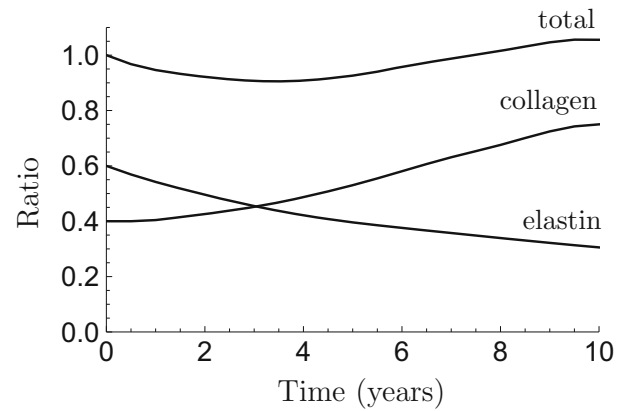


Fig. 6 Plots of density ratio between current and reference density. The changes of mass fractions of elastin $\rho_r^e(t)$ and collagen $\rho_r^c(t)$ are shown over a 10-year time frame. In the homeostatic state, these are $\rho_r^e(0) = 0.6\rho_r$ and $\rho_r^c(0) = 0.4\rho_r$ of the reference density $\rho_r = 1050\text{ kg/m}^3$

the protein elastin, neglecting age-related degradation, is considered stable, and therefore no turnover occurs [9]. Collagen, on the other hand, continuously degrades and regenerates keeping the total amount constant.

Aneurysm formation, which begins at $t = 0$, is accompanied by a loss of elastin (6.29) inducing a localized weakening of the arterial wall. The so induced dilatation yields an increase in the stretch of the collagen fibers. This, based on (6.36), triggers degradation of existing and deposition of new collagen as specified in (6.34) and (6.37). In addition, the embedded fibers remodel as detailed in (6.39), resulting in a continuous enlargement of the aneurysm bulge.

Figure 5 depicts the changes of the outer radius of a dilating abdominal aorta as a function of the axial position over a 10-year period with an applied pressure of 16 kPa (120 mmHg). The changes from the unloaded state, $A = 10\text{ mm}$ and $B = 12\text{ mm}$, to the homeostatic state, $a = 10.92\text{ mm}$ and $b = 12.77\text{ mm}$, are much smaller compared to those associated with the aneurysm formation, hence are not included. The numerical results show that the increase over time is nonlinear with the largest increase occurring between the fourth and sixth year. There is a small increase in radius of the healthy section, $Z > L_d = 45\text{ mm}$, generated by λ_z no longer constant along the axial direction.

Figure 6 illustrates the time dependent changes of ratios of elastin, collagen and total density over the homeostatic reference density $\rho_r = 1050\text{ kg/m}^3$. Specifically, the variations of elastin $\rho_r^e(t)$ and collagen $\rho_r^c(t)$, evaluated at the location of maximum bulge dilatation, are represented for a 10-year period. In the homeostatic state, $t \leq 0$, these are $\rho_r^e(0) = 60\%$ and $\rho_r^c(0) = 40\%$ of ρ_r . The figure shows that aneurysm formation is accompanied by a continuous reduction of elastin and by a gradual increase of collagen contents. During the same period the overall mass density increases by 5.5% with respect to the homeostatic state to $\rho_r(\mathbf{x}, 10\text{ years}) = 1180\text{ kg/m}^3$.

The stretch of the collagen fibers depends on the deformation of the matrix and on the intermediate configuration, which evolves with time as specified in (6.39). We visualize the effect of collagen remodeling by first evaluating

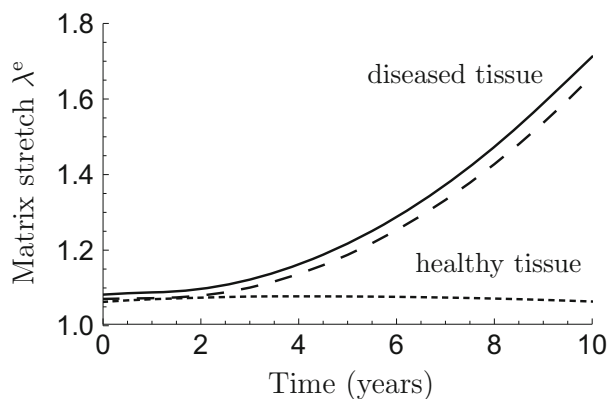


Fig. 7 The stretches of the matrix material λ^e along a fiber direction. The behavior of the diseased tissue is evaluated on the inner and outer surfaces at the location of maximum bulge dilatation and shown by *solid* and *dashed* lines, respectively. The stress of the healthy tissue is evaluated, outside the damage zone specified in (6.29), on the inner surface

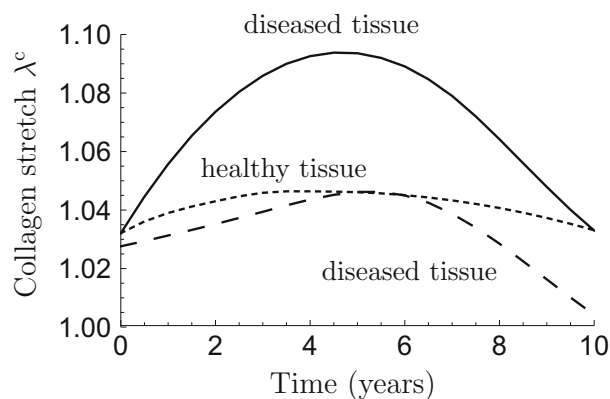
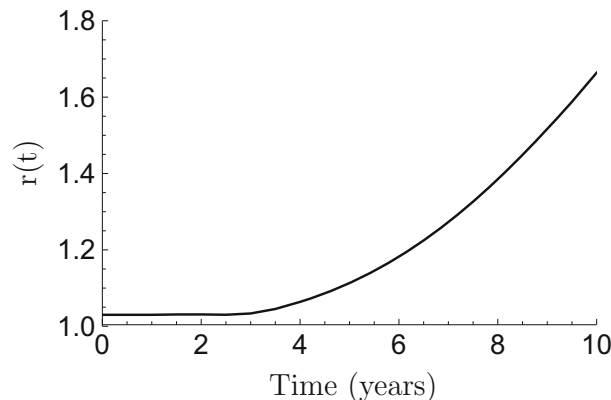


Fig. 8 The stretches λ^c of healthy and remodeled collagen fibers. Diseased fibers are evaluated on the inner and outer surfaces at the location of maximum bulge dilatation and shown by *solid* and *dashed* lines, respectively. The stretch of the healthy fiber is evaluated, outside the damage zone specified in (6.29), on the inner surface

Fig. 9 Changes of the recruitment variable $r(t)$ over a 10-year period. The recruitment variable defines the intermediate configuration where fibers straighten and begin to bear load



the stretch of the matrix along a fiber direction and then comparing the corresponding stretches $\lambda^e(t)$ and $\lambda^c(t)$. Figure 7 shows the stretches of the matrix material along a fiber direction of a healthy and a diseased tissue over a 10-year period. The response of the diseased tissue is evaluated on the inner and outer surfaces at the location of maximum bulge dilatation, shown by *solid* and *dashed* lines, respectively. The stretch of the healthy tissue, which is evaluated at the inner surface of the tube, initially increases from $\lambda^e(0) = 1.06$ to $\lambda^e(4) = 1.078$ and decreases afterwards. This behavior is explained by the variations of the axial stretch induced by the expanding aneurysm.

Figure 8 shows the changes of the collagen fiber stretch in healthy and diseased tissues over a 10-year period. As for the matrix material, the behavior of collagen is evaluated at the location of maximum bulge expansion on the inner and outer surfaces and shown by *solid* and *dashed* lines, respectively. For healthy collagen, we again restrict attention to the inner surface of the tube. The stretch of collagen is determined by the location of the intermediate configuration and is, in the healthy section given by $\lambda^c(t) = \lambda^e(t)/r(0)$, where the recruitment variable of the homeostatic state $r(0) = 1.03$. This condition is strictly true if and only if remodeling is set exactly to zero in the healthy tissue, which we assume to be the case. Stretches of the fibers in the diseased material are measured with respect to the evolving intermediate configuration and therefore do not increase monotonically, see Fig. 7. For a given time t , the collagen stretch is obtained by $\lambda^c(t) = \lambda^e(t)/r(t)$, where the evolution of the recruitment variable $r(t)$ is shown in Fig. 9. To this end, we like to recall equations (3.5) and (3.6). Also, note the change in scale from Figs. 7 to 8.

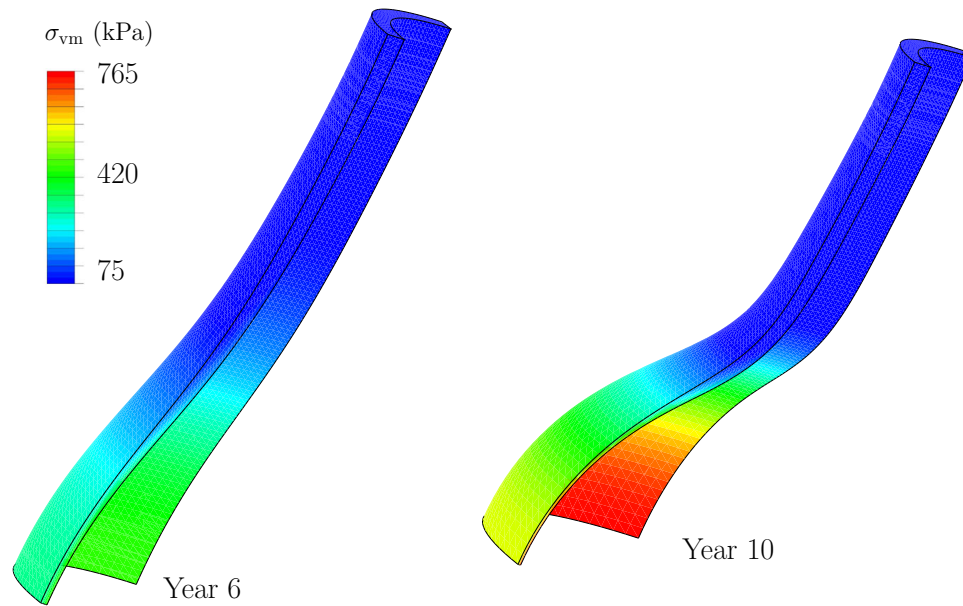


Fig. 10 The von Mises stress distribution on the inner and outer surfaces of a developing abdominal aortic aneurysm with a physiological pressure of 16 kPa (120 mmHg). The stress distributions on the inner and outer surfaces are uniform in the circumferential direction and varies radially and longitudinally. Images show results for years 6 and 10

In many previous papers, exemplified in [19,24,25,61–64], the von Mises stress has been used to characterize the stress distributions in the walls of AAAs, and here we also adopt this as our stress measure, which we denote by σ_{vm} , defined as $\sigma_{vm} = \sqrt{3\bar{\sigma} : \bar{\sigma}}/2$. Recall the deviatoric part of the Cauchy stress in (2.17). The pressure applied to the inner surface is uniform in the circumferential direction and constant longitudinally, and hence, the stress distribution depends on the radial and axial positions only. The wall stress distributions on the inner and outer surfaces of the aneurysmal wall are then visualized in Fig. 10. Six years into aneurysm formation, the von Mises stress varies in the range: $88 < \sigma_{vm} < 499$ kPa, and after 10 years, this increases to another range: $93 < \sigma_{vm} < 760$ kPa, with the upper limit now exceeding the tissue strength. The thinning of the arterial wall with bulge dilatation is clearly visible.

Two-dimensional wall mechanics to investigate aneurysm growth and remodeling is used, among others, in [28,32,34]. On the other hand, the current study solves the three-dimensional governing equations resulting in the shear distribution shown in Fig. 11. The images show a distribution that varies mainly along the axial direction, being zero in the healthy section of the tube. Six years into aneurysm formation, the shear stress varies in the range: $-43 < \tau_{rz} < 0.5$ kPa, and after 10 years, this variation changes to another range: $-135 < \tau_{rz} < 6.5$ kPa.

Figure 12 illustrates the changes of the circumferential Cauchy stress component over a 10-year period. The stress in the diseased tissue is again reported for the inner and outer surfaces at the location of maximum bulge dilatation and depicted by a solid and dashed lines, respectively. Not surprisingly, the circumferential stress is larger on the inner surface [65]. The response of the healthy section of the tube is recorded on the inner surface and shown by a dotted line. The magnitude reduces from 88.5 to 77.4 kPa over the 10-year period, which is attributed to the changes of the axial stretch generated by the expanding aneurysm.

In Fig. 13, the variation of the axial Cauchy stress component is illustrated with respect to time, t . For the diseased tissue, at the location of maximum bulge diameter, the values on the inner and outer surfaces are very similar and, as expected, much smaller compared to those of the circumferential component. The axial component on the inner surface of the healthy section changes from 33.8 kPa to 30.5 kPa over the reported period.

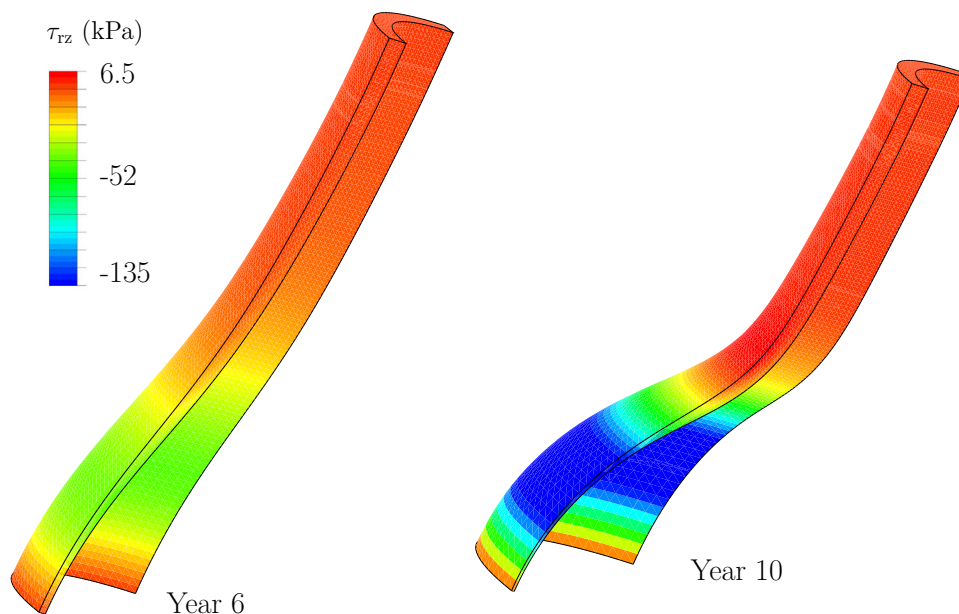


Fig. 11 Contour plot of the Cauchy stress component τ_{rz} on the inner and outer surfaces of a developing abdominal aortic aneurysm when a physiological pressure of 16 kPa (120 mmHg) is applied. Images show results for years 6 and 10

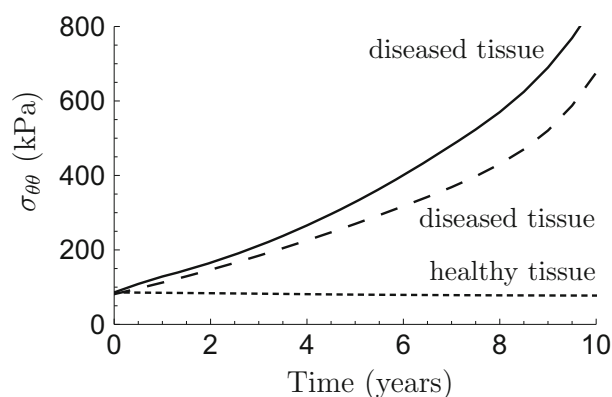


Fig. 12 The changes of the Cauchy stress component $\sigma_{\theta\theta}$ of healthy and diseased tissues over a 10-year period. The responses of the diseased tissue are evaluated at the inner and outer surfaces at the location of maximum bulge dilatation—shown by *solid* and *dashed lines*, respectively. The stress of the healthy tissue is evaluated, outside the damage zone specified in (6.29), on the inner surface

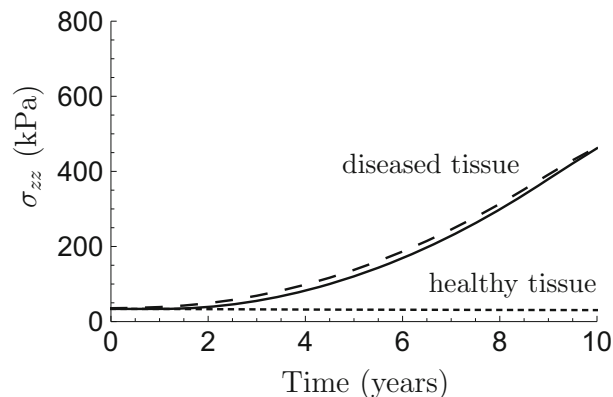


Fig. 13 The changes of the axial component of the Cauchy stress of healthy and diseased tissues. The responses of the diseased tissue are evaluated at the inner and outer surfaces at the location of maximum bulge dilatation—shown by *solid* and *dashed lines*, respectively. The stress of the healthy section is evaluated, outside the damage zone specified in (6.29), on the inner surface

7.4 Biaxial extension

Numerical results of equibiaxial extension of healthy and aneurysmal tissues are reported next. The properties of the healthy material are summarized in Tables 1 and 2. The properties of the aneurysmal tissue are taken from the finite element simulation at maximum bulge dilatation for $t = 10$ years. Specifically, the elastin content of the mixture reduces to $\rho_r^e(10) = 0.31\rho_r$, while the collagen content increases to $\rho_r^c(10) = 0.75\rho_r$, see Fig. 6. Also, due to bulge dilatation and fiber remodeling, the preferred directions change from the original $\pm 15^\circ$ to the current $\pm 9.6^\circ$. Figure 14 shows the circumferential and axial Cauchy stress components of the healthy material for $1 \leq \lambda \leq 1.1$. The behavior of aneurysmal tissue at $t = 10$ years is depicted in Fig. 15. The mechanical behavior

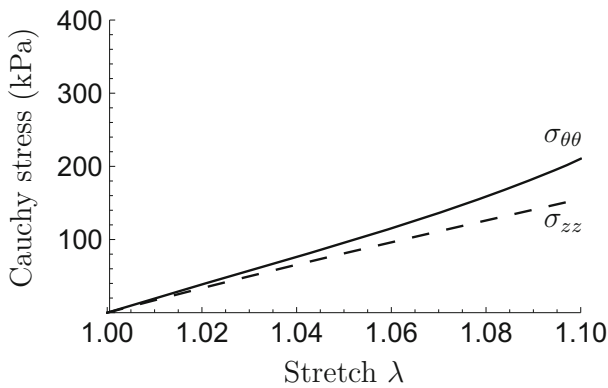


Fig. 14 The circumferential and axial Cauchy stress components of an aortic tissue in the homeostatic state during in-plane equibiaxial extension

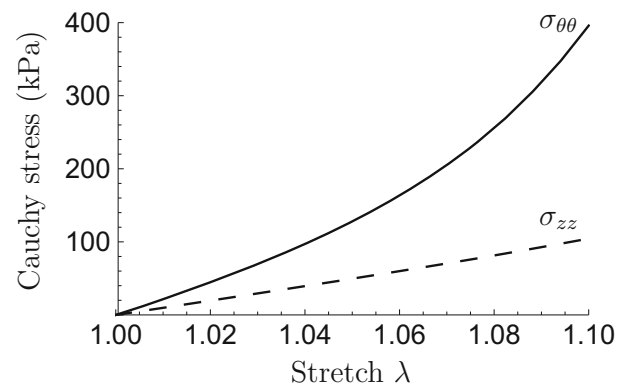


Fig. 15 The circumferential and axial Cauchy stress components during in-plane equibiaxial extension of an aneurysmal tissue. The material parameters are taken from the finite element simulation for $t = 10$ years at maximum bulge dilatation

of the aneurysmal tissue shows a significant degree of anisotropy and pronounced stretch-associated stiffening. As expected, it is stiffer compared with the material in the healthy state [6,66,67].

8 Concluding remarks

In this paper, a general three-dimensional formulation of the constrained mixture theory in the form developed by Humphrey and Rajagopal [30] has been applied to study the formation and dilatation of an abdominal aortic aneurysm. Axisymmetric deformations were considered for the homeostatic state, and for aneurysm development, therefore, only one eighth of the cylindrical geometry was considered. Without specialization of the constitutive formulation, general expressions have been derived, which quantify the processes of production and removal of constituents from the loaded configuration. The interaction between mechanical stretch and collagen, which leads to microstructures changes, is included in the model formulation.

The constitutive theory has then been specialized to a mixture of elastin and oriented collagen fibers, which endow the material with anisotropic properties. For numerical purposes, the energy function has been decomposed into isochoric and volumetric parts. This has then been particularized so that the isochoric part consists of a neo-Hookean term associated with the matrix material and two exponential terms accounting for the degree of anisotropy. The volumetric part consists of a penalty function to enforce the volumetric response during short-term events.

Results show that the mixture theory of growth and remodeling predicts the development of inhomogeneous mechanical properties and dilatation of the diseased section of the arterial wall. We found that the rate of expansion depends primarily on the rate of production and removal of elastin and collagen as well as on the change in microstructure. Specifically, the results show that aneurysm formation is accompanied by reduction of elastin and a gradual increase of collagen. The three-dimensional formulation adopted in this study allows evaluating, in addition to the in-plane stress components, the out-of-plane shear stress distribution within the arterial wall, which is not possible if two-dimensional wall mechanics is used.

It is, of course, a simplifying assumption that the axisymmetric shape is maintained during aneurysm expansion, an assumption that runs counter to the medical evidence. Also, by considering the aorta as an isolated system not in contact with surrounding tissues and organs, the results and findings are somewhat compromised. It is possible to account for these and other shortcomings; however, this leads to a much more complicated analysis.

Acknowledgements This work was supported by the National Science Foundation (Grant Nos. CMMI-1031366 and CMMI-1352955) and by an Innovates/Collaborates Award granted by the Tufts University.

References

1. Armentano R, Barra J, Levenson J, Simon A, Pichel R (1995) Arterial wall mechanics in conscious dogs: assessment of viscous, inertial and elastic moduli to characterize aortic wall behavior. *Circ Res* 76:468–478
2. Shadwick R (1999) Mechanical design in arteries. *J Exp Biol* 202:3305–3313
3. Raghavan ML, Webster M, Vorp DA (1999) Ex-vivo bio-mechanical behavior of AAA: assessment using a new mathematical model. *Ann Biomed Eng* 24:573–582
4. Sverdlik A, Lanir Y (2002) Time dependent mechanical behaviour of sheep digital tendons, including the effects of preconditioning. *J Biomech Eng* 124:78–84
5. Sacks MS (2003) Incorporation of experimentally derived fiber orientation into a structural constitutive model for planar collagenous tissues. *J Biomech Eng* 125:280–287
6. Pancheri FQ, Peattie RA, Reddy ND, Ahamed T, Lin W, Ouellette TD, Iafrati MD, Dorfmann L (2017) Histology and biaxial mechanical behavior of abdominal aortic aneurysm tissue samples. *J Biomech Eng* 139:031002
7. O’Leary SA, Healey DA, Kavanagh EG, Walsh MT, McGloughlin TM, Doyle BJ (2014) The biaxial biomechanical behavior of abdominal aortic aneurysm tissue. *Ann Biomed Eng* 42:2440–2450
8. Tong J, Cohnert T, Regitnig P, Holzapfel GA (2011) Effects of age on the elastic properties of the intraluminal thrombus and the thrombus-covered wall in abdominal aortic aneurysms: Biaxial extension behaviour and material modelling. *Eur J Vasc Endovasc Surg* 42:207–219
9. Humphrey JD (1999) Remodelling of a collagenous tissue at fixed lengths. *ASME J Biomech Eng* 121:591–597
10. Nissen R, Cardinale GJ, Udenfriend S (1978) Increased turnover of arterial collagen in hypertensive rats. *Proc Natl Acad Sci USA Med Sci* 75:451–453
11. He CM, Roach M (1993) The composition and mechanical properties of abdominal aortic aneurysms. *J Vasc Surg* 20:6–13
12. Cheheltani R, Pichamuthu JE, Rao J, Weinbaum JS, Kiani MF, Vorp DA, Pleshko N (2017) Fourier transform infrared spectroscopic imaging-derived collagen content and maturity correlates with stress in the aortic wall of abdominal aortic aneurysm patients. *Cardiovasc Eng Technol* 8:70–80
13. McGee GS, Baxter BT, Shively VP, Chisholm R, McCarthy WJ, Flinn WR, Yao JST, Pearce WH (1991) Aneurysm or occlusive disease-factors determining the clinical course of atherosclerosis of the infrarenal aorta. *Surgery* 110:370–376
14. Choke E, Cockerill G, Wilson WRW, Sayed S, Dawson J, Loftus I, Thompson MM (2005) A review of biological factors implicated in abdominal aortic aneurysm rupture. *Eur J Vasc Endovasc Surg* 30:227–244
15. Vorp DA (2007) Biomechanics of abdominal aortic aneurysm. *J Biomech* 40:1887–1902
16. Fillinger MF, Raghavan ML, Marra SP, Cronenwett JL, Kennedy FE (2002) In vivo analysis of mechanical wall stress and abdominal aortic aneurysm rupture risk. *J Vasc Surg* 36:589–597
17. Dorfmann A, Wilson C, Edgar ES, Peattie RA (2010) Evaluating patient-specific abdominal aortic aneurysm wall stress based on flow-induced loading. *Biomech Model Mechan* 9:127–139
18. Erhart P, Grond-Ginsbach C, Hakimi M, Lasitschka F, Dihlmann S, Böckler D, Alexander Hyhlik-Dürr A (2014) Finite element analysis of abdominal aortic aneurysms: predicted rupture risk correlates with aortic wall histology in individual patients. *J Endovasc Ther* 21:556–564
19. Ahamed T, Dorfmann L, Ogden RW (2016) Modelling of residually stressed materials with application to AAA. *J Mech Behav Biomed* 61:221–234
20. Rissland P, Alemu Y, Einav S, Ricotta J, Bluestein D (2009) Abdominal aortic aneurysm risk of rupture: patient-specific FSI simulations using anisotropic model. *ASME J Biomech Eng* 131:031001
21. Pierce DM, Fastl TE, Rodriguez-Vila B, Verbrughe P, Fournau I, Maleux G, Herijgers P, Gomez EJ, Holzapfel GA (2015) A method for incorporating three-dimensional residual stretches/stresses into patient-specific finite element simulations of arteries. *J Mech Behav Biomed Mater* 47:147–16
22. Joldes GR, Miller K, Wittek A, Doyle B (2016) A simple, effective and clinically applicable method to compute abdominal aortic aneurysm wall stress. *J Mech Behav Biomed Mater* 58:139–148
23. Eriksson T, Watton P, Luo X, Ventikos Y (2014) Modelling volumetric growth in a thick walled fibre reinforced artery. *J Mech Phys Solids* 73:134–150
24. Raghavan ML, Vorp DA (2000) Toward a biomechanical tool to evaluate rupture potential of abdominal aortic aneurysm: identification of a finite strain constitutive model and evaluation of its applicability. *J Biomech* 33:475–482
25. Maier A, Gee MW, Reeps C, Pongratz J, Eckstein HH, Wall WA (2010) A comparison of diameter, wall stress, and rupture potential index for abdominal aortic aneurysm rupture risk prediction. *Ann Biomed Eng* 38:3124–3134
26. Gasser T, Auer M, Labruto F, Swedenborg J, Roy J (2010) Biomechanical rupture risk assessment of abdominal aortic aneurysms: model complexity versus predictability of finite element simulations. *Eur J Vasc Endovasc* 40:176–185
27. Erhart P, Hyhlik-Dürr A, Geisbüsch P, Kotelis D, Müller-Eschner M, Gasser T, von Tengg- Kobligk H, Böckler D (2015) Finite element analysis in asymptomatic, symptomatic, and ruptured abdominal aortic aneurysms: in search of new rupture risk predictors. *Eur J Vasc Endovasc* 49:239–245

28. Watton PN, Hill NA, Heil M (2004) A mathematical model for the growth of the abdominal aortic aneurysm. *Biomech Model Mech* 3:98–113
29. Watton PN, Hill NA, Heil M (2009) Evolving mechanical properties of a model of abdominal aortic aneurysm. *Biomech Model Mech* 8:25–42
30. Humphrey JD, Rajagopal KR (2002) A constrained mixture model for growth and remodeling of soft tissues. *Math Models Methods Appl Sci* 12:407–430
31. Baek S, Rajagopal KR, Humphrey JD (2006) A theoretical model of enlarging intracranial fusiform aneurysms. *ASME J Biomech Eng* 128:142–149
32. Valentin A, Cardamone L, Baek S, Humphrey J (2009a) Complementary vasoactivity and matrix re-modelling in arterial adaptations to altered flow and pressure. *J R Soc Interface* 6:293–306
33. Valentin A, Humphrey J (2009b) Evaluation of fundamental hypotheses underlying constrained mixture models of arterial growth and remodelling. *Philos Trans R Soc A* 367:3585–3606
34. Wilson JS, Baek S, Humphrey JD (2013) Parametric study of effects of collagen turnover on the natural history of abdominal aortic aneurysms. *Proc R Soc A Math Phys Eng Sci* 469:20120556
35. Valentin A, Humphrey J, Holzapfel GA (2011) A multi-layered computational model of coupled elastin degradation, vasoactive dysfunction, and collagenous stiffening in aortic aging. *Ann Biomed Eng* 39:2027–2045
36. Valentin A, Humphrey J, Holzapfel GA (2013) A finite element-based constrained mixture implementation for arterial growth, remodeling, and adaptation: Theory and numerical verification. *Int J Numer Methods Biomed Eng* 29:822–849
37. Spencer AJM, Rivlin RS (1959) Finite integrity bases for five or fewer symmetric 3×3 matrices. *Arch Ration Mech Anal* 2:435–446
38. Spencer AJM (1971) Theory of invariants. In: Eringen AC (ed) *Continuum physics*, vol 1. Academic Press, New York, pp 239–353
39. Flory PJ (1961) Thermodynamic relations for highly elastic materials. *Trans Faraday Soc* 57:829–838
40. Ogden RW (1978) Nearly isochoric elastic deformations: application to rubberlike solids. *J Mech Phys Solids* 26:37–57
41. Demirkoparan H, Pence TJ, Wineman A (2009) On dissolution and reassembly of filamentary reinforcing networks in hyperelastic materials. *Proc R Soc A Math Phys Eng Sci* 465:867–894
42. Demirkoparan H, Pence TJ, Wineman A (2013) Chemomechanics and homeostasis in active strain stabilized hyperelastic fibrous microstructures. *Int J Nonlinear Mech* 56:86–93
43. Holzapfel GA, Gasser TC, Ogden RW (2000) A new constitutive framework for arterial wall mechanics and a comparative study of material models. *J Elasticity* 61:1–48
44. Wang N, Butler JP, Ingber DE (1993) Mechanotransduction across the cell-surface and through the cytoskeleton. *Science* 260:1124–1127
45. Tözeren A, Skalak R (1988) Interaction of stress and growth in a fibrous tissue. *J Theor Biol* 130:337–350
46. Kroon M, Holzapfel GA (2007) A model of saccular cerebral aneurysm growth by collagen fiber remodeling. *J Theor Biol* 247:775–787
47. Kroon M, Holzapfel GA (2008) Modeling of saccular aneurysm growth in a human middle cerebral artery. *ASME J Biomech Eng* 130:051012
48. Rajagopal K, Wineman A (1992) A constitutive equation for nonlinear solids which undergo deformation induced microstructural changes. *Int J Plasticity* 8:385–395
49. Rodriguez EK, Hoger A, McCulloch AD (1994) Stress-dependent finite growth in soft elastic tissues. *J Biomech* 27:455–67
50. Cyron CJ, Humphrey JD (2017) Growth and remodeling of load-bearing biological soft tissues. *Meccanica* 52:645–664
51. Rezakhanlou R, Agianniotis A, Schrauwen JTC, Griffa A, Sage D, Bouten CVC, van de Vosse FN, Unser M, Stergiopoulos N (2012) Experimental investigation of collagen waviness and orientation in the arterial adventitia using confocal laser scanning microscopy. *Biomech Model Mech* 11:461–473
52. Frank C, Shrive N, Hiraoka H, Nakamura N, Kaneda Y, Hart D (1999) Optimisation of the biology of soft tissue repair. *J Sci Med Sport* 2:190–210
53. Gurtner GC, Werner S, Barrandon Y, Longaker MT (2008) Wound repair and regeneration. *Nature* 453:314–321
54. Adler JH, Dorfmann L, Han D, MacLachlan S, Paetsch C (2014) Mathematical and computational models of incompressible materials subject to shear. *IMA J Appl Math* 79:889–914
55. Braeu FA, Seitz A, Aydin RC, Cyron CJ (2016) Homogenized constrained mixture models for anisotropic volumetric growth and remodeling. *Biomech Model Mech* 16(3):889–906
56. Cyron CJ, Wilson JS, Humphrey JD (2014) Mechanobiological stability: a new paradigm to understand the enlargement of aneurysms? *J R Soc Interface* 11:20140680
57. Cyron CJ, Humphrey JD (2014) Vascular homeostasis and the concept of mechanobiological stability. *Int J Eng Sci* 85:203–223
58. Wilson JS, Baek S, Humphrey JD (2012) Importance of initial aortic properties on the evolving regional anisotropy, stiffness and wall thickness of human abdominal aortic aneurysms. *J R Soc Interface* 9:2047–2058
59. Pancheri FQ (2014) Experimental and analytical aspects of biological and engineering materials subject to planar biaxial loading. PhD Thesis, Tufts University
60. Langille BL (1995) Blood flow-induced remodeling of the artery wall. In: Bevan JA, Kaley G, Rubanyi GM (eds) *Flow-dependent regulation of vascular function*. Springer, New York
61. Raghavan ML, Vorp DA, Federle M, Makaroun MS, Webster MW (2000) Wall stress distribution on three-dimensionally reconstructed models of human abdominal aortic aneurysm. *J Vasc Surg* 31:760–769

62. Wang DHJ, Makaroun MS, Webster MW, Vorp DA (2002) Effect of intraluminal thrombus on wall stress in patient-specific models of abdominal aortic aneurysm. *J Vasc Surg* 36:598–604
63. Lu J, Zhou X, Raghavan ML (2007) Inverse elastostatic stress analysis in pre-deformed biological structures: demonstration using abdominal aortic aneurysms. *J Biomech* 40:693–696
64. Scotti CM, Jimenez J, Muluk SC, Finol EA (2008) Wall stress and flow dynamics in abdominal aortic aneurysms: finite element analysis vs. fluid–structure interaction. *Comput Methods Biomech Biomed Eng* 11:301–322
65. Ogden RW (1997) *Non-linear elastic deformations*. Dover, Mineola
66. Vande Geest JP, Sacks MS, Vorp DA (2006) The effects of aneurysm on the biaxial mechanical behavior of human abdominal aorta. *J Biomech* 39:1324–1334
67. Pancheri FQ, Eng CM, Lieberman DE, Biewener AA, Dorfmann L (2014) A constitutive description of the anisotropic response of the fascia lata. *J Mech Behav Biomed* 30:306–323

C Appendix C

Histology and biaxial mechanical behavior of abdominal aortic aneurysm tissue sam- ples

Reference

Francesco Q. Pancheri, Robert A. Peattie, Nithin D. Reddy,
Touhid Ahamed, Wenjian Lin, Timothy D. Ouellette, Mark D. Iafrati,
Luis Dorfmann

Francesco Q. Pancheri

Department of Mechanical Engineering,
Tufts University,
Medford, MA 02155

Robert A. Peattie¹

Department of Surgery,
Tufts Medical Center,
Boston, MA 02111
e-mail: robert.peattie@tufts.edu

Nithin D. Reddy

Department of Surgery,
Tufts Medical Center,
Boston, MA 02111

Touhid Ahamed

Department of Civil and
Environmental Engineering,
Tufts University,
Medford, MA 02155

Wenjian Lin

Department of Civil and
Environmental Engineering,
Tufts University,
Medford, MA 02155

Timothy D. Ouellette

Department of Surgery,
Tufts Medical Center,
Boston, MA 02111

Mark D. Iafrati

Department of Surgery,
Tufts Medical Center,
Boston, MA 02111

A. Luis Dorfmann

Department of Civil and
Environmental Engineering,
Tufts University,
Medford, MA 02155;
Department of Biomedical Engineering,
Tufts University,
Medford, MA 02155

Histology and Biaxial Mechanical Behavior of Abdominal Aortic Aneurysm Tissue Samples

Abdominal aortic aneurysms (AAAs) represent permanent, localized dilations of the abdominal aorta that can be life-threatening if progressing to rupture. Evaluation of risk of rupture depends on understanding the mechanical behavior of patient AAA walls. In this project, a series of patient AAA wall tissue samples have been evaluated through a combined anamnestic, mechanical, and histopathologic approach. Mechanical properties of the samples have been characterized using a novel, strain-controlled, planar biaxial testing protocol emulating the in vivo deformation of the aorta. Histologically, the tissue ultrastructure was highly disrupted. All samples showed pronounced mechanical stiffening with stretch and were notably anisotropic, with greater stiffness in the circumferential than the axial direction. However, there were significant intrapatient variations in wall stiffness and stress. In biaxial tests in which the longitudinal stretch was held constant at 1.1 as the circumferential stretch was extended to 1.1, the maximum average circumferential stress was 330 ± 70 kPa, while the maximum average axial stress was 190 ± 30 kPa. A constitutive model considering the wall as anisotropic with two preferred directions fit the measured data well. No statistically significant differences in tissue mechanical properties were found based on patient gender, age, maximum bulge diameter, height, weight, body mass index, or smoking history. Although a larger patient cohort is merited to confirm these conclusions, the project provides new insight into the relationships between patient natural history, histopathology, and mechanical behavior that may be useful in the development of accurate methods for rupture risk evaluation. [DOI: 10.1115/1.4035261]

Keywords: aortic aneurysm, tissue, histology, collagen, mechanical properties

1 Introduction

Abdominal aortic aneurysms (AAAs) are degenerative, localized dilations of the abdominal aorta that can potentially be life-threatening if progressing to rupture. AAAs have been estimated to occur in as much as 2–3% of the population [1,2], with approximately 150,000 new cases diagnosed each year [3]. The mortality rate on rupture is between 78% and 94% [4,5], and ruptured AAA is responsible for 14,000 deaths annually in the U.S. alone [6]. At present, clinical treatment decisions are determined based on the size and growth rate of the lesion. A 5.5 cm diameter lesion in men and 5.0 cm in women are considered the critical size beyond which risk of rupture is unacceptably high, and therefore surgical management is indicated [1,6–9]. Elective treatment is also

suggested if maximum diameter increases at a rate larger than 0.5–1.0 cm per year [7,10]. However, despite a long history of research into the formation, growth, and mechanical properties of AAA, there is still no clinical system capable of accurately predicting the risk of rupture on a patient-specific basis. Additionally, it has been suggested by several authors that from a fundamental biomechanical perspective, peak wall stress and strength may be better predictors of aneurysm rupture than maximum diameter [11–16]. As a result, there is a critical need to implement a patient-specific program capable of accurately assessing rupture risk based on aneurysm pathophysiological characteristics.

To support the evaluation of wall stress and rupture risk, an extensive literature has developed in recent years characterizing the histology, pathology, material properties, and mechanical behavior of AAA wall tissue. A general consensus has emerged associating the presence of AAA with an overall disorganization of elastin and collagen in the diseased vessel wall, combined with a net decrease in smooth muscle cell density [17–20]. However,

¹Corresponding author.

Manuscript received December 16, 2015; final manuscript received November 1, 2016; published online January 23, 2017. Assoc. Editor: Jonathan Vande Geest.

the specific reorganization of wall ultrastructural components is not yet clear. Although He and Roach [19] reported collagen and ground matrix volume fractions to increase within AAAs, others have reported collagen levels to remain unchanged [21] and also decrease [18,22]. Further, the presence and extent of hard calcifications, atheroma, and thrombus can vary widely between patients [23,24].

Even if a constitutive model was able to describe the general behavior of the tissue response, it would not capture the full extent of the ultrastructural heterogeneity among different samples. Instead, attention has focused on creating a biomechanically based approach to assess rupture risk for specific patients through evaluation of AAA material characteristics. He and Roach [19] conducted uniaxial tension tests on human abdominal aortic tissue samples and correlated the test results with tissue histology. However, more recent data from load or displacement controlled biaxial testing of AAA specimens have found the tissue to show moderately anisotropic behavior [14,25–27]. Biaxial material property measurements have been compared with patient age and gender [27] and have been used to calibrate computational models [14,25,26]. Planar biaxial tests approximating strain magnitudes to which the tissue is exposed during the cardiac cycle offer the advantage of producing states of deformation more closely resembling in vivo conditions of the artery than uniaxial protocols. In addition, biaxial measurements can highlight the anisotropic characteristics of biological materials to a higher extent than uniaxial tests, thus helping to capture material directional coupling. From a mechanical–structural point of view, tissue anisotropy is the characteristic feature of AAAs. Further, aneurysmal wall anisotropy has been shown to change on a patient to patient basis, and to be greater in diseased or older individuals than in samples from young healthy individuals [25,28].

Unfortunately, none of these tests have been carried out under true strain-controlled conditions realistically emulating in vivo stress–stretch behavior. In addition, biaxial measurements of AAA tissue sample mechanical properties have not yet been compared with tissue histology. As a result, there remains a need for a combined histologic and strain-controlled biaxial mechanical characterization of AAA tissue. Most importantly, endovascular surgical repair (EVAR) is increasingly becoming the clinical treatment of choice even for small AAAs. Since tissue samples are not presently retrievable during an EVAR procedure, opportunities to harvest tissue samples for experimental study are becoming increasingly rare. It is therefore important to characterize as many tissue samples as possible, while the tissue can still be obtained. Here, we present results from a study addressing these needs. The biaxial mechanical properties of AAA tissue samples have been evaluated under true strain-controlled conditions emulating in vivo strains during the cardiac cycle and fit with a mathematical model based on wall matrix and fiber distributions. Measured properties have been correlated with the natural history of the patients from whom the tissue samples were obtained, as well as with histologic characterization of the wall ultrastructure.

2 Methods

All procedures were carried out with the full approval of the Tufts University and Medical Center Institutional Review Board. De-identified patient natural history anamnesis data were obtained from Tufts Medical Center records.

2.1 Specimen Preparation. Full thickness tissue samples approximately 35 mm long and 25 mm wide (Fig. 1(a)) were obtained intra-operatively from patients undergoing elective open-abdomen aortic aneurysm repair at the Tufts Medical Center. Prior to resection, the longitudinal direction of each sample was marked with a suture. Samples were immersed in isotonic saline, then placed on ice but not frozen. They were immediately transported to the Tufts University Mechanics of Soft Materials

laboratory, and material property testing was completed on them normally within 8 h of resection. Before preparation for testing, the presence and extent of hard calcifications, lipids, and thrombus on and within the samples were quantified by visual inspection, using a 4 point scale in which 4 represents near complete coverage of constituents, 3 represents extensive but not complete coverage, 2 represents moderate coverage, 1 represents limited coverage, and 0 no noticeable deposits. (For example, Fig. 1(a) shows a specimen scored 3 for atheroma, 2 for calcifications, and 1 for thrombus.)

Cruciform sections suitable for biaxial testing [29,30] were cut from the original specimens using a custom-designed tracing die, keeping one axis of the section along the aorta longitudinal direction and the orthogonal axis in the circumferential direction. Four gage marks were attached in the section center to define a 7 mm × 7 mm square gage region (Fig. 1(b)) in which strain was tracked. Specimen thickness was measured using a contact micrometer with ±0.01 mm resolution (Mitutoyo Corp., pocket thickness gage) at several portions within this gage region, using the minimum pressure needed to contact the tissue surface but not deform it. However, to avoid the possibility of compression by the micrometer, sample width was determined by a pixel count method using the image captured from the testing machine's fixed focal length video extensometer in conjunction with the publicly available software IMAGEJ (NIH), taking care to keep the samples flat and unfolded. Spatial resolution was 45.6 μm/pixel.

2.2 Histology. When possible, portions of the tissue cut off to form the cruciform-shaped specimen were labeled and fixed in 4% buffered formaldehyde solution (pH 7.4), then embedded in paraffin, and sectioned at 5 μm intervals. To assess different tissue characteristics, consecutive histologic sections were stained with either hematoxylin and eosin (H&E), elastica van Gieson (EvG), Masson's trichrome (TRI), or antismooth muscle actin (SMA). Qualitative and quantitative observations of the cell and fiber distributions in the tissue ultrastructure were made using a light microscope (Olympus BX40, Olympus Corporation of the Americas, Center Valley, PA). Digital image collection was performed with the microscope's integrated camera (SPOT Insight 2, Diagnostic Instruments, Inc., Sterling Heights, MI) controlled by SPOT BASIC software (Diagnostic Instruments, Inc., Sterling Heights, MI). Both the total tissue area and the area fraction of coverage of each stain were evaluated quantitatively at 100× magnification using a series of SPOT and IMAGEJ tools (*Match Color* to set the background area of the image to zero color saturation so that total area could be determined, *Threshold Color* to gate for hue and saturation values of specific colors and separate the background from the area of interest, and *Analyze Particles* to measure the area of interest). Percent area was defined as the ratio of the area of interest to the total area of tissue coverage (percent area error 0.2%). Between 20 and 40 individual images depending on the size of the tissue section were analyzed in this way for each stain, for each patient, and mean and standard deviation area fraction of coverage were calculated.

2.3 Test Apparatus. Mechanical properties of the tissue samples were evaluated using a custom-designed, planar biaxial tension tester (Zwick-Roell, Inc., Ulm, Germany), under strain control (Fig. 1(c)). The characteristics and layout of this apparatus have been documented previously [31]. Briefly, it includes four horizontally opposing independently controlled linear actuators (Zwick/Roell Z2.0), with dedicated load cells and computer. Gage marks are tracked by a video extensometer that also provides the feedback loop controlling both deformation and strain rate by independently regulating the signal used to drive each of the actuators. As a result, measured load, time, and actuator position are all functions of the independently controlled deformation.

Tissue samples were held in the tester by four custom C-shaped grips designed to position the sample within a constant

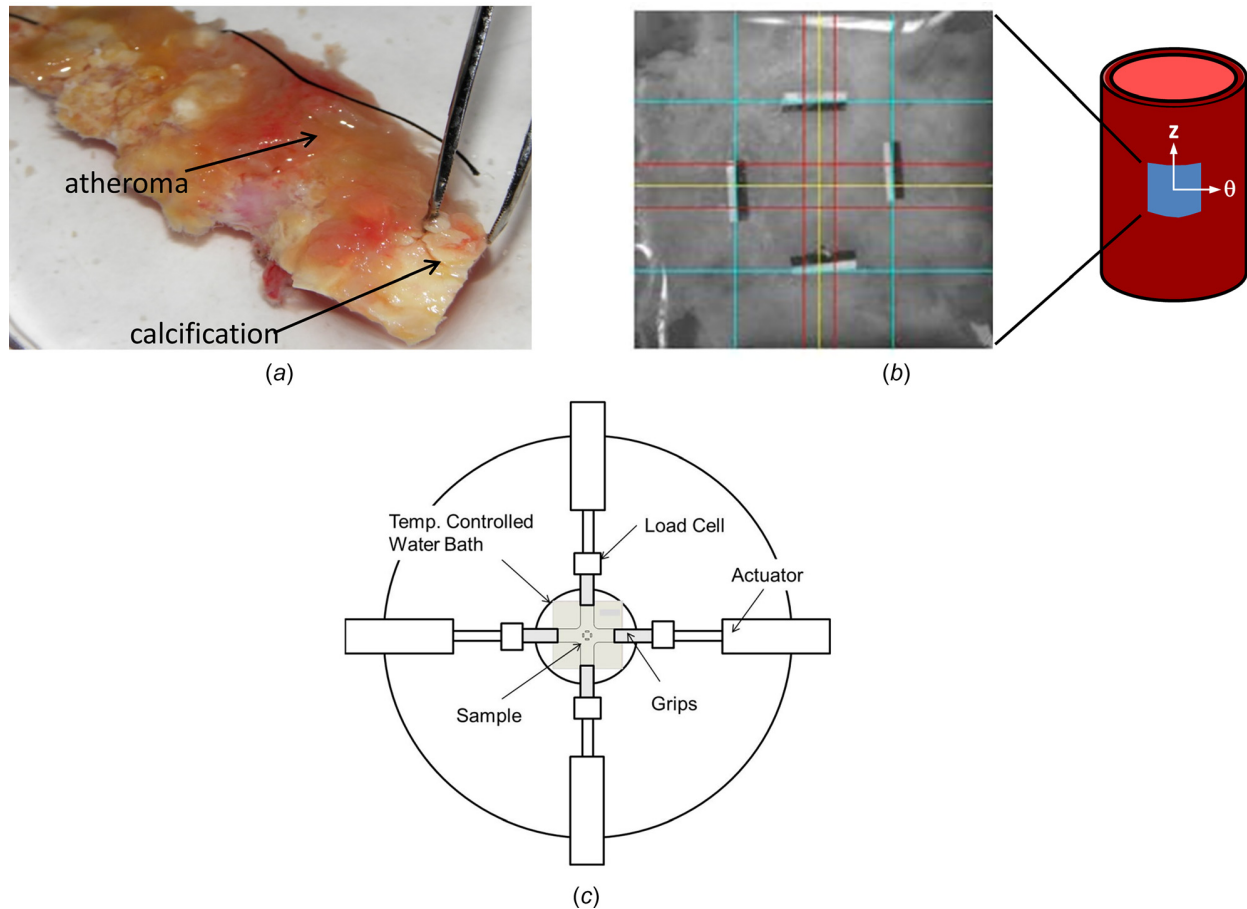


Fig. 1 (a) AAA tissue sample as received. Severe polymorphous atherosclerotic plaque with precipitated calcium agglomerates is clearly apparent. (b) Tissue specimen undergoing planar biaxial tension. Digital gage marks track the movement of the physical markers. The circumferential and longitudinal directions of the sample relative to the aorta are shown on the right. (c) Schematic diagram of the biaxial test apparatus, showing the sample, water bath, grips, actuator arms, and load cells. Not shown is the video extensometer directly above the specimen used to measure and control deformation in the gage region.

temperature bath filled with isotonic phosphate buffered saline (PBS). The temperature of the bath was controlled by an autoregulated circulator (Ecoline Type RE 104; LAUDA Königshofen, Germany), and all tests were carried out at 37 °C.

2.4 Test Protocol. Tissue samples were tested using a biaxial protocol emulating the in vivo deformations of the abdominal aorta during the cardiac cycle [32,33]. The stretch ratio λ was

computed as l/L , where l and L denote the measured gage lengths in the deformed and reference configurations, respectively, with the reference configuration taken as the position of the gage marks when 0.05 N preload was detected by all four load cells, which was determined at the beginning of each test sequence.

A series of four tests were performed, although not all samples completed all tests due to the tissue condition. In each test, while the tissue was extending and contracting, loads in the axial and circumferential directions were continuously measured by 500 N

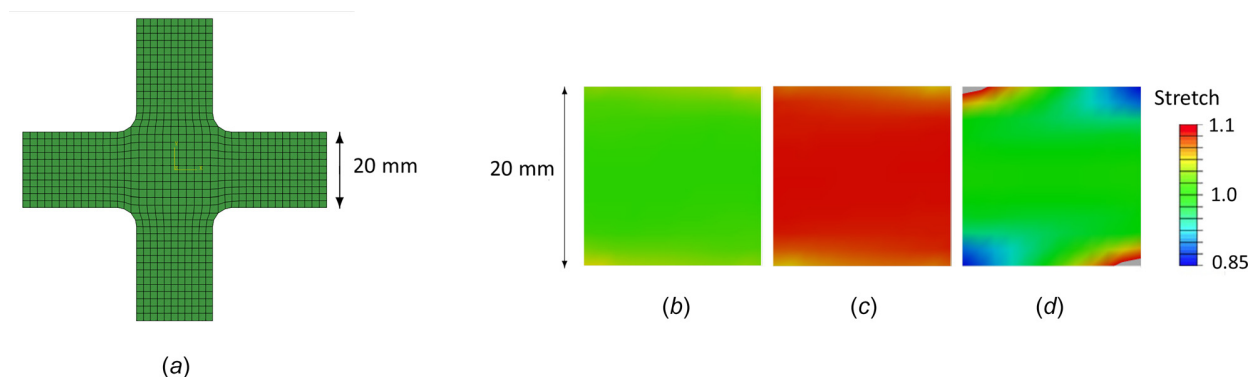


Fig. 2 Finite element calculation. (a) Mesh used to evaluate the deformation field in the gage region of the cruciform-shaped sample, with length scale. (b)–(d) Contour plots showing homogeneity of the deformation field, (b) axial stretch distribution, (c) circumferential stretch distribution, and (d) shear distribution.

Table 1 Model parameter values providing a best fit to the patient group-mean measurements. Goodness-of-fit was greater than 0.98 for all but two of the curves.

μ_{iso} (kPa)	α	μ_{fib} (kPa)	k	ϕ (deg)
46.987	21.071	33.922	37.287	6.745

load cells accurate to ± 10 mN (Zwick/Roell B8122.10.01), and gage mark positions were monitored through the video extensometer. In the first test, axial stretch, λ_z , was fixed at 1.0, while circumferential stretch, λ_θ , underwent a set of extension–retraction cycles to a maximum of 1.1. In the second test, λ_z was fixed at 1.1, while λ_θ was again cycled to a maximum of 1.1. The third test was an equibiaxial deformation in which both λ_z and λ_θ were cycled simultaneously to 1.1, while in the fourth test, λ_z was again fixed at 1.0, while λ_θ was cycled to a maximum of 1.15. Five loading–unloading cycles were carried out in every test, with the first four cycles serving as preconditioning. Only data from the fifth cycle were used for further analysis. All tests were carried out at a fixed strain rate of 0.0035 s^{-1} . Tissue samples were photographed repeatedly during extension and if possible, while failing.

2.5 Finite Element Analysis. To verify that the deformation in the gage region was homogeneous when tissue samples were subjected to biaxial extension, a finite element analysis was performed using the commercial finite element package Abaqus (Dassault Systèmes, Inc., Waltham, MA, 2013) [34]. A finite element mesh was generated in the cruciform shape (Fig. 2(a)), assuming a thickness of 2 mm. A displacement boundary condition was applied at the edges of the cruciform-shaped model. The resulting deformation field throughout the cruciform shape was determined using the constitutive equation described below, with the material model parameters listed in Table 1.

2.6 Data Analysis. The circumferential and axial components of measured nominal stress, $P_{\theta\theta}$ and P_{zz} , were calculated as

$$P_{\theta\theta} = \frac{f_\theta}{A_\theta}, \quad P_{zz} = \frac{f_z}{A_z} \quad (1)$$

where f_θ and f_z represent the forces measured in the circumferential and axial directions, and A_θ and A_z are the corresponding

reference cross-sectional areas, given by $A_\theta = HL_z$ and $A_z = HL_\theta$, with H the mean thickness of the central region and L_θ , L_z the corresponding in-plane dimensions.

For each test, the fifth loading–unloading cycle of each sample was used to calculate the peak stress value, the percent energy dissipated, and the maximum elastic modulus (MEM) (stiffness) during loading. Specifically, the elastic modulus is a deformation-dependent measure that connects an increment of nominal stress to a corresponding increment of deformation. The values reported here are specific to the testing protocol and, by definition, depend on the stretch in the axial and circumferential directions. Mean and standard deviations of the stress–stretch response and elastic moduli were calculated by averaging over all the patient samples completing that test using only the loading portion of the test. To evaluate tissue anisotropy, the maximum elastic modulus (MEM) was calculated by fitting a series of straight line segments, each 2% of the maximum stretch, by least squares regression to the stress–deformation data. MEM was determined from the fitted segment for which the slope was a maximum, and the goodness-of-fit, R^2 , was greater than 0.97. Material anisotropy was evaluated by comparison of the maximum elastic moduli of the stress–stretch curves in the circumferential and longitudinal directions, using an independent t -test. Independent t -tests were also used to evaluate differences in tissue sample properties as a function of patient anamnesis properties. For all statistical analyses, significance was taken at the level $p \leq 0.05$. All analyses were carried out using MATLAB (MathWorks, Inc., Natick, MA).

2.7 Constitutive Modeling. The measured data were fit with a constitutive model based on Refs. [35] and [36]. AAA wall tissue was assumed to be homogeneous, incompressible, and hyperelastic, and to consist of an isotropic base matrix the wall was assumed to consist of an isotropic base matrix with distributed collagen fibers providing two preferred directions. Under those assumptions, the mechanical response of the material is given by a strain energy function, W , depending only on the deformation gradient tensor \mathbf{F} , i.e., $W = W(\mathbf{F})$. The nominal, \mathbf{P} , and Cauchy, $\boldsymbol{\sigma}$, stress tensors are then given by

$$\mathbf{P} = \frac{\partial W}{\partial \mathbf{F}} - p\mathbf{F}^{-1}, \quad \boldsymbol{\sigma} = \mathbf{F} \frac{\partial W}{\partial \mathbf{F}} - p\mathbf{I} \quad (2)$$

where p is an arbitrary scalar determined from the equilibrium equations and the boundary conditions [37], and \mathbf{I} is the identity

Table 2 Patient anamnesis and sample characteristics (NA = not available)

Characteristics	Patient 1	Patient 2	Patient 3	Patient 4	Patient 5	Patient 6	Patient 7	Patient 8	Patient 9	Patient 10	Patient 11	Patient 12	Patient 13	Mean \pm SD
Age (yr)	73	66	71	74	78	58	75	75	66	73	86	67	77	72.2 \pm 6.9
Gender	F	M	M	M	M	M	F	F	M	M	M	M	F	
Height (cm)	165	185	173	172	170	175	155	168	170	160	178	177	170	170.6 \pm 6.9
Weight (kg)	62	143	84	78	68	90	61	60	107	60	69	102	70	81.1 \pm 24.4
Maximum bulge diameter, D (mm)	55	56	40	82	72	80	57.4	58	90	55	72	55	55	63.6 \pm 14.2
Nondilated aorta diameter, d (mm)	22.8	26.0	NA	NA	30.0	NA	19.7	19.5	20.8	26.2	22.2	22.0	26.0	23.5 \pm 3.4
Wall thickness, H (mm)	1.84	2.24	1.35	3.10	1.75	3.21	1.35	1.28	2.15	4.35	1.11	3.34	2.37	2.34 \pm 0.9
Bulge diam/wall thickness, D/H	27.8	23.0	27.6	24.4	39.2	23.0	40.6	43.4	39.8	12.6	62.8	14.4	21.2	30.8 \pm 14.1
Htn > 140 mm Hg	Yes	Yes	Yes	Yes	Yes	No	Yes	Yes	No	No	Yes	Yes	No	
Smoking history	Prev.	Prev.	Curr.	Curr.	Prev.	Curr.	Curr.	Prev.	Prev.	Prev.	No	Curr.	Prev.	
Family history	Yes	No	No	No	No									
Diabetes	No	Type 2	No	Type 1	No	No								
Aortic surgery	No	Endo	No	Heart	No	No								
Calcification	4	3	1	0	1	0	0	1	2	0	1	1	0	1.1 \pm 1.3
Lipid deposit	4	1	2	2	2	3	4	1	3	1	3	1	0	2.1 \pm 1.3
Thrombus deposit	1	0	0	4	3	1	2	1	1	0	2	2	2	1.5 \pm 1.2

tensor. Following Ref. [36], the base matrix has strain energy, W_{iso} , given by

$$W_{\text{iso}} = \frac{\mu_{\text{iso}}}{2\alpha} \left\{ \exp[\alpha(I_1 - 3)] - 1 \right\} \quad (3)$$

where μ_{iso} represents the shear stiffness of the matrix in the reference configuration, α is a dimensionless material parameter, and I_1 is the first invariant of the right Cauchy–Green deformation tensor, \mathbf{C} , given by $\mathbf{C} = \mathbf{F}^T \mathbf{F}$, with $I_1 = \text{tr } \mathbf{C}$. Strain energy associated with the preferred directions, W_{fib} , is given by

$$W_{\text{fib}} = \frac{\mu_{\text{fib}}}{2k} \left\{ \exp[k(I_4 - 1)^2] - 1 \right\} + \frac{\mu_{\text{fib}}}{2k} \left\{ \exp[k(I_6 - 1)^2] - 1 \right\} \quad (4)$$

where μ_{fib} describes the degree of anisotropy, k is a dimensionless parameter associated with the preferred directions, and I_4 and I_6 are given by $I_4 = \mathbf{M} \cdot (\mathbf{C}\mathbf{M})$ and $I_6 = \mathbf{M}' \cdot (\mathbf{C}\mathbf{M}')$, where the unit vectors \mathbf{M} and \mathbf{M}' denote the preferred directions in the reference configuration, which are given by

$$\mathbf{M} = \cos \phi \mathbf{e}_\theta + \sin \phi \mathbf{e}_z, \quad \mathbf{M}' = \cos \phi \mathbf{e}_\theta - \sin \phi \mathbf{e}_z \quad (5)$$

where ϕ is the angle between the preferred directions and the circumferential direction, and \mathbf{e}_θ , \mathbf{e}_z are unit vectors in the circumferential and axial directions, respectively. It can be shown [38,39] that with this approach, the in-plane Cauchy stress components take the form

$$\sigma_{\theta\theta} = \mu_{\text{iso}}(\lambda_\theta^2 - \lambda_\theta^{-2}\lambda_z^{-2}) \exp[\alpha(I_1 - 3)] + 4\mu_{\text{fib}}\lambda_\theta^2 \cos^2 \phi (I_4 - 1) \exp[k(I_4 - 1)^2] \quad (6)$$

and

$$\sigma_{zz} = \mu_{\text{iso}}(\lambda_z^2 - \lambda_\theta^{-2}\lambda_z^{-2}) \exp[\alpha(I_1 - 3)] + 4\mu_{\text{fib}}\lambda_z^2 \sin^2 \phi (I_6 - 1) \exp[k(I_6 - 1)^2] \quad (7)$$

For an incompressible material, the nominal and Cauchy stress tensors are related by $\mathbf{P} = \mathbf{F}^{-1}\boldsymbol{\sigma}$. Since the deformations imposed here were planar biaxial extensions, \mathbf{F} becomes diagonal, and the analytically determined nominal stress components are

$$P_{\theta\theta} = \frac{\sigma_{\theta\theta}}{\lambda_\theta}, \quad P_{zz} = \frac{\sigma_{zz}}{\lambda_z} \quad (8)$$

Values of μ_{iso} , μ_{fib} , α , k , and ϕ providing the best fit of the model circumferential and axial stresses to the measured data were determined by the nonlinear, iterative algorithm for parameter estimation proposed by Buzzi-Ferraris and Manenti [40], using only the first three tests due to accumulated tissue damage by the fourth test. The closeness of the resulting fitted curves to the data was evaluated with the MATLAB *Goodness-of-fit* tool.

3 Results

3.1 Patient Clinical Traits and Specimen Characteristics.

Mechanical and histologic properties of 13 patient AAA wall tissue samples resected from the bulge anterior side during elective surgical repair were evaluated. Anamnesis data for the patients are summarized in Table 2, including age and gender, AAA bulge maximum diameter D , nondilated abdominal aorta diameter near the most inferior renal artery d , specimen wall thickness, and ratio of inner bulge diameter to wall thickness, D/H . Contributing factors such as presence or absence of hypertension (Htn), smoking, diabetes, and family history are also given, along with scores for

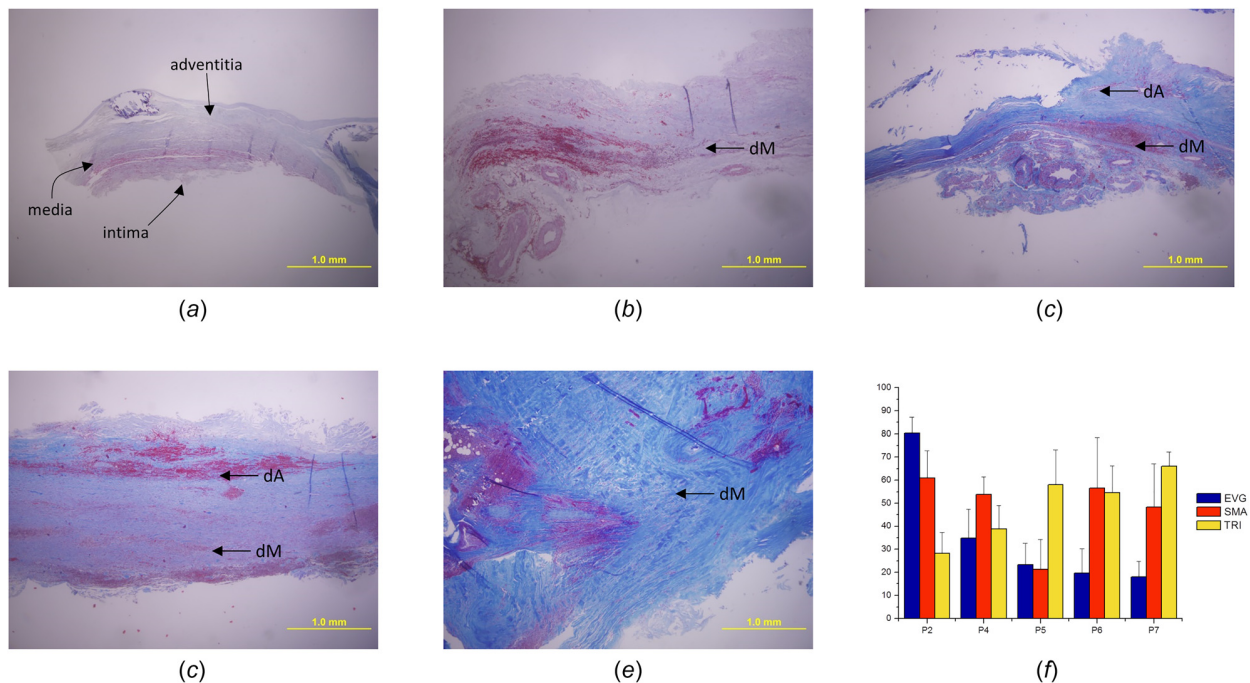


Fig. 3 Representative histologic images characterizing the wall ultrastructure, 40 \times magnification, Masson's trichrome stain. Blue—collagen; red—smooth muscle and extravasated cells. All images oriented with the tunica intima facing down. (a) Patient 2, (b) patient 4, (c) patient 5, (d) patient 6, and (e) patient 7. (f) Fractional area of coverage for EvG (highlighting elastin fibers), TRI (highlighting collagen fibers), or anti-SMA (highlighting smooth muscle). dM—disrupted tunica media and dA—disrupted tunica adventitia.

the presence and extent of hard calcifications, lipids, and thrombus on and within the samples.

Four of the patients were female, nine were male. Patient age ranged from 58 to 86, with a mean of 72.2 ± 6.9 . Maximum bulge diameter varied from 40 to 90 mm, with a mean of 63.6 ± 14.2 mm. Thickness of the samples varied from 1.28 to 4.35 mm, with a mean of 2.34 ± 0.9 mm. Nine of the 13 patients showed marked hypertension (greater than 140 mm Hg), four did not. Most strikingly, all but one of the patients had a past or current history of smoking.

3.2 Tissue Histology. Wall ultrastructure varied significantly between patients (Fig. 3, which shows representative images stained with trichrome). A small number of wall samples showed an organized distribution of layers within the wall, with recognizable intima, media, and adventitia (Fig. 3(a)). However, the ultrastructure of most samples lacked the well-organized layers normally associated with healthy aorta walls [41] and varied widely from patient to patient (Figs. 3(b)–3(e)). In these samples, wall layers were generally highly disorganized, tortuous, and fragmented. The media and adventitia, to the extent they could be recognized, were densely invested with numerous fibroblasts along with extravasated red cells, granular and agranular leukocytes, and other inflammatory cell types. Some of these samples showed regions of well-ordered tissue in some locations, but none was

well organized throughout. Most contained regions of highly disorganized structure interspersed with regions of increased collagen or elastin concentrations. In addition, most tissue samples showed intramural empty spaces that were lined by large quantities of cell types not associated with healthy aorta wall tissue, presumably inflammatory cells. Significant loss of parietal structural architecture and disruption of smooth muscle was common (Figs. 3(b)–3(e)).

EvG coverage varied from as little as 18% (Fig. 3(f), patient 7) to as much as 80% (patient 2). Trichrome coverage varied from 28% to 66%, and SMA coverage varied from 21% to 61%. In addition, the ratios of coverage between stains for each patient also varied extensively. Patient 2 showed nearly three-fold the coverage of EvG as trichrome (80% versus 28%), indicating a widespread distribution of elastin fibers but only limited collagen. In contrast, patients 5, 6, and 7 showed limited EvG coverage (18% for patient 7) but much greater trichrome coverage (66% for patient 7), indicating much more widely distributed collagen than elastin in the tissue. Further, the areas highlighted by the different stains for any individual patient summed to values larger than 100%, indicating an extensive overlap of the elastin, collagen, and smooth muscle components within the wall.

3.3 Finite Element Analysis. The deformation in the central gage region was highly homogeneous (Figs. 2(b)–2(d)). Over the

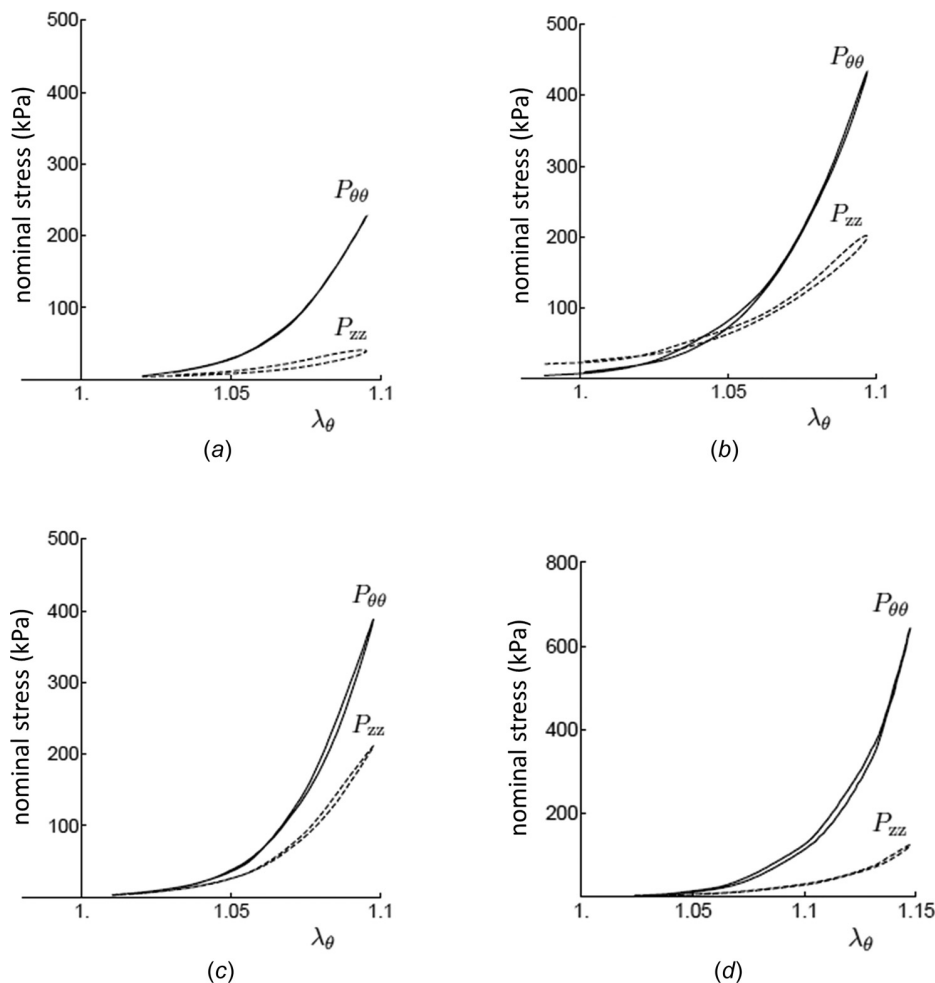


Fig. 4 Measured nominal stress components in the circumferential and axial directions, $P_{\theta\theta}$ and P_{zz} , for patient 2 during the fifth loading cycle in each test. (a) $\lambda_z = 1.0$, $\lambda_\theta \rightarrow 1.1$, (b) $\lambda_z = 1.1$, $\lambda_\theta \rightarrow 1.1$, (c) $\lambda_z \rightarrow 1.1$, $\lambda_\theta \rightarrow 1.1$, and (d) $\lambda_z = 1.0$, $\lambda_\theta \rightarrow 1.15$.

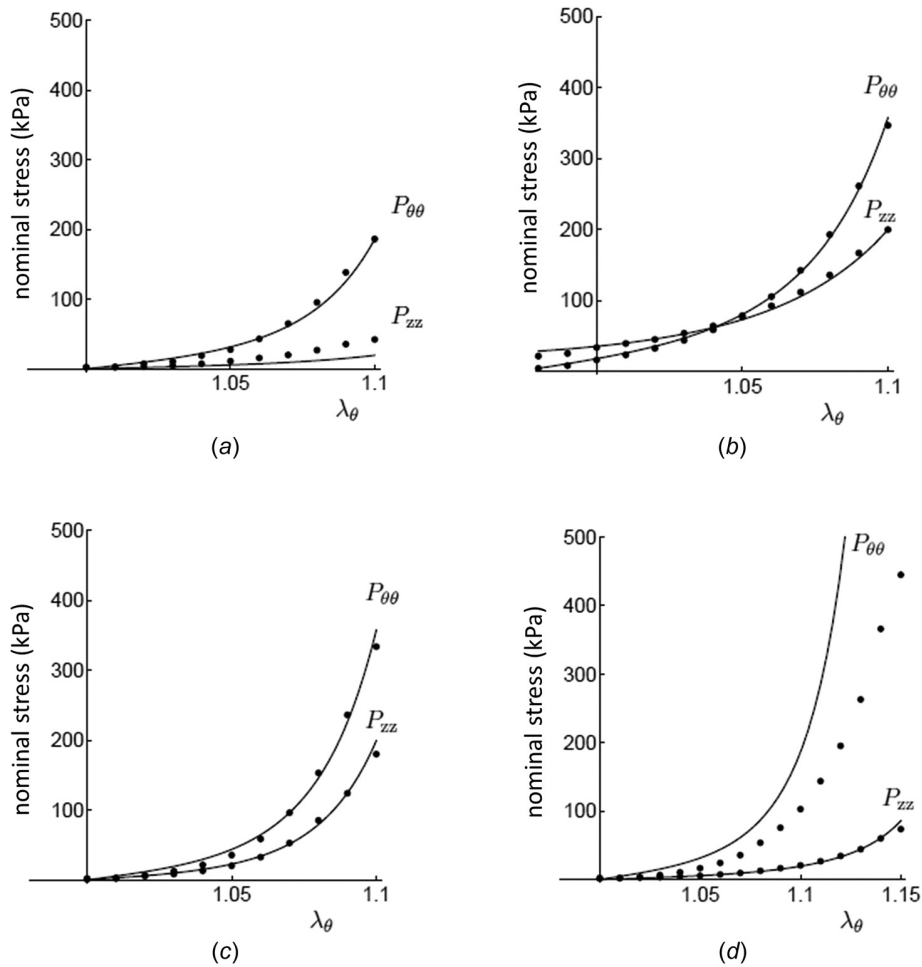


Fig. 5 Measured nominal stress components in the circumferential and axial directions, $P_{\theta\theta}$ and P_{zz} , during the fifth loading cycle in each test, averaged over all patient samples. (a) $\lambda_z = 1.0$, $\lambda_\theta \rightarrow 1.1$, (b) $\lambda_z = 1.1$, $\lambda_\theta \rightarrow 1.1$, (c) $\lambda_z \rightarrow 1.1$, $\lambda_\theta \rightarrow 1.1$, and (d) $\lambda_z = 1.0$, $\lambda_\theta \rightarrow 1.15$. Data points—measured values; solid curves—corresponding model fitted curves.

central gage region, axial stretch varied from 0.9840 to 0.9903, less than 0.7%, while circumferential stretch varied from 1.0909 to 1.0989, less than 0.8%. These values suggest that the size of the cruciform samples was appropriate for testing, and that the deformation in the central region was homogeneous.

3.4 Mechanical Behavior. The mechanical behavior of all individual tissue samples showed pronounced stretch-associated stiffening and was significantly anisotropic under all tests (Fig. 4, which shows measurements of the fifth loading cycle in each test for patient 2 as a representative example. Figure 4(a) shows the first test, λ_z fixed at 1.0 and λ_θ allowed to cycle to 1.1; Fig. 4(b) shows the second test, λ_z fixed at 1.1 and λ_θ allowed to cycle to

1.1; Fig. 4(c) shows the third test, λ_z and λ_θ both allowed to cycle to 1.1; and Fig. 4(d) shows the fourth test, λ_z fixed at 1.0 and λ_θ allowed to cycle to 1.15.) In tests with λ_z fixed at 1.1 and λ_θ allowed to cycle to 1.1, maximum axial stress varied from 147 to 207 kPa for the different samples, while maximum circumferential stress varied from 260 to 443 kPa. At all stretch levels in each test, stiffness was larger in the circumferential direction than the axial direction (Fig. 4). For example, for patient 2, MEM_θ and MEM_z were 11.1 and 5.64 MPa, respectively.

Stretch-associated stiffening behavior of the tissue was clearly apparent in the group-average measurements as well, as was anisotropic behavior (Fig. 5, which shows measurements of the fifth loading cycle in each test averaged over all patient samples along

Table 3 Mean mechanical properties. MEM_z was not calculated for tests in which λ_z was held constant. Test 1, λ_z fixed at 1.0 and λ_θ allowed to cycle to 1.1; test 2, λ_z fixed at 1.1 and λ_θ allowed to cycle to 1.1; test 3, λ_z and λ_θ both allowed to cycle to 1.1; and test 4, λ_z fixed at 1.0 and λ_θ allowed to cycle to 1.15.

	$MEM_\theta \pm SD$ (MPa)	$MEM_z \pm SD$ (MPa)	Max $P_{\theta\theta} \pm SD$ (kPa)	Max $P_{zz} \pm SD$ (kPa)	Dissip $\pm SD$ (%)
Test 1	4.6 ± 1.7	n.a.	180 ± 80	50 ± 30	11.6 ± 3.8
Test 2	6.2 ± 2.4	n.a.	340 ± 73	200 ± 32	10.6 ± 3.3
Test 3	10.5 ± 3.2	6.0 ± 1.2	310 ± 80	165 ± 59	7.9 ± 3.7
Test 4	11.6 ± 4.0	n.a.	460 ± 130	80 ± 50	10.8 ± 3.2

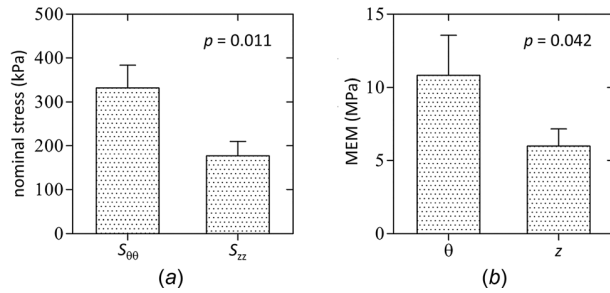


Fig. 6 (a) Values of mean maximum stresses and (b) of mean maximum elastic moduli in equibiaxial tension in the circumferential, (θ), and longitudinal, (z), directions

with the corresponding model fit curves). Best fit parameter values used to generate the model curves in Fig. 5 are given in Table 1. In tests with λ_z fixed at 1.1 and λ_θ allowed to cycle to 1.1, the mean maximum axial stress was 200 kPa, while the maximum mean circumferential stress was 340 kPa (Fig. 5(b), Table 3, $p = 0.01$). Mean MEM in the circumferential direction in this test was 6.2 MPa. In equibiaxial tests with both λ_z and λ_θ allowed to cycle to 1.1, mean maximum stresses were 310 and 165 kPa in the λ_θ and λ_z directions, respectively (Figs. 5(c) and 6(a), Table 3, $p = 0.01$). Mean MEM in this test was 10.5 MPa in the circumferential direction and 6.0 MPa in the longitudinal direction (Fig. 6(b), Table 3, $p = 0.04$). Mean percent energy dissipation in tests with λ_z fixed at 1.1 and λ_θ allowed to cycle to 1.1 was 10.6%, while mean percent energy dissipation in the equibiaxial tests was 7.9% (Table 3). Mean percent energy dissipation in the other tests was 11.6% and 10.8%, respectively (Table 3).

3.5 Correlations With Patient Characteristics. No statistically significant correlations were found between mean maximum circumferential stress, axial stress, or circumferential elastic modulus and patient characteristics including gender, age, body mass

index, maximum bulge diameter, smoking history, or the presence or absence of lipid or thrombus deposits or within the tissue samples (Table 4). However, maximum circumferential stress was statistically significantly inversely correlated with wall thickness ≥ 2.25 mm (110 ± 22 versus 225 ± 49 kPa, $p = 0.0043$), and positively correlated with hypertension ≥ 140 mm Hg (203 ± 71 versus 121 ± 17 kPa, $p = 0.040$), diabetes (240 ± 5.8 versus 163 ± 73 kPa, $p = 0.05$), and the presence of calcifications in the wall (235 ± 51 versus 130 ± 42 kPa, $p = 0.021$). Maximum axial stress was inversely correlated with wall thickness (30 ± 10 versus 74 ± 28 kPa, $p = 0.023$), while maximum circumferential elastic modulus was positively correlated with the presence of calcifications in the wall (5.76 ± 0.6 versus 3.18 ± 1.1 MPa, $p = 0.012$).

4 Discussion

In this study, the mechanical properties of AAA tissue samples from 13 patients undergoing open AAA repair were evaluated and compared with patient characteristics and tissue ultrastructure. The constitutive relationship used to model the biomechanical response provided an excellent fit to the measurements in almost all tests. No significant differences in mechanical properties as result of gender, age, or AAA diameter were detected, but mechanical properties were found to correlate with wall thickness, hypertension, diabetes, and the presence of wall calcifications.

Patients in this study were obtained as they presented, without regard to bulge size, patient natural history, or any other specific criteria. Major factors associated with the presence of AAA or the risk of rupture among the patients are summarized in Table 2. Nine of the 13 patients were male, and all but one were age 66 or higher. Hypertension was present in 69% (9/13). Interestingly, two factors that did not show a significant correlation with mechanical behavior were past family history of AAA, which was present in only one patient, and smoking. However, 92% (12/13) of the patients were either current or previous smokers, which suggest a strong correlation between smoking and the incidence of AAA. This is consistent with other studies showing each year of smoking to increase the relative risk of developing AAA by

Table 4 Statistical correlations between patient characteristics and mean maximum circumferential stress, axial stress, and maximum circumferential elastic modulus measured in tests with λ_z fixed at 1.0 and λ_θ allowed to cycle to 1.1. Statistically significant p -values are shown in bold. P -value for smoking history refers to comparison of previous to current smokers only.

Parameter	n	$P_{\theta\theta, \max}$ (kPa)	$P_{zz, \max}$ (kPa)	MEM_θ (MPa)		n	$P_{\theta\theta, \max}$ (kPa)	$P_{zz, \max}$ (kPa)	MEM_θ (MPa)		
Gender	Male	5	169 \pm 71	54 \pm 37	4.73 \pm 1.7	Smoking history	Current	5	162 \pm 82	52 \pm 18	3.73 \pm 1.6
	Female	3	204 \pm 81	53 \pm 25	4.04 \pm 1.7		Previous	2	202 \pm 48	73 \pm 38	5.98 \pm 0.9
	p -value	0.57	0.70	0.60			Never	1	244	114	5.18
							p -value	0.48	0.85	0.079	
Age	≥ 70	6	186 \pm 74	65 \pm 34	4.10 \pm 1.6	Family history	Yes	0	—	—	—
	< 70	2	172 \pm 90	37 \pm 3.5	5.61 \pm 1.4		No	8	340 \pm 73	200 \pm 33	6.24 \pm 2.4
	p -value	0.87	0.10	0.33			p -value	n.a.	n.a.	n.a.	
Body mass index (kg/m ²)	≥ 25	4	155 \pm 68	39 \pm 19	4.14 \pm 2.0	Diabetes (T1, T2)	Yes	2	240 \pm 5.8	77 \pm 53	5.89 \pm 1.0
	< 25	4	209 \pm 72	76 \pm 32	4.81 \pm 1.4		No	6	163 \pm 73	51 \pm 25	4.00 \pm 1.6
	p -value	0.32	0.11	0.60			p -value	0.05	0.62	0.14	
Maximum bulge diameter (mm)	≥ 60	4	152 \pm 69	58 \pm 42	4.27 \pm 1.6	Calcifications	≥ 1	4	235 \pm 51	77 \pm 32	5.76 \pm 0.6
	< 60	4	212 \pm 68	57 \pm 23	4.68 \pm 1.9		0	4	130 \pm 42	39 \pm 19	3.18 \pm 1.1
	p -value	0.26	0.97	0.75			p -value	0.021	0.099	0.012	
Wall thickness (mm)	≥ 2.25	3	110 \pm 22	30 \pm 10	3.10 \pm 1.4	Lipid deposits	≥ 2	5	159 \pm 62	59 \pm 37	4.10 \pm 1.4
	< 2.25	5	225 \pm 49	74 \pm 28	5.30 \pm 1.2		< 2	3	220 \pm 81	55 \pm 28	5.09 \pm 2.0
	p -value	0.0043	0.023	0.087			p -value	0.33	0.86	0.51	
Hypertension (Htn) > 140 mm Hg	Htn	6	203 \pm 71	65 \pm 34	4.73 \pm 1.7	Thrombus deposits	≥ 2	5	164 \pm 58	60 \pm 36	3.73 \pm 1.5
	Non-Htn	2	121 \pm 17	36 \pm 2.6	3.69 \pm 1.3		< 2	3	212 \pm 94	54 \pm 29	5.71 \pm 1.0
	p -value	0.040	0.095	0.45			p -value	0.49	0.80	0.07	

4%, with ex-smokers and current smokers being, respectively, at 3 and 7.6 times greater risk than nonsmokers [42,43].

Strain levels during the loading–unloading tests were chosen to reflect AAA deformations observed in vivo. Nagy et al. measured the full two-dimensional strain field experienced by a patient AAA in vivo over the cardiac cycle, calculating strains based on noninvasive electrocardiogram-gated magnetic resonance angiography imaging. For the patient studied, circumferential strains of 5–10% were widely distributed over the AAA bulge surface, while axial strains were limited to 1–2% except at a small number of specific points of high-wall curvature [44]. Measurements in our own laboratory using a similar noninvasive technique have found mean circumferential strains as large as 18% in some subjects (unpublished data). At these strains, tissue samples showed anisotropic behavior with stretch-associated stiffening and showed greater stiffness in the circumferential than the axial direction. These findings are consistent with reports from other authors [14,25,26,45,46]. However, the stress and anisotropy levels found here are generally greater than those reported by other authors. In equibiaxial tests, at 150 kPa, O’Leary et al. reported tangential moduli of 8.1 ± 3.2 and 6.6 ± 1.2 MPa [27] in the circumferential and axial directions, respectively, while Tong et al. reported 8.7 ± 1.7 and 6.6 ± 2.7 MPa [14]. Under corresponding conditions, Vande Geest et al. reported larger average moduli of 11.7 ± 1.9 and 8.3 ± 1.2 MPa [25]. Here, mean maximal moduli were 10.5 ± 3.2 and 6.0 ± 1.2 MPa, respectively, but were measured at an equibiaxial stretch ratio of 1.1, which produced higher mean stress levels of 310 ± 80 and 165 ± 59 kPa in the

circumferential and axial directions. The magnitude of the difference in moduli in the two directions was 20% for O’Leary et al. [27] and 27% for Tong et al. [14]. In contrast, moduli in the circumferential and axial directions reported by Vande Geest et al. [25] differed by 34%, while here they differed by 55%.

The most likely cause of these different stress and anisotropy values is that prestretch levels found in the iliac and carotid arteries [28,47–49] were reproduced as a boundary condition in two of our tests by keeping the deformation along the axial tissue direction constant, while the circumferential direction was cycled. Prestretch conditions were also imposed by Vande Geest et al. [25], but not by other authors [27,45]. The resulting difference in reference configurations may have contributed to differences in tissue behavior. In addition, inpatient differences in the histology of the tissue samples were not small, and both calcifications and bulge wall thickness can measurably affect tissue mechanical behavior [50]. Further, increased thrombus age has been shown to be associated with greater measured tissue anisotropy [14]. Data describing thrombus age was not available in the present study, and it is possible that differences in extensibility, stiffness, and anisotropy may in part have been associated with the presence or age of deposited mural thrombus.

Along with the large difference in mean maximal stiffness in the circumferential and axial directions, there were very large differences in mean maximal stress magnitudes in the two directions in each of our tests (Table 3). In the equibiaxial tests, mean maximum stress in the circumferential and axial directions differed by 63% (310 ± 80 versus 165 ± 59 kPa), and similar or even larger

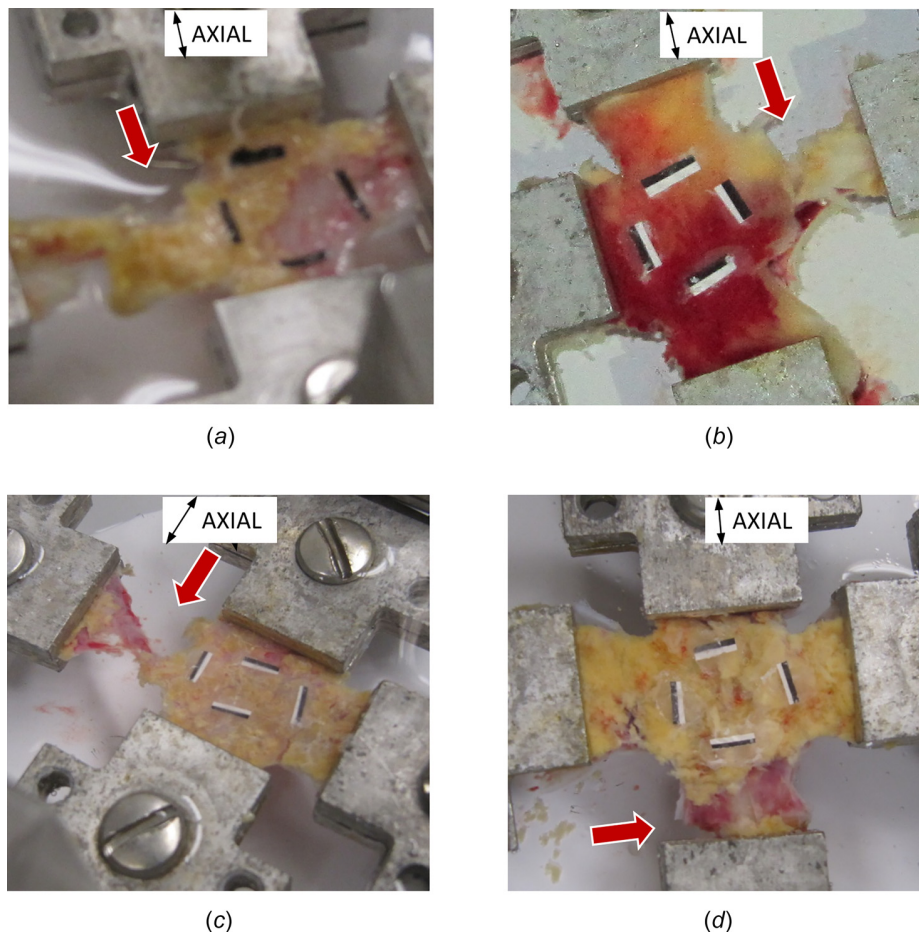


Fig. 7 Representative failure sites of tissue samples failing during biaxial extension tests. Axial arrow indicates the original axial orientation of the tissue sample in the AAA wall. Red arrow indicates the site and orientation of failure. (a) Patient 3, (b) patient 4, (c) patient 5, and (d) patient 6.

differences developed in the other tests. These differences suggested the need for an anisotropic constitutive model to fit the measured data accurately. The numerical results provided an excellent fit to the experimental measurements (Figs. 5(a)–5(c)). It has been shown that the best fit parameters may not be unique [51]. However, the parameters were determined by an objective technique [40], and goodness-of-fit was ≥ 0.98 for all but two of the fitted curves. The principal exception was the numerical values of $P_{\theta\theta}$ when λ_z was fixed at 1.0, while λ_θ was cycled to 1.15 (Fig. 5(d)), which were significantly larger than the experimental data for the same stretch. Numerical results in the first test (Fig. 5(a)) were identical to those in the fourth test (Fig. 5(d)) up to $\lambda_\theta = 1.1$, as required for an elastic material. However, the data clearly show that the material is less stiff in Fig. 5(d) compared to Fig. 5(a), which is most likely due to tissue damage accumulated during testing.

Inpatient differences in the distribution of smooth muscle and collagen and elastin fibers within the wall were striking (Fig. 3). The thresholding technique used to analyze the distribution of these components within the wall minimized the possibility of misinterpreting their relative distributions due to differences in the amount of stain applied to each component or the affinity of the component for the stain. Overall, these AAA samples demonstrated a general degradation of the normal distinctive constituents of the tunicae [41], which is consistent with findings reported by other authors [52]. Patient walls exhibited empty areas lined by fibrous elastin, indicating the possibility of encapsulation of foreign substance disrupting the normal wall ultrastructural organization. They also showed blood infiltration, delamination, inflammatory cell invasion, disruption of elastin, widespread fibroblasts, and highly perturbed connective tissue. The percent area of the wall staining positively for EvG, trichrome, and SMA also varied widely between patients (Fig. 3(f)). In general, patients with notably disorganized wall structure tended to show widely distributed collagen content. He and Roach [19] reported a significant decrease in the elastin and smooth muscle volume fractions of the aneurysmal wall, combined with a large increase in collagen and ground substance volumes. The current study showed much more inpatient variability than was reported by He and Roach, and general trends were correspondingly less apparent. However, three of the five patients showed significantly more coverage of trichrome than EvG, suggesting that collagen occupied a significantly larger fraction of the tissue volume than did elastin. Increased rates of collagen synthesis have been reported in AAA compared to healthy control [53]. The current results are consistent with that finding.

In view of the differences in wall ultrastructure, it is not surprising that mechanical properties also differed significantly between patients. In equibiaxial tests, maximum stiffness in the circumferential direction, MEM_θ , varied from 7.12 MPa (patient 4) to 13.4 MPa (patient 6). Maximum stiffness in the axial direction, MEM_z , varied from 5.02 MPa to 7.3 MPa. Maximum circumferential stress, $P_{\theta\theta}$, varied from 281.4 kPa (patient 6) to 383.2 kPa (patient 2), while maximum axial stress, P_{zz} , varied from 143.0 kPa to 208.8 kPa. Further, although all tissue samples in this study were obtained from the anterior region of the AAA wall, the samples differed in their gross structure and in the presence and distribution of calcifications, lipid, and thrombus deposits (Fig. 7). There also were significant spatial variations within the ultrastructure of most individual samples (Fig. 3). These variations, along with the observation of significant histologic disorganization reported by Erhart et al. [54], suggest that AAA walls may be more structurally and histopathologically heterogeneous than has often been recognized to date. As a result, there are experimentally based reasons to suggest that in addition to varying between patients, mechanical properties may be spatially inhomogeneous within the wall of individual patients as well. Wall stress calculations to date have primarily assumed the wall to be characterized by a single homogeneous mechanical response [11–16,55,56]. However, the histopathologic images of the current study suggest

this may not be a safe assumption. Initial wall stress studies allowing spatially inhomogeneous mechanical behavior have recently been described by Reeps et al. [50], Tierney et al. [57], and Polzer and Gasser [58].

Previous studies of AAA mechanical properties have reported inconsistent findings with regard to differences in tissue properties as a function of patient gender, age, and maximum bulge diameter. In some studies, tissue samples from male patients have been reported to have greater stiffness and tensile strength than samples from female patients [14,25,50], but in other studies no statistically significant difference was found [27]. The current study found no statistically significant differences in elastic mechanical properties based on gender. In addition, it is generally thought that the stiffness of the nonaneurysmal aorta increases with age [59], which is attributed to a gradual loss of elastin and increase in the collagen content of the wall over time. However, no statistically significant change in the mechanical properties of AAA tissue samples has been found for patients over or under age 70 [27]. The current study similarly found no differences in maximal stress or stiffness for patients over 70 compared to those under 70. It is possible that the loss of ultrastructural organization associated with the AAA wall offsets age-related changes in the wall collagen or elastin content. As a result, no general trend of mechanical properties develops.

A large study of the uniaxial properties of AAA wall tissue samples reported tissue from patients with maximum bulge diameter greater than 5.5 cm to have higher failure strength and extensibility than samples from patients less than 5.5 cm [60]. However, biaxial studies more accurately replicating deformations experienced by the wall in vivo have not found statistically significant differences in mechanical properties with bulge diameter [27]. The current study evaluated maximal wall stress and stiffness rather than failure strength, but also did not find statistically significant differences in these properties with diameter. The smaller number of patients in the current study may explain part of the absence of a difference. In addition, it has been suggested that increases in wall strength as bulge diameter increases may reflect a remodeling process in the wall that results in growth of the total mass of collagen present [60]. However, the rate at which remodeling might proceed and the relations between remodeling rate and bulge shape and size are not yet known. The current study does not support the hypothesis that collagen deposition during the remodeling process occurs in an ultrastructurally organized pattern producing a significant difference in mechanical properties between patients greater than or less than 5.5 cm in diameter.

Furthermore, the current study found no statistically significant differences in tissue mechanical properties based on other clinically observable factors specific to individual patients, including height, weight, and body mass index. Surprisingly, given the prevalence of smoking among the patients studied and the pathophysiologic tissue degradations associated with smoking, mechanical properties were independent of current versus past history of smoking. Previous studies have also not found a correlation between mechanical properties and smoking [61]. Although a larger patient cohort would be needed to draw conclusions with confidence, it does not seem likely that these parameters can be used to discriminate patients with mechanical properties suggesting a high risk of rupture. However, the presence of calcifications has been suggested to correlate with wall stiffness [50] as well as with high risk of rupture [62], and in correspondence with this suggestion, the current study showed a significant dependence of stiffness and stress on the presence or absence of calcifications in the wall. Further study of the effect of calcification on wall properties may provide further insight into AAA rupture risk.

To our knowledge, the current study represents the first attempt to evaluate the mechanical properties of patient AAA wall tissue samples using a physiologically realistic true strain-controlled protocol. Deformations experienced by the wall in vivo were emulated by imposing known strain on a small region at the center of the tissue sample. Since only strain in the gage region was tracked

and used for control, our method avoided errors associated with nonhomogeneous distortions of the tissue in the near region of the grips. In addition, the grips themselves successfully held the tissue samples in place with no evidence of slippage, tear out, or other tissue damage. Nevertheless, the study was subject to several limitations. First, the number of patients was not large. Other studies of the biaxial mechanical behavior of AAA tissue samples with larger patient groups have been previously published [25,27]. However, those studies were not carried out with true strain control. Because of the current use of EVAR for surgical repair of nearly all patient AAAs, opportunities to acquire tissue samples for experimental study are becoming increasingly rare. The infrequency with which tissue samples can be obtained, in combination with significant inpatient variability of tissue mechanical properties, suggest the importance of adding as many measurements as possible to the published data while that can be done.

A related point is the potential for bias in the measured data, since tissue can only be obtained from patients not suitable for EVAR because of their geometric complexity or because of the density of calcifications in their wall. As a result, it is possible that the measured wall properties do not adequately reflect the average AAA patient.

A second limitation is that all tissue samples were obtained from the anterior region of the patient sac. Inter- and inpatient variations in the wall ultrastructure were significant, suggesting that tissue mechanical properties may vary with position within the AAA sac [54,57]. Unfortunately, the sac region from which tissue can be acquired is presently limited by the surgical technique with which the tissue is excised. In particular, it would be of interest to compare the present measurements with the properties of the site of rupture. However, it appears to only be possible to obtain tissue from the rupture site post mortem. Finally, a third limitation is that although tissue prestretch in the axial direction in vivo was emulated in the test protocol, circumferential components of residual strain, if present, were not accommodated for in this analysis.

5 Conclusions

The goals of this study were to evaluate the mechanical properties of patient AAA tissue samples with a true strain-controlled biaxial test protocol and to correlate those properties with patient characteristics and tissue histopathologic features. The gross appearance of the AAA tissue samples showed amounts of atherosclerotic plaque, calcified deposits, and thrombus that differed substantially between patients. In general, the samples exhibited substantial degradation of the healthy wall ultrastructural organization, with perturbed, delaminated connective tissue, elastin degradation, blood infiltration, and inflammatory cell invasion. Strain-controlled biaxial tests showed tissue samples to be anisotropic, with a greater tendency toward stiffening under load in the circumferential direction than the axial direction. An anisotropic, hyperelastic constitutive model fit the measured data well. No statistically significant differences in tissue mechanical properties were found based on patient characteristics including gender, age, maximum bulge diameter, height, weight, body mass index, or smoking history. Although a larger patient cohort is needed to confirm these conclusions, it does not seem likely that these parameters can be used clinically to discriminate patients with mechanical properties suggestive of a high risk of rupture. Further study of the relations between wall thickness, ultrastructure, and stress development may provide insight into rupture risk.

Acknowledgment

This work was supported by the National Science Foundation (Grant Nos. CMMI-1031366 and CMMI-1352955). The authors are grateful to Ms. Christa Margossian for assistance obtaining the tissue samples and Ms. Rio Nomoto for retrieving patient anamnesis data.

References

- Ashton, H. A., Buxton, M. J., Day, N. E., Kim, L. G., Marteau, T. M., Scott, R. A., Thompson, S. G., and Walker, N. M., 2002, "The Multicentre Aneurysm Screening Study (Mass) Into the Effect of Abdominal Aortic Aneurysm Screening on Mortality in Men: A Randomized Control Trial," *Lancet*, **360**, pp. 1531–1539.
- Lederle, F. A., Johnson, G. R., Wilson, S. E., Ballard, D. J., Jordan, W. D., Jr., Blebea, J., Littooy, F. N., Freischlag, J. A., Bandyk, D., Rapp, J. H., and Salam, A. A., 2002, "Veterans Affairs Cooperative Study, I. Rupture Rate of Large Abdominal Aortic Aneurysms in Patients Refusing or Unfit for Elective Repair," *J. Am. Med. Assoc.*, **287**(22), pp. 2968–2972.
- Karkos, C., Mukhopadhyay, U., Papakostas, I., Ghosh, J., Thomson, G., and Hughes, R., 2000, "Abdominal Aortic Aneurysm: The Role of Clinical Examination and Opportunistic Detection," *Eur. J. Vasc. Endovasc. Surg.*, **19**(3), pp. 299–303.
- Davis, M., Harris, M., and Earnshaw, J. J., 2013, "Implementation of the National Health Service Abdominal Aortic Aneurysm Screening Program in England," *J. Vasc. Surg.*, **57**(5), pp. 1440–1445.
- Lederle, F. A., 2009, "The Natural History of Abdominal Aortic Aneurysm," *Acta Chir. Belg.*, **109**(1), pp. 7–12.
- CDC, 2015, "National Center for Health Statistics," Centers for Disease Control and Prevention, Atlanta, GA, accessed, June 2015, www.cdc.gov/nchs/deaths.htm
- Grootenboer, N., Bosch, J., Hendriks, J. M., and van Sambeek, M. R. H. M., 2009, "Epidemiology, Aetiology, Risk of Rupture and Treatment of Abdominal Aortic Aneurysms: Does Sex Matter?," *Eur. J. Vasc. Endovasc. Surg.*, **38**(3), pp. 278–284.
- Lederle, F. A., Wilson, S. E., Johnson, G. R., Reinke, D. B., Littooy, F. N., Acher, C. W., Ballard, D. J., Messina, L. M., Gordon, I. L., Chute, E. P., Krupski, W. C., Busuttill, S. J., Barone, G. W., Sparks, S., Graham, L. M., Rapp, J. H., Makaroun, M. S., Moneta, G. L., Cambria, R. A., Makhoul, R. G., Eton, D., Ansel, H. J., Freischlag, J. A., and Bandyk, D., 2002, "Immediate Repair Compared With Surveillance of Small Abdominal Aortic Aneurysms," *N. Engl. J. Med.*, **346**(19), pp. 1437–1444.
- Nevitt, M. P., Ballard, D. J., and Hallett, J. W., 1989, "Prognosis of Abdominal Aortic Aneurysms: A Population Based Study," *N. Engl. J. Med.*, **321**(15), pp. 1009–1014.
- Thompson, S., Brown, L., Sweeting, M., Bown, M., Kim, L., Glover, M., Buxton, M., and Powell, J., 2013, "Systematic Review and Meta-Analysis of the Growth and Rupture Rates of Small Abdominal Aortic Aneurysms: Implications for Surveillance Intervals and Their Cost-Effectiveness," *Health Technol. Assess.*, **17**(41), pp. 1–118.
- Fillinger, M. F., Raghavan, M. L., Marra, S. P., Cronenwett, J. L., and Kennedy, F. E., 2002, "In Vivo Analysis of Mechanical Wall Stress and Abdominal Aortic Aneurysm Rupture Risk," *J. Vasc. Surg.*, **36**(3), pp. 589–597.
- Fillinger, M. F., 2007, "Who Should We Operate on and How Do We Decide: Predicting Rupture and Survival in Patients With Aortic Aneurysm," *Semin. Vasc. Surg.*, **20**(2), pp. 121–127.
- Larsson, E., Labruto, F., Gasser, T., Swedenborg, J., and Hultgren, R., 2011, "Analysis of Aortic Wall Stress and Rupture Risk in Patients With Abdominal Aortic Aneurysm With a Gender Perspective," *J. Vasc. Surg.*, **54**(2), pp. 295–299.
- Tong, J., Cohnert, T., Regitnig, P., and Holzapfel, G. A., 2011, "Effects of Age on the Elastic Properties of the Intraluminal Thrombus and the Thrombus-Covered Wall in Abdominal Aortic Aneurysms: Biaxial Extension Behaviour and Material Modelling," *Eur. J. Vasc. Endovasc. Surg.*, **42**(2), pp. 207–219.
- Dorfmann, A., Wilson, C., Edgar, E. S., and Peattie, R. A., 2010, "Evaluating Patient-Specific Abdominal Aortic Aneurysm Wall Stress Based on Flow-Induced Loading," *Biomech. Model. Mechanobiol.*, **9**(2), pp. 127–139.
- Ahamed, T., Dorfmann, L., and Ogden, R. W., 2016, "Modelling of Residually Stressed Materials With Application to AAA," *J. Mech. Behav. Biomed. Mater.*, **61**, pp. 221–234.
- Campa, J. S., Greenhalgh, R. M., and Powell, J. T., 1987, "Elastin Degradation in Abdominal Aortic Aneurysms," *Atherosclerosis*, **65**, pp. 12–21.
- Choke, E., Cockerill, G., Wilson, W. R. W., Sayed, S., Dawson, J., Loftus, I., and Thompson, M. M., 2005, "A Review of Biological Factors Implicated in Abdominal Aortic Aneurysm Rupture," *Eur. J. Vasc. Endovasc. Surg.*, **30**(3), pp. 227–244.
- He, C. M., and Roach, M. R., 1994, "The Composition and Mechanical Properties of Abdominal Aortic Aneurysm," *J. Vasc. Surg.*, **20**(1), pp. 6–13.
- Summer, D. S., Hokanson, D. S., and Strandness, D. E. J., 1970, "Stress Strain Characteristics and Collagen Elastin Content of Abdominal Aortic Aneurysms," *Surg. Gynecol. Obstet.*, **130**(3), pp. 459–466.
- McGee, G. S., Baxter, B. T., Shively, V. P., Chisholm, R., McCarthy, W. J., Flinn, W. R., Yao, J. S. T., and Pearce, W. H., 1991, "Aneurysm or Occlusive Disease-Factors Determining the Clinical Course of Atherosclerosis of the Infra-renal Aorta," *Surgery*, **110**(2), pp. 370–376.
- Vorp, D. A., 2007, "Biomechanics of Abdominal Aortic Aneurysm," *J. Biomech.*, **40**(9), pp. 1887–1902.
- Maier, A., Gee, M. W., Reeps, C., Eckstein, H. H., and Wall, W. A., 2010, "Impact of Calcifications on Patient-Specific Wall Stress Analysis of Abdominal Aortic Aneurysms," *Biomech. Model. Mechanobiol.*, **9**(5), pp. 511–521.
- Buijs, R. V., Willems, T. P., Tio, R. A., Boersma, H. H., Tielliu, I. F., Slart, R. H., and Zeebregts, C. J., 2013, "Calcification as a Risk Factor for Rupture of Abdominal Aortic Aneurysm," *Eur. J. Vasc. Endovasc. Surg.*, **46**(5), pp. 542–548.
- Vande Geest, J. P., Sacks, M. S., and Vorp, D. A., 2006, "The Effects of Aneurysm on the Biaxial Mechanical Behavior of Human Abdominal Aorta," *J. Biomech.*, **39**(7), pp. 1324–1334.

- [26] Tong, J., Schriefel, A. J., Cohnert, T., and Holzapfel, G. A., 2013, "Gender Differences in Biomechanical Properties, Thrombus Age, Mass Fraction and Clinical Factors of Abdominal Aortic Aneurysms," *Eur. J. Vasc. Endovasc. Surg.*, **45**(4), pp. 364–372.
- [27] O'Leary, S. A., Healey, D. A., Kavanagh, E. G., Walsh, M. T., McGloughlin, T. M., and Doyle, B. J., 2014, "The Biaxial Biomechanical Behavior of Abdominal Aortic Aneurysm Tissue," *Ann. Biomed. Eng.*, **42**(12), pp. 2440–2450.
- [28] Holzapfel, G. A., Sommer, G., and Regitnig, P., 2004, "Anisotropic Mechanical Properties of Tissue Components in Human Atherosclerotic Plaques," *ASME J. Biomech. Eng.*, **126**(5), pp. 657–665.
- [29] Abu-Farha, F., Hector, L. G., Jr., and Khraisheh, M., 2009, "Cruciform-Shaped Specimens for Elevated Temperature Biaxial Testing of Lightweight Materials," *J.O.M.*, **61**(8), pp. 48–56.
- [30] Waldman, S. D., and Lee, J. M., 2005, "Effect of Sample Geometry on the Apparent Biaxial Mechanical Behaviour of Planar Connective Tissues," *Biomaterials*, **26**(35), pp. 7504–7513.
- [31] Pancheri, F. P., and Dorfmann, A., 2014, "Strain Controlled Biaxial Tension of Natural Rubber: New Experimental Data," *Rubber Chem. Technol.*, **87**(1), pp. 120–138.
- [32] Hansen, F., Bergqvist, D., Mangell, P., Rydén, A., Sonesson, B., and Länne, T., 1993, "Non-Invasive Measurement of Pulsatile Vessel Diameter Change and Elastic Properties Human Arteries: A Methodological Study," *Clin. Physiol.*, **13**(6), pp. 631–643.
- [33] Länne, T., Stale, H., Bengtsson, H., Gustafsson, D., Bergqvist, D., Sonesson, B., Lecerof, H., and Dahl, P., 1992, "Noninvasive Measurement of Diameter Changes in the Distal Abdominal Aorta in Man," *Ultrasound Med. Biol.*, **18**(5), pp. 451–457.
- [34] ABAQUS, Inc., 2013, "Abaqus, Theory Manual," Dassault Systèmes Simulia, Waltham, MA, Version 6.13.
- [35] Demiray, H., 1972, "A Note on the Elasticity of Soft Biological Tissues," *J. Biomech.*, **5**(3), pp. 309–311.
- [36] Holzapfel, G. A., Gasser, T. C., and Ogden, R. W., 2000, "A New Constitutive Framework for Arterial Wall Mechanics and a Comparative Study of Material Models," *J. Elasticity*, **61**, pp. 1–48.
- [37] Ogden, R. W., 1997, *Non-Linear Elastic Deformations*, Dover Publications, New York.
- [38] Pancheri, F. Q., Eng, C. M., Lieberman, D. E., Biewener, A. A., and Dorfmann, L., 2014, "A Constitutive Description of the Anisotropic Response of the Fascia Lata," *J. Mech. Behav. Biomed.*, **30**, pp. 306–323.
- [39] Pancheri, F. Q., Eng, C. M., Lieberman, D. E., Biewener, A. A., and Dorfmann, L., 2015, "Corrigendum to: A Constitutive Description of the Anisotropic Response of the Fascia Lata," *J. Mech. Behav. Biomed.*, **50**, pp. 308–310.
- [40] Buzzi-Ferraris, G., and Manenti, F., 2009, "Kinetic Models Analysis," *Chem. Eng. Sci.*, **64**(5), pp. 1061–1074.
- [41] Junqueira, L. C., and Carneiro, J., 2005, *Basic Histology: Text & Atlas*, 11th ed., McGraw-Hill Lange, New York.
- [42] Baxter, B. T., Terrin, M. C., and Dalman, R. L., 2008, "Medical Management of Small Abdominal Aortic Aneurysms," *Circulation*, **117**(14), pp. 1883–1889.
- [43] Wilmsink, T. B. M., Quick, C. R. G., and Day, N. E., 1999, "The Association Between Cigarette Smoking and Abdominal Aortic Aneurysms," *J. Vasc. Surg.*, **30**(6), pp. 1099–1105.
- [44] Nagy, R., Csobay-Novák, C., Lovas, A., Sótonyi, P., and Bojtár, I., 2015, "Non-Invasive in vivo Time-Dependent Strain Measurement Method in Human Abdominal Aortic Aneurysms: Towards a Novel Approach to Rupture Risk Estimation," *J. Biomech.*, **48**(10), pp. 1876–1886.
- [45] Polzer, S., Gasser, T. C., Bursa, J., Staffa, R., Vlachovsky, R., Man, V., and Skacel, P., 2013, "Importance of Material Model in Wall Stress Prediction in Abdominal Aortic Aneurysms," *Med. Eng. Phys.*, **35**(9), pp. 1282–1289.
- [46] Gasser, T. D., Gallinetti, S., Xing, X., Forsell, C., Swedenborg, J., and Roy, J., 2012, "Spatial Orientation of Collagen Fibers in the Abdominal Aortic Aneurysm's Wall and Its Relation to Wall Mechanics," *Acta Biomater.*, **8**(8), pp. 3091–3103.
- [47] Schulze-Bauer, C. A. J., Morth, C., and Holzapfel, G. A., 2003, "Passive Biaxial Mechanical Response of Aged Human Iliac Arteries," *ASME J. Biomech. Eng.*, **125**(3), pp. 395–406.
- [48] Sommer, G., Regitnig, P., Koeltringer, L., and Holzapfel, G. A., 2010, "Biaxial Mechanical Properties of Intact and Layer-Dissected Human Carotid Arteries at Physiological and Supraphysiological Loadings," *Am. J. Physiol.-Heart C.*, **298**(3), pp. H898–H912.
- [49] Sommer, G., and Holzapfel, G. A., 2012, "3D Constitutive Modeling of the Biaxial Mechanical Response of Intact and Layer-Dissected Human Carotid Arteries," *J. Mech. Behav. Biomed. Mater.*, **5**(1), pp. 116–128.
- [50] Reeps, C., Maier, A., Pelisek, J., Härtl, F., Grabher-Meier, V., Wall, W. A., Essler, M., Eckstein, H. H., and Gee, M. W., 2013, "Measuring and Modeling Patient-Specific Distributions of Material Properties in Abdominal Aortic Aneurysm Wall," *Biomech. Model. Mechanobiol.*, **12**(4), pp. 717–733.
- [51] Ogden, R. W., Saccomandi, G., and Sgura, I., 2004, "Fitting Hyperelastic Models to Experimental Data," *Comput. Mech.*, **34**(6), pp. 484–502.
- [52] Lindeman, J. H. N., Ashcroft, B. A., Beenakker, J. W. M., van Es, M., Koekkoek, N. B. R., Prins, F. A., Tielemans, J. F., Abdul-Hussien, H., Bank, R. A., and Oosterkamp, T. H., 2010, "Distinct Defects in Collagen Microarchitecture Underlie Vessel-Wall Failure in Advanced Abdominal Aneurysms and Aneurysms in Marfan Syndrome," *Proc. Natl. Acad. Sci.*, **107**(2), pp. 862–865.
- [53] Wilson, K., Lindholt, J., Hoskins, P., Heickendorff, L., Vammen, S., and Bradbury, A., 2001, "The Relationship Between Abdominal Aortic Aneurysm Distensibility and Serum Markers of Elastin and Collagen Metabolism," *Eur. J. Vasc. Endovasc. Surg.*, **21**(2), pp. 175–178.
- [54] Erhart, P., Grond-Ginsbach, C., Hakimi, M., Lasitschka, F., Dihlmann, S., Böckler, D., and Alexander Hyhlik-Dürr, A., 2014, "Finite Element Analysis of Abdominal Aortic Aneurysms: Predicted Rupture Risk Correlates With Aortic Wall Histology in Individual Patients," *J. Endovasc. Ther.*, **21**(4), pp. 556–564.
- [55] Rissland, P., Alemu, Y., Einav, S., Ricotta, J., and Bluestein, D., 2009, "Abdominal Aortic Aneurysm Risk of Rupture: Patient-Specific FSI Simulations Using Anisotropic Model," *ASME J. Biomech. Eng.*, **131**(3), p. 031001.
- [56] Raut, S. S., Jana, A., De Oliveira, V., Muluk, S. C., and Finol, E. A., 2013, "The Importance of Patient-Specific Regionally Varying Wall Thickness in Abdominal Aortic Aneurysm Biomechanics," *ASME J. Biomech. Eng.*, **135**(8), p. 81010.
- [57] Tierney, A. P., Callanan, A., and McGloughlin, T. M., 2012, "Use of Regional Mechanical Properties of Abdominal Aortic Aneurysms to Advance Finite Element Modeling of Rupture Risk," *J. Endovasc. Ther.*, **19**(1), pp. 100–114.
- [58] Polzer, S., and Gasser, T. C., 2015, "Biomechanical Rupture Risk Assessment of Abdominal Aortic Aneurysm Based on a Novel Probabilistic Rupture Risk Index," *J. R. Soc. Interface*, **12**(113), p. 20150852.
- [59] Imura, T., Yamamoto, K., Kanamori, K., Mikami, T., and Yasuda, H., 1986, "Non-Invasive Ultrasonic Measurement of the Elastic Properties of the Human Abdominal Aorta," *Cardiovasc. Res.*, **20**(3), pp. 208–214.
- [60] Tavares Monteiro, J., Simão da Silva, E., Raghavan, M., Puech-Leão, P., Higuichi, M., and Otoch, J., 2013, "Histologic, Histochemical, and Biomechanical Properties of Fragments Isolated From the Anterior Wall of Abdominal Aortic Aneurysms," *J. Vasc. Surg.*, **59**, pp. 1393–1401.
- [61] Vande Geest, J. P., Wang, D. H. J., Wisniewski, S. R., Makaroun, M. S., and Vorp, D. A., 2006, "Towards a Noninvasive Method for Determination of Patient-Specific Wall Strength Distribution in Abdominal Aortic Aneurysms," *Ann. Biomed. Eng.*, **34**(7), pp. 1098–1106.
- [62] Buijs, R. V., Willems, T. P., Tio, R. A., Boersma, H. H., Tielliu, I. F., Slart, R. H., and Zeebregts, C. J., 2013, "Calcification as a Risk Factor for Rupture of Abdominal Aortic Aneurysm," *Eur. J. Vasc. Endovasc. Surg.*, **46**(5), pp. 542–548.

References

- [1] Adler JH, Dorfmann L, Han D, MacLachlan S, Paetsch C (2014) Mathematical and computational models of incompressible materials subject to shear. *IMA J Appl Math* 79:889–914
- [2] Ahamed T, Dorfmann L, Ogden RW (2016) Modelling of residually stressed materials with application to AAA. *J Mech Behav Biomed* 61:221–234
- [3] Ahamed T, Peattie RA, Dorfmann L, Cherry Kemmerling EM (2018) Pulsatile flow measurements and wall stress distribution in a patient specific abdominal aortic aneurysm, in review.
- [4] Arribas SM, Hinek A, Gonza MC (2006) Elastic fibres and vascular structure in hypertension. *Pharmacology and Therapeutics* 111:771–791
- [5] Ashton HA, Buxton MJ, Day NE, Kim LG, Marteau TM, Scott RA, Thompson SG, Walker NM (2002) The multicentre aneurysm screening study (MASS) into the effect of abdominal aortic aneurysm screening on mortality in men: A randomized control trial. *Lancet* 360:1531–1539
- [6] Baaijens F, Bouten C, Driessen N (2010) Modeling collagen remodeling. *J Biomech* 43:166–175
- [7] Baek S, Rajagopal KR, Humphrey JD (2006) A theoretical model of enlarging intracranial fusiform aneurysms. *ASME J Biomech Eng* 128:142–149

- [8] Baek S, Humphrey JD (2010) Computational modeling of growth and remodeling in biological soft tissues: application to arterial mechanics. *Comp Modeling in Biomech*, DOI 10.1007/978
- [9] Batchelor GK (1967) *An introduction to fluid dynamics*. Cambridge University Press 73 ISBN 0-521-66396-2
- [10] Blanchard JF, Armenian HK, Friesen PP (2000) Risk factors for abdominal aortic aneurysm: results of a case-control study. *Am J Epidemiol* 151(6):575–583
- [11] Boyle JJ, Bowyer DE, Weissberg PL, Bennett MR (2001) Human blood-derived macrophages induce apoptosis in human plaque-derived vascular smooth muscle cells by Fas-ligand/Fas interactions. *Arterioscler Thromb Vasc Biol* 21(9): 1402–1407
- [12] Braeu FA, Seitz A, Aydin RC, Cyron CJ (2016) Homogenized constrained mixture models for anisotropic volumetric growth and remodeling. *Biomech Model Mechan* Doi:10.1007/s10237-016-0859-1
- [13] Brewster DC, Cronenwett JL, Hallett JW (2003) Guidelines for the treatment of abdominal aortic aneurysms. Report of a subcommittee of the joint council of the american association for vascular surgery and society for vascular surgery. *J Vasc Surg* 37:17–21
- [14] Carmo M, Colombo L, Bruno A, Corsi FRM, Roncoroni L, Cuttin MS, Radice F, Mussini E, Settembrini PG (2002) Alteration of elastin, collagen and their cross-links in abdominal aortic aneurysms. *Eur J Vasc Endovasc Surg* 2002; 23:543–549

- [15] Chang TYP, Saleeb AF, Li G (1991) Large strain analysis of rubber-like materials based on a perturbed Lagrangian variational principle. *Comp Mech* 8(4):221–233
- [16] Cheheltani R, Pichamuthu JE, Rao J, Weinbaum JS, Kiani, MF, Vorp DA, Pleshko, N (2017) Fourier transform infrared spectroscopic imaging-derived collagen content and maturity correlates with stress in the aortic wall of abdominal aortic aneurysm patients. *Cardiovasc Eng Tech* 8:70–80
- [17] Choke E, Cockerill G, Wilson WRW, Sayed S, Dawson J, Loftus I, Thompson MM (2005) A review of biological factors implicated in abdominal aortic aneurysm rupture. *Eur J Vasc Endovasc Surg* 30:227–244
- [18] Comellas E, Gasser TC, Bellomo F.J., Oller S. (2016) A homeostatic-driven turnover remodelling constitutive model for healing in soft tissue.
- [19] Cronenwett JL, Sargent SK, Wall MH, Hawkes ML, Freeman DH, Dain BJ (1990) Variables that affect the expansion rate and outcome of small abdominal aortic aneurysms. *J Vasc Surg* 11(2):260–268
- [20] Cyron CJ, Wilson JS, Humphrey JD (2014) Mechanobiological stability: a new paradigm to understand the enlargement of aneurysms? *J Roy Soc Interface* 11:20140680.
- [21] Cyron CJ, Humphrey JD (2014) Vascular homeostasis and the concept of mechanobiological stability. *Int J Eng Sci* 85: 203–223.

- [22] Cyron CJ, Humphrey JD (2017) Growth and remodeling of load-bearing biological soft tissues. *Meccanica* 52:645-664
- [23] Darling RC (1970) Ruptured arteriosclerotic abdominal aortic aneurysms, a pathologic and clinical study. *Am J Surg* 119:397-401
- [24] Darling RC, Messina CR, Brewster DC, Ottinger LW (1977) Autopsy study of unoperated abdominal aortic aneurysms, *Circ* 56:161-164
- [25] Davarani SZ, Sheidaei A, Baek S (2011) A finite element model of stress-mediated vascular adaptation: application to abdominal aortic aneurysm. *Comp Meth in Biom and Biom Eng*. Vol. 14, No.9, Sep 2011, 803-817
- [26] Dorfmann AL, Wilson C, Edgar ES, Peattie RA (2010) Evaluating patient-specific abdominal aortic aneurysm wall stress based on flow-induced loading. *Biomech Model Mechanobiol* 9:127-139
- [27] Driessen NJB, Peters GWM, Huyghe JM, Bouten CVC, Baaijens FPT (2003) Remodeling of continuously distributed collagen fibers in soft connective tissues. *J Biomech* 36:1151-1158
- [28] Driessen NJB, Wilson W, Bouten CVC, Baaijens FPT (2004) A computational model for collagen fiber remodeling in the arterial wall. *J Thero Biol* 226:53-64
- [29] Enevoldsen MS, Henneberg KA, Jensen JA, Lonn L, Humphrey JD (2011) New interpretation of arterial stiffening due to cigarette smoking using a structurally-motivated constitutive model. *J Biomech*. 2011; 44:1209-1211

- [30] Erhart P, Grond-Ginsbach C, Hakimi M, Lasitschka F, Dihlmann S, Böckler D, Alexander Hyhlik-Dürr A (2014) Finite element analysis of abdominal aortic aneurysms: Predicted rupture risk correlates with aortic wall histology in individual patients. *J Endovasc Ther* 21:556–564
- [31] Erhart P, Hyhlik-Dürr A, Geisbüsch P, Kotelis D, Müller-Eschner M, Gasser T, von Tengg- Kobligk H, Böckler D (2015) Finite element analysis in asymptomatic, symptomatic, and ruptured abdominal aortic aneurysms: In search of new rupture risk predictors. *Eur J Vasc Endovasc* 49:239–245
- [32] Eriksson T, Watton P, Luo X, and Ventikos Y (2014) Modelling volumetric growth in a thick walled fibre reinforced artery. *J Mech Phys Solids* 73:134–150
- [33] Fillinger MF, Raghavan ML, Marra SP, Cronenwett JL, Kennedy FE (2002) In vivo analysis of mechanical wall stress and abdominal aortic aneurysm rupture risk. *J Vasc Surg* 36: 589–597
- [34] Fillinger MF, Marra SP, Raghavan ML, Kennedy FE (2003) Prediction of rupture risk in abdominal aortic aneurysm during observation: Wall stress versus diameter. *J Vasc Surg* 37:724-732
- [35] Finlay HM, McCullough L, Canham PB (1995) Three-dimensional collagen organization of human brain arteries at different transmural pressures. *J Vasc Res* 1995, 32, 301–312

- [36] Foster JH, Bolasny BL, Gobbel WG, Scott HW (1969) Comparative study of elective resection and expectant treatment of abdominal aortic aneurysm. *Surg Gynecol Obstet* 129(1):1–9
- [37] Frank C, Shrive N, Hiraoka H, Nakamura N, Kaneda Y, Hart D (1999) Optimisation of the biology of soft tissue repair. *J Sci Med Sport* 2:190–210
- [38] Freestone T, Turner RJ, Coady A, Higman DJ, Greenhalgh RM, Powell JT (1995) Inflammation and matrix metalloproteinases in the enlarging abdominal aortic aneurysm. *Arter Thromb and Vasc Bio* 15:1145–1151
- [39] Fung YC (1973) Biorheology of soft tissues. *Biorheology* 10:139–155
- [40] Fung YC, Fronek K, Patitucci P (1979) Pseudoelasticity of arteries and the choice of its mathematical expression. *Am J Physiol* 37:620–631
- [41] Fung YC (1993) *Biomechanics: Mechanical properties of living tissues*. New York: Springer-Verlag
- [42] Gasser TC (2016) Damage in vascular tissues and its modeling. *Mtr Para Iden Inv Prob in Soft Tiss Biomech*, Chapter 6
- [43] Gasser TC, Auer M, Labruto F, Swedenborg J, Roy J (2010) Biomechanical rupture risk assessment of abdominal aortic aneurysms: model complexity versus predictability of finite element simulations. *Euro J Vasc and Endo Surg* 40:176–185
- [44] Gasser TC, Gallinetti S, Xing X, Forsell C, Swedenborg J, Roy J (2012) Spatial orientation of collagen fibers in the Abdominal Aor-

- tic Aneurysm wall and its relation to wall mechanics. *Acta Biomater.* 2012, 8, 3091–3103
- [45] Gent AN (1996) A new constitutive relation for rubber. *Rubber Chem Tech* 69:59–61
- [46] Gleason RL, Taber LA, Humphrey JD (2004) A 2-D model of flow induced alterations in the geometry, structure, and properties of carotid arteries. *J Biomech Eng* 126(3):371–381
- [47] Green AE, Adkins JE (1970) *Large elastic deformations*, 2nd edn, Oxford University Press, Oxford. 6
- [48] Grootenboer N, Bosch JL, Hendriks JM, van Sambeek MRHM (2009) Epidemiology, aetiology, risk of rupture and treatment of abdominal aortic aneurysms: Does sex matter? *Eur J Vasc Endovasc Surg* 2009; 38:278–284.
- [49] Grytsan A, Eriksson TSE, Watton PN, Gasser TC (2017) Growth description for vessel wall adaptation: A thick-walled mixture model of abdominal aortic aneurysm evolution. *Materials*, 2017; 10,994.
- [50] Gurtner GC, Werner S, Barrandon Y, Longaker MT (2008) Wound repair and regeneration. *Nature* 453:314–321
- [51] Hartmann S, Neff P (2003) Polyconvexity of generalized polynomial-type hyperelastic strain energy functions for near-incompressibility. *Int J Solids and Str* 40(11): 2767–2791

- [52] He CM, Roach M (1993) The composition and mechanical properties of abdominal aortic aneurysms. *J Vasc Surg* 20:6–13
- [53] Henderson EL, Geng YJ, Sukhova GK, Whittemore AD, Knox J, Libby P (1999) Death of smooth muscle cells and expression of mediators of apoptosis by Tlymphocytes in human abdominal aortic aneurysms. *Circulation* 99(1): 96–104
- [54] Holzapfel GA, Gasser TC, Ogden RW (2000) A new constitutive framework for arterial wall mechanics and a comparative study of material models. *J Elasticity* 61:1–48
- [55] Holzapfel GA, Gasser TC, Ogden RW (2004) Comparison of a multi-layer structural model for arterial walls with a Fung-type model, and issues of material stability. *Trans ASME* 126:264–275
- [56] Houard X, Rouzet F, Touat Z, Philippe M, Dominguez M, Fontaine V, Sarda-Mantel L, Meulemans A, Le Guludec D, Meilhac O, Michel JB (2007) Topology of the fibrinolytic system within the mural thrombus of human abdominal aortic aneurysms. *J Pathol* 212(1): 20–28
- [57] Humphrey JD (1998) Computer methods in membrane biomechanics. *Comput Meth Biomech Biomed Eng* 1:171–210
- [58] Humphrey JD (1999) Remodeling of a collagenous tissue at fixed lengths. *J Biomech* 121:591–97
- [59] Humphrey JD (2003) Continuum biomechanics of soft biological tissues. *Proc R Soc Lond A* 459

- [60] Humphrey JD, Canham PB (2000) Structure, mechanical properties, and mechanics of intracranial saccular aneurysms. *J Elastic* 61:49–81
- [61] Humphrey JD, Rajagopal KR (2002) A constrained mixture model for growth and remodeling of soft tissues. *Math Models Methods Appl Sci* 12:407–430
- [62] Humphrey JD, Yin F (1989) Biomechanical experiments on excised myocardium: Theoretical consideration. *J Biomech* 22:377–383
- [63] Joldes GR, Miller K, Wittek A, Doyle B (2016) A simple, effective and clinically applicable method to compute abdominal aortic aneurysm wall stress. *J Mech Behav Biomed Mater* 58:139–148
- [64] Karrer HE (1961) An electron microscope study of the aorta in young and in aging mice. *J Ultrastruct Res* 5: 1–27
- [65] Keech MK (1960) Electron microscope study of the normal rat aorta. *J Biophys Biochem Cytol* 7: 533–538
- [66] Kenyon DE (1976) Transient filtration in a porous elastic cylinder. *J Applied Mech* 43:594–598
- [67] Klish SM, Chen SS, Sah RL, Hoger A (2003) A growth mixture theory for cartilage with application to growth-related experiments on cartilage explants. *J Biomech Eng* 125(3):169–179
- [68] Kroon M, Holzapfel GA (2007) A model of saccular cerebral aneurysm growth by collagen fiber remodeling. *J Theor Biol* 247:775–787

- [69] Kroon M, Holzapfel GA (2008) Modeling of saccular aneurysm growth in a human middle cerebral artery. *ASME J Biomech Eng* 130:051012
- [70] Kuhl E, Maas R, Himpel G, Menzel A (2007) Computational modeling of arterial wall growth. *Biomechan Model Mechanobiol* 6:321–331
- [71] Laksari K, Shafieian M, Darvish K (2012) Constitutive model for brain tissue under finite compression. *J Biomech* 45(4):642–646
- [72] Langille BL (1995) Blood flow-induced remodeling of the artery wall. In: Bevan, J.A., Kaley, G., Rubanyi, G.,M. (Eds.), *Flow-Dependent Regulation of Vascular Function*. Springer New York 277–299
- [73] Lederle FA, Johnson GR, Wilson SE, Ballard DJ, Jordan WD, Blebea J (2002) Rupture rate of large abdominal aortic aneurysms in patients refusing or unfit for elective repair. *JAMA* 287(22):2968–2972
- [74] Limet R, Sakalihassan N, Albert A (1991) Determination of the expansion rate and incidence of rupture of abdominal aortic aneurysms. *J Vasc Surg* 14:540–548
- [75] Lin WJ, Iafrati MD, Peattie RA, Dorfmann L (2018) Growth and remodeling with application to abdominal aortic aneurysms. *J Eng Math* 109:113–137
- [76] Long A, Rouet L, Bissery A, Rossignol P, Mouradian D, Sapoval M (2005) Compliance of abdominal aortic aneurysms evaluated by tissue doppler imaging: Correlation with aneurysm size. *J Vasc Surg* 42:18-26

- [77] Lopez-Candales A, Holmes DR, Liao S, Scott MJ, Wickline SA, Thompson RW (1997) Decreased vascular smooth muscle cell density in medial degeneration of human abdominal aortic aneurysms. *Am J Pathol* 150(3): 993–1007
- [78] Lu J, Zhou X, Raghavan ML (2007) Inverse elastostatic stress analysis in pre-deformed biological structures: Demonstration using abdominal aortic aneurysms. *J Biomech* 40:693–696
- [79] Maier A, Gee MW, Reeps C, Pongratz J, Eckstein HH, Wall WA (2010) A comparison of diameter, wall stress, and rupture potential index for abdominal aortic aneurysm rupture risk prediction. *Ann Biomed Eng* 38:3124–3134
- [80] Maurel W, Wu Y, Thalmann NM, Thalmann D (1998) *Biomechanical models for soft tissue simulation*. Springer
- [81] McGee GS, Baxter BT, Shively VP, Chisholm R, McCarthy WJ, Flinn WR, Yao JST, Pearce WH (1991) Aneurysm or occlusive disease-factors determining the clinical course of atherosclerosis of the infrarenal aorta. *Surgery* 110:370–376
- [82] Menashi S, Campa JS, Greenhalgh RM, Powell JT (1987) Collagen in abdominal aortic aneurysm: Typing, content, and degradation. *J Vasc Surg* 1987; 6:578–582
- [83] Menzel A (2007) A fibre reorientation model for orthotropic multiplicative growth. *Configurational driving stresses, kinematics-based reori-*

entation, and algorithmic aspects. *Biomech Model Mechanobiol* 6:303–320

- [84] Michel JB, Martin-Ventura JL, Egido J, Sakalihasan N, Treska V, Lindholt J, Allaire E, Thorsteinsdottir U, Cockerill G, Swedenborg J (2011) Novel aspects of the pathogenesis of aneurysms of the abdominal aorta in humans. *Cardiovasc Res* 90(1): 18–27
- [85] Moreno PR, Purushothaman KR, Sirol M, Levy AP, Fuster V (2006) Neovascularization in human atherosclerosis. *Circulation* 113(18): 2245–2252
- [86] Nackman GB, Karkowski FJ, Halpern VJ, Gaetz HP, Tilson MD (1997) Elastin degradation products induce adventitial angiogenesis in the Anidjar/Dobrin rat aneurysm model. *Surgery* 122(1): 39–44
- [87] Oden JT (1972) *Finite elements of nonlinear continua*. New York: McGraw-Hill
- [88] Ogden RW (1972) Large deformation isotropic elasticity - on the correlation of theory and experiment for incompressible rubber-like solids. *Proc of the Roy Soc A: Math, Phy and Eng Sci* 326:565–584
- [89] Ogden RW (1997) *Non-Linear Elastic Deformations*. Dover Publications
- [90] O’Leary SA, Healey DA, Kavanagh EG, Walsh MT, McGloughlin TM, Doyle BJ (2014) The biaxial biomechanical behavior of abdominal aortic aneurysm tissue. *Ann Biomed Engr* 42:2440–2450

- [91] Ouriel K, Green RM, Donayre C (1992) An evaluation of new methods of expressing aortic aneurysm size: Relationship to rupture. *J Vasc Surg* 15:12–18
- [92] Pancheri FQ, Eng CM, Lieberman DE, Biewener AA, Dorfmann L (2014) A constitutive description of the anisotropic response of the fascia lata. *J Mech Behav Biomed* 30:306–323
- [93] Pancheri FQ, Peattie RA, Reddy ND, Ahamed T, Lin W, Ouellette TD, Iafrati MD, Dorfmann L (2017) Histology and biaxial mechanical behavior of abdominal aortic aneurysm tissue samples. *J Biomech Eng* 139:031002
- [94] Peattie RA, Riehle TJ, Bluth E (2004) Pulsatile flow in fusiform models of Abdominal Aortic Aneurysms: Flow fields, velocity patterns and flow-induced wall stresses. *J of Biomech Eng* 126
- [95] Pierce DM, Fastl TE, Rodriguez-Vila B, Verbrugghe P, Fourneau I, Maleux G, Herijgers P, Gomez EJ, Holzapfel GA (2015) A method for incorporating three-dimensional residual stretches/stresses into patient-specific finite element simulations of arteries. *J Mech Behav Biomed Mater* 47:147–16
- [96] Polzer S, Gasser TC, Swedenborg J, Bursa J (2011) The impact of intraluminal thrombus failure on the mechanical stress in the wall of abdominal aortic aneurysms. *Eur J Vasc Endovasc Surg*
- [97] Polzer S, Gasser T, Novak K, Man V, Tichy M, Skacel P, Bursa J (2015) Structure-based constitutive model can accurately predict pla-

- nar biaxial properties of aortic wall tissue. *Acta Biomater.* 2015, 14, 133–145
- [98] Rachev A, Meister J (1998) A model for geometric and mechanical adaption of arteries to sustained hypertension. *J Biomech Eng* 120:9–17
- [99] Raghavan ML, Vorp DA (2000) Toward a biomechanical tool to evaluate rupture potential of abdominal aortic aneurysm: identification of a finite strain constitutive model and evaluation of its applicability. *J Biomech* 33:475–482
- [100] Raghavan ML, Vorp DA, Federle M., Makaroun MS, Webster MW (2000) Wall stress distribution on three-dimensionally reconstructed models of human abdominal aortic aneurysm. *J Vasc Surg* 31:760–769
- [101] Rajagopal K, Wineman A (1992) A constitutive equation for nonlinear solids which undergo deformation induced microstructural changes. *Int J Plasticity* 8:385-395
- [102] Rezakhaniha R, Agianniotis A, Schrauwen JTC, Griffa A, Sage D, Bouten CVC, van de Vosse FN, Unser M, Stergiopoulos N (2012) Experimental investigation of collagen waviness and orientation in the arterial adventitia using confocal laser scanning microscopy. *Biomech Model Mechan* 11:461–473
- [103] Rissland P, Alemu Y, Einav S, Ricotta J, Bluestein D (2009) Abdominal aortic aneurysm risk of rupture: patient-specific FSI simulations using anisotropic model. *ASME J Biomech Eng* 131:031001

- [104] Rivlin RS, Saunders DW (1951) Large elastic deformations of isotropic materials. VII. Experiments on the deformation of rubber. *Phi Trans Roy Soci A. Math, Phy and Eng Sci* 243:251–288
- [105] Rizas KD, Ippagunta N, Tilson MD (2009) Immune cells and molecular mediators in the pathogenesis of the abdominal aortic aneurysm. *Cardiol Rev.* 2009; 17:201–?10
- [106] Robinet A, Fahem A, Cauchard JH, Huet E, Vincent L, Lorimier S, Antonicelli F, Soria C, Crepin M, Hornebeck W, Bellon G (2005) Elastin-derived peptides enhance angiogenesis by promoting endothelial cell migration and tubulogenesis through upregulation of MT1-MMP. *J Cell Sci* 118(Pt 2): 343–356
- [107] Rodriguez JF, Ruiz C, Doblare M, Holzapfel GA (2008) Mechanical stresses in abdominal aortic aneurysms: influence of diameter, asymmetry and material anisotropy. *J Biomech Eng* 130,021023
- [108] Rodriguez EK, Hoger A, McCulloch AD (1994) Stress-dependent finite growth in soft elastic tissues. *J Biomech* 27:455–67
- [109] Roy CS (1880) The elastic properties of the arterial wall. *Phil Trans R Soc Lond B* 99:1–31
- [110] Schrieffl A, Zeindlinger G, Pierce D, Regitnig P, Holzapfel G (2012) Determination of the layer-specific distributed collagen fiber orientations in human thoracic and abdominal aortas and common iliac arteries. *J R Soc Interface* 2012, 7, 1275–1286

- [111] Schwartz SM (1997) Smooth muscle migration in atherosclerosis and restenosis. *J Clin Invest* 100(11 Suppl): S87–89
- [112] Scotti CM, Jimenez J, Muluk SC, Finol EA (2008) Wall stress and flow dynamics in abdominal aortic aneurysms: finite element analysis vs. fluid-structure interaction. *Comp Meth Biomech Biomed Eng* 11:301–322
- [113] Sheidaei A, Hunley SC, Zeinali-Davarani S, Raguin LG, Baek S (2011) Simulation of abdominal aortic aneurysm growth with updating hemodynamic loads using a realistic geometry. *Med Eng Phys*. 33:80-88
- [114] Silverberg E, Boring CC, Squires TS (1990) Cancer statistics. *CA Cancer J Clin* 40:9–26
- [115] Singh K, Bnaa KH, Jacobsen BK, Bjork L, Solberg S (2001) Prevalence of and risk factors for abdominal aortic aneurysms in a population based study 154(3):236–244
- [116] Skalak R (1981) Growth as a finite displacement field. *Proc IUTAM symp fin elast August 10-15, 1980*
- [117] Speelman L, Bohra A, Bosboom EMH, Schurink GWH, Van de Vosse, Makaorun MS, Vorp DA (2007) Effects of wall calcification in patient-specific wall stress analyses of abdominal aortic aneurysms. *J Biomech Eng* 129:105–109
- [118] Spencer AJM (1971) Theory of Invariants. In: Eringen, A.C. (Ed.), *Continuum Physics. Vol. 1*. Academic Press, New York, 239–353

- [119] Stanfordhealthcare.org (2010)
- [120] Stary HC (2000) Lipid and macrophage accumulations in arteries of children and the development of atherosclerosis. *Am J Clin Nutr* 72(5 Suppl): 1297S–1306S
- [121] Taber LA (1995) Biomechanics of growth, remodeling and morphogenesis. *Appl Mech Rev* 48:487–545
- [122] Taber LA (1998) A model for aortic growth based on fluid shear and fiber stresses. *J Biomech Eng* 120:348–354
- [123] Thompson S, Brown L, Sweeting M, Bown M, Kim L, Glover M, Buxton M, Powell J (2013) Systematic review and meta-analysis of the growth and rupture rates of small abdominal aortic aneurysms: Implications for surveillance intervals and their cost-effectiveness, *Health Technol. Assess* 17:1–118
- [124] Thunes JR, Pal S, Fortunato RN, Phillippi JA, Gleason G, Vorp DA, Maiti S (2016) A structural finite element model for lamellar unit of aortic media indicates heterogeneous stress field after collagen recruitment. *J. Biomech.* 2016, 49, 1562–1569
- [125] Tong J, Cohnert T, Regitnig P, Holzapfel GA (2011) Effects of age on the elastic properties of the intraluminal thrombus and the thrombus-covered wall in abdominal aortic aneurysms: Biaxial extension behaviour and material modelling. *Eur J Vasc Endovasc Surg* 42:207–219
- [126] Tozern A, Skalak R (1988) Interaction of stress and growth in a fibrous tissue. *J bio* 130:337–50

- [127] Truesdell C, Noll W (1965) *The non-linear field theories of mechanics*, ISBN 978-3-662-10388-3
- [128] Valentin A, Cardamone L, Baek S, Humphrey J (2009a) Complementary vasoactivity and matrix re-modelling in arterial adaptations to altered flow and pressure. *J Roy Soc Interface* 6:293–306
- [129] Valentin A, Humphrey J (2009b) Evaluation of fundamental hypotheses underlying constrained mixture models of arterial growth and remodelling. *Philos T Roy Soc A* 367:3585–3606
- [130] Valentin A, Humphrey J, Holzapfel GA (2011) A multi-layered computational model of coupled elastin degradation, vasoactive dysfunction, and collagenous stiffening in aortic aging. *Ann Biomed Eng* 39:2027–2045
- [131] Valentin A, Humphrey J, Holzapfel GA (2013) A finite element-based constrained mixture implementation for arterial growth, remodeling, and adaptation: Theory and numerical verification. *Int J Numer Meth Biomed Engng* 29:822–849
- [132] Vande Geest JP, Wang DHJ, Wisniewski SR, Makaroun MS, Vorp DA (2006) A noninvasive method for determination of patient-specific wall strength distribution in abdominal aortic aneurysms. *Ann Biomed Eng* 34:1098-1106
- [133] Venkatasubramaniam AK, Fagan MJ, Mehta T, Mylankal KJ, Ray B, Kuhan G, Chetter IC, McCollum PT (2004) A comparative study of

aortic wall stress using finite element analysis for ruptured and non-ruptured abdominal aortic aneurysms. *Euro J Vasc Endov Surg* 28:168-176

- [134] Volokh k. (2014) Modeling aneurysm growth and failure. *IUTAM* 12(2015)204–210
- [135] Vorp DA, Mandarino WA, Webster MW, Gorcsan J. (1996) 3rd Potential influence of intraluminal thrombus on abdominal aortic aneurysm as assessed by a new non-invasive method. *Cardi Surg* 4:732
- [136] Vorp DA, Wang DH, Webster MW, Federspiel WJ (1998) Effect of intraluminal thrombus thickness and bulge diameter on the oxygen diffusion in abdominal aortic aneurysm. *J Biomech Eng* 120(5): 579–583
- [137] Vorp DA (2007) Biomechanics of abdominal aortic aneurysm. *J Biomech* 40:1887–1902
- [138] Wang DHJ, Makaroun MS, Webster MW, Vorp DA (2002) Effect of intraluminal thrombus on wall stress in patient-specific models of abdominal aortic aneurysm. *J Vasc Surg* 36:598–604
- [139] Watton PN, Hill NA, Heil M (2004) A mathematical model for the growth of the abdominal aortic aneurysm. *Biomech and Mod Mech* 3:98–113
- [140] Watton PN, Hill NA, Heil M 2009. Evolving mechanical properties of a model of abdominal aortic aneurysm. *Biomech Model Mechan* 8:25–42

- [141] Willis AI, Pierre-Paul D, Sumpio BE, Gahtan V (2004) Vascular smooth muscle cell migration: current research and clinical implications. *Vasc Endovascular Surg* 38(1):11–23
- [142] Wilson JS, Baek S, Humphrey JD (2012) Importance of initial aortic properties on the evolving regional anisotropy, stiffness and wall thickness of human abdominal aortic aneurysms. *J Roy Soc Interface* 9:2047–2058
- [143] Wilson JS, Baek S, Humphrey JD (2013) Parametric study of effects of collagen turnover on the natural history of abdominal aortic aneurysms. *Proc R Soc A Math Phys Eng Sci* 469:20120556
- [144] Wolinsky H, Glagov S (1964) Structural Basis for the Static Mechanical Properties of the Aortic Media. *Circulation Research* 14: 400–413
- [145] Yeoh OH (1993) Some forms of the strain energy function for rubber. *Rub Chem and Tech* 66(5):754–771
- [146] Young A (2011) The physiology of wound healing. *Surgery (Oxford)* 29:475–479
- [147] Zulliger MA, Rachev A, Stergiopoulos N (2004) A constitutive formulation of arterial mechanics including vascular smooth muscle tone. *Am J Physiol Heart Circ Physiol* 287(3):1335–1343